UNIVERSITY OF SOUTHAMPTON

A measurement based study of the acoustics of pipe systems with flow

by

Emmet J. English

A thesis submitted in partial fulfillment for the degree of Doctor of Philosophy

in the

Faculty of Engineering Science and Mathematics

Institute of Sound and Vibration

July 2010

UNIVERSITY OF SOUTHAMPTON

Abstract

Faculty of Engineering Science and Mathematics
Institute of Sound and Vibration

Doctor of Philosophy

by Emmet J. English

The focus of this thesis is the measurement of specific aeroacoustic properties in ducts at frequencies below the cut-on frequency of the first higher order mode. A body of measurement results are presented which highlight the effect of flow on some of the aeroacoustic characteristics in ducts as well as describe the aeroacoustic sources of an in-duct orifice and a simple expansion chamber. The results have been compared with published theory where appropriate.

Important developments from measurements of the acoustic characteristics of a simple duct with flow include a new experimental method to determine the viscothermal attenuation coefficient. In addition, pressure reflection coefficient measurements of an unflanged duct with flow with two different edge conditions are used in conjunction with a numerical model developed by Gabard [1] to determine the extent of vorticity shed from the duct termination.

A novel method is presented for the measurement of aeroacoustic source strengths in ducts with flow. The source is defined in terms of acoustic power and is determined by measuring the acoustic power flux both upstream and downstream of the source region in a duct. The method adopts a plane wave approximation and was assessed experimentally by creating a source in a duct at a number of known frequencies and modifying its magnitude by a known amount.

The source measurement technique is applied to an in-duct orifice. The results are used to determine the spectral characteristic and velocity dependence of the source. The results indicate that the duct-to-orifice area ratio has a important effect on the spectral characteristics and velocity dependence of the source.

New measurements of the aeroacoustic source strength of a simple flow excited expansion chamber are presented. The results indicate that lock-on flow tones occur when hydrodynamic modes which form in the chamber match the tailpipe resonant frequencies. The results are compared with predictions of a model based on describing function theory.

Acknowledgements

This thesis was completed in part under the supervision of Prof. P.O.A.L. Davies who sadly past away in 2008. It was a privilege to work with someone with such enthusiasm and I am very thankful for the insight and technical support which he contributed. I would also like to thank my supervisor Dr. Keith Holland for his input and advice during all stages of the research. Thanks is also due to Dr. Gwénaël Gabard whose Matlab code enabled significant insight and development during my research.

I would like to express my gratitude to my parents who have been a constant source of love, support and encouragement which kept me going when things got hard. I'd also like to thank my sisters Fiona and Stephanie for the enjoyment each of their distinct personalities provides.

Contents

List of Figures

Nomenclature

α	Viscousthermal attenuation coefficient.
$\bar{\rho}$	Mean density
$\bar{p}$	Mean pressure
$\bar{T}$	Ambient Temperature
$\bar{U}$	Mean flow velocity
$\bar{W}_r$	Acoustic power radiated into farfield from duct termination
$\bar{W}_s$	Source acoustic power flux
β	Constant which accounts for the 'Phase Lag' associated with the arrival of the vortex at the trailing edge and the emission of the acoustic pulse
$\Delta\bar{P}$	Pressure drop, differential pressure
δ	Acoustic end correction a unflanged duct termination
δ_∞	Acoustic end correction of a duct terminated with an infinite flange
δ_{ac}	Acoustic boundary layer thickness, $\sqrt{\frac{2u_*^2}{\nu\omega}}$
$\dot{Q}$	Volumetric flow rate
Γ	Parameter describing the extent of shed vorticity
γ	Ratio of specific heats
γ_{12}^2	Coherence Function
$\hat{\rho}$	Acoustic part of density

$\hat{H}_{nm}$ Transfer function

$\hat{k}^{\pm}$ Wave numbers of the positive and negative propagating wave disturbances

$\hat{p}$ Acoustic pressure

$\hat{p}^{\pm}$ Postive and negative travelling pressure wave components

$\hat{R}$ Pressure reflection coefficient

$\hat{u}$ Acoustic particle velocity

ν Kinematic viscosity

Ω Non-dimensional frequency, ω/ω_o

ω Angular frequency

ω_o Natural frequency of a resonator, $\sqrt{K/M}$, [Rad/s]

ρ Density, absolute density

$\widetilde{\delta}$ Acoustic end correction of a duct with a finite wall thickness

ζ Specific acoustic impedance

A Surface area over which a oscillatory flow acts

a Radius of duct

C Calibration Coefficient

c Speed of sound

C_D Drag Coefficient

C_d Orifice discharge coefficient

D Diameter, inlet pipe diameter

d Length over which a hydrodynamic mode developes

D_o Orifice Diameter

F Force, Force Exerted on a fluid in the resonator opening.

f_r Resonant frequencies

f_s Sampling Frequency, Samples per second

f_{res} Spectral binwidth

G_{nm} Cross spectrum

G_{nn} Autospectrum

H_j Hankel function of order J

I Acoustic intensity

K Stiffness of resonator

k Wavenumber,$\frac{\omega}{c}$

$K_o^{\pm}$ Propagation Constant

ka Helmhotz number,$\frac{\omega a}{c}$

L Length, Cavity Length

L_t Tailpipe Length

L_{eff} Effective Length

M Mach number

m Mass

n Velocity dependence, Mode number

p Pressure, absolute pressure

p_f Farfield pressure

Pr Prantl number,

Q Quality factor of a resonator, $\sqrt{Kn}/r$

q_o Orifice volume velocity,

q_r Resonator volume velocity

r Radiation resistance

R_o Universal gas constant

Re Reynolds number

S Area

S_o Orifice cross sectional area

S_t Cross-sectional area of tailpipe

Sh Shear wave number, $Sh = a\sqrt{\frac{\omega}{\nu}}$

Str Strouhal number,$\frac{fL}{U}$

U Flow velocity

U_c Convective velocity

u_* Friction velocity

V Voltage

W Acoustic power

$W^{\pm}$ Acoutic power flux

x Displacement

List of Tables

Chapter 1

Introduction

1.1 Introduction

Large gas pipelines, intake and exhaust systems for reciprocating internal combustion engines, as well as industrial exhaust stacks are all examples of gas transport system in which sound generation and propagation can occur. The details of this sound generation and propagation is important due to its potential environmental impact when radiated from automotive or stack exhausts, or when it has an affect the structural integrity of the containing system. Consequently, in order to aid engineers at both the design and problem solution stage it is important that a knowledge of (i) the effect of flow on the aeroacoustic properties, and (ii) how and when the flow acts as a means of sound generation and absorption. As a result, it is essential that we gather specific experimental information of the effect of flow on the acoustic characteristics as well as quantitative detail of aeroacoustic sources and sinks related to common geometrical features of such systems.

1.1.1 Thesis overview

The focus of this thesis is the measurement of specific aeroacoustic properties in ducts at frequencies below the cut-on frequency of the first higher order mode. This thesis proposes a novel experimental technique for measurement of in-duct sources and applies it to two common geometrical features of gas transport systems; the in-duct orifice and the simple expansion chamber or cavity. This chapter presents

a survey of the literature and highlights common techniques employed to measure basic characteristics of a planar sound field in a duct. In addition it shows that there are a limited number of measurement techniques available to measure in-duct source strength.

Chapter 2 presents the method, experimental technique and experimental set-up developed to measure the pressure wave components in a duct with flow at frequencies below the cut-on of the first higher order mode. A novel technique for measuring the attenuation coefficient with flow is presented. Experimental results determined using the technique are presented and compared with theoretical predictions. Measurements of the pressure reflection coefficient of an unflanged duct with outflow are presented for two different edge conditions. The measured pressure reflection coefficients are used in conjunction with theoretical predictions to estimate the extent of vorticity shed from the duct end for each edge condition. In addition, measurements of the acoustic end correction of an unflanged duct with flow are presented and compared with theoretical predictions.

In chapter 3 the topic of sound power flux in ducts with flow is addressed. Sound power flux measurements are compared with that predicted using commercial software. The absorption of sound power through the jet formed at the outlet of a simple unflanged duct with outflow is measured and compared with predictions. A new technique for measuring the aeroacoustic source strength in ducts with flow at frequencies below the cut-on of the first higher order mode is presented. The method is based on simultaneous measurement of the acoustic power flux either side of the source region of interest. The technique is tested experimentally using an artificial source in a simple duct with no flow.

Chapter 4 assesses the aeroacoustics of an in-duct orifice with flow. The chapter examines the potential of the orifice (or more accurately the flow through the orifice) to act as both a means of sound absorption and sound generation. An equation for the amount of sound absorption by the orifice is derived and compared with experimental results. Both the prediction and results highlight the importance of the local acoustic field on the amount of sound absorption. The sound generated by flow through an orifice with three different duct-to-orifice area ratios is measured using the source measurement techniques presented in chapter

3. Measurements of the source power are used to determine the velocity dependence of the sources for each orifice as well as the spectral characteristics of each source.

The source measurement technique developed in chapter 3 is used in chapter 5 to measure the aeroacoustic source of an simple expansion chamber with flow. The effect of chamber length on the source characteristics is assessed. The results indicate that acoustic lock-on is the primary source mechanism for such duct geometries. In addition, a technique for modeling the source associated with the acoustic feedback mechanism apparent in the results is adopted and modified to predict the source characteristics of the expansion chamber. The prediction of the source frequency and the experimental results are compared. The final chapter of this thesis summaries the conclusion and gives suggestions for further work.

1.2 The effects of flow on the acoustic characteristics

FIGURE 1.1: Esso Fawley oil refinery, Hampshire, United Kingdom.

Gas transport systems are common features of a modern industrial environment. An example of this is shown in figure 1.1 of the Esso Fawley oil refinery in Hampshire, UK and it highlights the complexity of the pipe networks which exist. In order to acoustically model gas transport system an understanding of the effect of flow on the basic acoustic properties is required. Such acoustic properties includes the extent of damping within the system and the pressure reflection. Since automotive exhaust system and industrial exhaust stacks are commonly terminated with an unflanged open duct this thesis will examine these features first as a prerequisite to aeroacoustic source measurement in ducts.

1.3 Plane wave propagation in ducts with flow

In a duct, so long as the Helmholtz number remains less than $1.84\sqrt{1-M^2}$, where M is the mean flow Mach number, the resultant acoustic wave motion can be considered substantially one-dimensional [9]. The Helmholtz number, ka, can be defined as

$$ka = \frac{\omega a}{c}, \tag{1.1}$$

where ω is the angular frequency of the acoustic wave disturbance, a is the radius of the duct and c is the speed of sound in the medium. Under these conditions the spectral amplitude of the component waves traveling in the direction of x positive can then be described as

$$\hat{p}^+(x,\omega) = \hat{p}_0^+ e^{j(\omega t - \hat{k}^+ x)}, \tag{1.2}$$

and those traveling in the opposite direction by

$$\hat{p}^-(x,\omega) = \hat{p}_0^- e^{j(\omega t + \hat{k}^- x)}, \tag{1.3}$$

where $\hat{p}_0^+$ and $\hat{p}_0^-$ are the component pressure wave amplitudes at $x = 0$. Here $\hat{k}^+$ & $\hat{k}^-$ are the complex acoustic wave numbers of the positive and negative propagating wave disturbances. In practice, with ducts of finite length, both components exist simultaneously so that the fluctuating pressure at each frequency is then

$$\hat{p}(x,t) = \hat{p}_0^+ e^{j(\omega t - \hat{k}^+ x)} + \hat{p}_0^- e^{j(\omega t + \hat{k}^- x)}. \tag{1.4}$$

The complex wave numbers replace the wave number, $k = \omega/c$, to take account of the effects of the mean flow and viscothermal attenuation associated with tangential stresses at the duct wall. In the absence of flow Kirchoff [10] demonstrated that the inviscid wave number k is modified to $k\hat{K}_o$ due to viscothermal losses at the pipe wall where the propagation constant $\hat{K}_o$ is given by [11] as

$$\hat{K}_o = 1 + \alpha(1-j)\frac{c}{\omega}. \tag{1.5}$$

Where α is the viscothermal attenuation coefficient. Initially, to account for the effects of steady flow, an *ad hoc* solution[12] was adopted which defined the forward, K_o^+, and backward, K_o^-, propagation constants as

$$\hat{K}_o^{\pm} = \frac{\hat{K}_o}{1 \pm M}. \tag{1.6}$$

However this has been superseded by an alternative formulation published in 1995 by Dokumaci [13, 14] who presents the forward and backward propagation constants for acoustic wave motion in a duct with superimposed uniform mean flow as

$$\hat{K}_o^{\pm} = \frac{\hat{K}_o}{1 \pm M\hat{K}_o}. \tag{1.7}$$

Using this formulation the complex wave numbers are defined as

$$\begin{aligned} \hat{k}^+ &= k\hat{K}_o^+, \\ \hat{k}^- &= k\hat{K}_o^-. \end{aligned} \tag{1.8}$$

It is apparent from eqns 1.2 & 1.3 that propagation of plane wave in a duct is highly dependent on these complex wavenumbers. Consequently, it is believed important that k^+ & k^-, and their constituent parameters clearly defined. One such parameter is the visco-thermal attenuation coefficient.

Author	Expression For α
Helmholtz [15]	$\alpha_h = \frac{\omega}{c\sqrt{2}Sh}$
Kirchoff [16]	$\alpha_K = \frac{\omega}{c}\left(\frac{1}{\sqrt{2}Sh}\left(1+\frac{\gamma-1}{\sqrt{Pr}}\right)+\frac{1}{Sh^2}\left(1+\frac{\gamma-1}{\sqrt{Pr}}-\frac{\gamma}{2}\frac{\gamma-1}{Pr}\right)\right)$
Rayleigh (Narrow tube) [17]	$\alpha_R = \frac{\omega}{c}\left(\frac{2\sqrt{\gamma}}{Sh}\right)$
Ingard [18]	$\alpha_{Ing} = \frac{\omega}{c}\frac{2^{-\frac{3}{2}}}{Sh}\left(1+\frac{1}{\sqrt{Pr}}\right)$

TABLE 1.1: Different expressions for the viscothermal attenuation coefficient in ducts with flow

1.3.1 Viscothermal attenuation coefficient

In a duct the propagation of sound waves is dissipative because of viscothermal losses at the pipe wall. Such losses can be accounted for by including a viscothermal attenuation coefficient, α, in the analysis. A number of analytical expressions exist for the viscothermal attenuation coefficient in a cylindrical duct with flow. Tijdeman [11] highlights that the viscothermal attenuation coefficient can be completely defined by the Helmholtz number, ka, where a is the duct radius, the shear wave number, $Sh = a\sqrt{\frac{\omega}{\nu}}$, with ν representing the kinematic viscosity, the Prantl number, Pr, and the ratio of specific heats, γ. For a given gas Pr and γ can be considered constant at a specific temperature. Table 1.1 above shows a number of commonly adopted expressions for α. In the expressions, the inclusion of Sh indicates the effects of viscosity are accounted for, and the inclusion of γ and Pr indicates the effects of heat conduction are accounted for. The expression by Helmholtz notably excludes the effects of heat conduction due to the omission of Pr and γ in the equation and only takes account of viscosity.

Figure 1.2 is a comparison of the viscothermal attenuation coefficients defined in Table 1.1 as a function of Helmholtz number. It is clearly apparent that α increases with increasing ka. Further examination of all the expressions indicates that α increases as a function of $\sqrt{\omega}$. Helmholtz's expression consistently provides the lowest value of α for all frequencies. This is to be expected as Helmholtz's expression does not include the effect of heat conduction. Rayleigh's expression is significantly higher than that of the other curves. Figure 1.3 is a plot in dB of the attenuation of a sound wave in a duct as a function of distance for different values of ka. It is apparent from the plot that the extent of the attenuation remains low for pipes of relatively short length such as automotive exhaust systems. However, when the pipe system is much larger such as that of gas pipe lines the attenuation

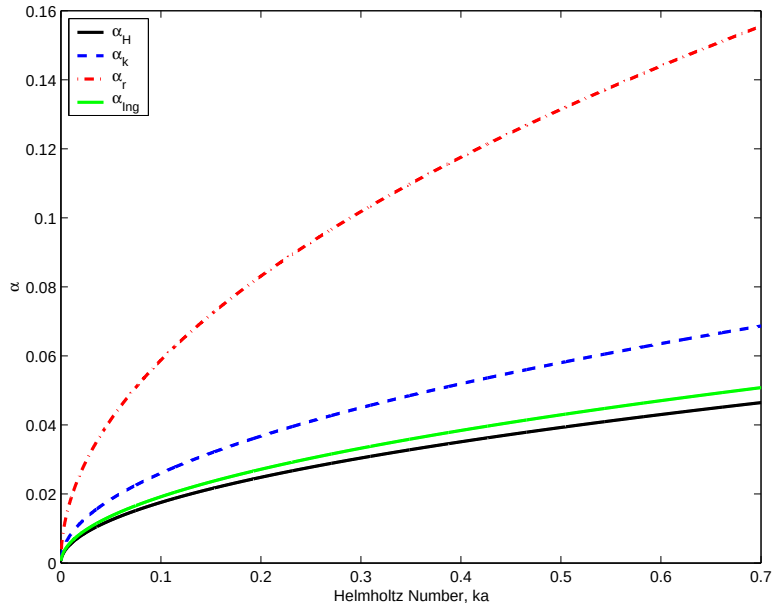

FIGURE 1.2: Comparison of the viscothermal attenuation coefficients defined in Table 1.1 as a function of ka.

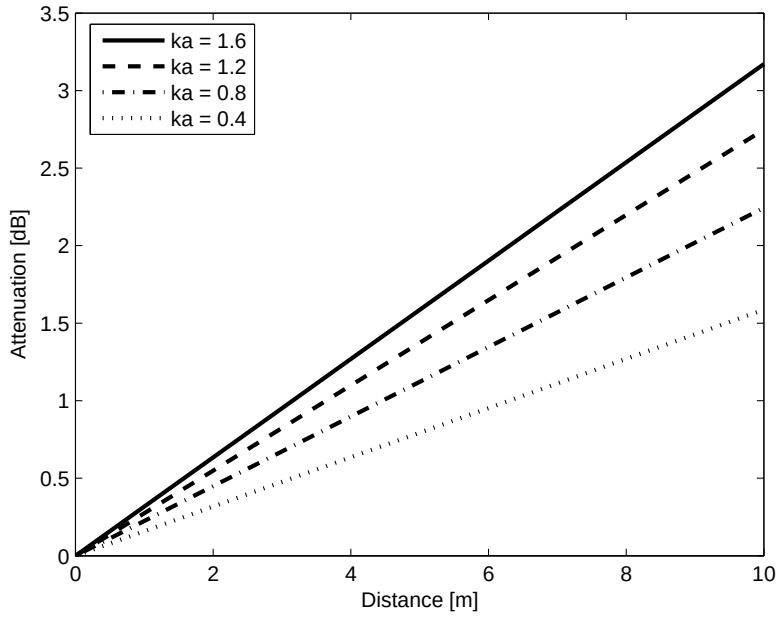

FIGURE 1.3: Attenuation of a sound wave in a duct as a function of distance for different values of ka. Duct containing air at 18^oC with an internal diameter of 8cm.

of sound due to viscothermal attenuation can be quite high. Consequently, it is important that the viscothermal attenuation coefficient is clearly defined in order for the acoustic wave propagation of such system to modeled correctly.

When there is a mean flow within the duct the level of damping is modified. The presence of turbulence in the duct has been highlighted to have an effect on the damping of acoustic waves. Ingard and Singhal[18] model the attenuation of sound in turbulent pipe flow. In their analysis they consider the oscillatory flow of the sound field to represent a quasistatic modulation of the steady flow. This results in a modulation of the pressure drop in the pipe, which can be expressed as equivalent turbulent friction acting on the oscillatory flow. The simple model obtained indicates an increase in the attenuation of the acoustic waves propagating when there is mean flow. This additional attenuation due to the turbulence is related to the Reynolds number, Mach number, and duct wall friction factor. As a result of their analysis they indicate that the viscothermal attenuation coefficient, α, should be replaced in the upstream direction with α^- and in the downstream direction with α^+. In addition, they note α^- to be higher than that of α^+. Comparison of the predictions with measurements reinforces the validity of the model, however, the large amount of scatter in the measurements suggest limited precision in the measurements. In addition, Ingard and Singhal's analysis adopted the *ad hoc* formulation of the wave propagation with flow which, as mention, has recently been superseded.

Howe[19] proposes an alternative model for the viscothermal attenuation coefficients with flow. The model include the effect of the turbulent boundary layer eddy viscosity. The model shows good agreement with experiments by Peters et al[20] within the range $0.02<M<0.12$ indicating an increase in the overall attenuation of acoustic waves when there is mean flow. The model is limited to Reynolds numbers above 10^4, below which the eddy viscosity model may be invalid. More recently Allam and Abom[21] experimentally investigated the damping of acoustic waves in a duct with mean flow at low frequencies. In their analysis the differences between the *ad hoc* and Dokumaci formulation for the complex wave numbers are highlighted. They also compare measurements of the viscothermal attenuation coefficient with flow with Howe's model indicating it is valid up to a normalised acoustic boundary layer thickness of 30-40. However, this seems to be the only experimental analysis of plane wave propagation in ducts for which Dokumaci's formulation for the propagation constants with flow has been adopted.

In conclusion, since plane wave propagation in ducts is dependent on the complex wave numbers it is crucial for these to be clearly defined when modeling the plane wave propagation in ducts with flow as well when undertaking experiments using

a plane wave decomposition technique. Since there has been recent developments in the definition of the complex wavenumbers when flow is present it is believed necessary that the topic of the viscothermal attenuation coefficient be revisited. In this thesis an alternative and, to the authors knowledge, novel experimental technique for determining the viscothermal attenuation coefficient is presented.

1.3.2 Pressure reflection coefficient

One topic of particular interest to exhaust systems is the pressure reflection coefficient of a simple unflanged duct termination. Almost all exhaust system are terminated with a simple tailpipe comparable to that of an unflanged duct. The pressure reflection coefficient, $\hat{R}$, is the complex ratio of the reflected, $\hat{p}^-$, to incident, $\hat{p}^+$, pressure wave amplitude and is an important factor controlling the radiation of sound from exhaust tailpipes. Notably, the pressure reflection coefficient can be related to the normalised specific acoustic impedance, ζ, by the expression

$$\zeta = \frac{1+\hat{R}}{1-\hat{R}} \tag{1.9}$$

At low frequencies where the acoustic wave propagation can be considered to be substantially one-dimensional the magnitude of the reflection coefficient tends toward unity indicating that the majority of the incident pressure wave component is reflected at the duct termination. The magnitude of the pressure reflection coefficient is in fact a function of frequency and duct radius. Levine and Schwinger's[2] paper on the radiation of sound from an unflanged circular pipe provides the most widely accepted theoretical model for the pressure reflection coefficient. The model has been experimental tested on numerous occasion [20–22] with all results indicating the validity of the prediction to within the precision of the measurement methods employed.

Under mean outflow conditions the magnitude of the pressure reflection coefficient no longer matches that predicted by Levine and Schwinger's model. Munt [3, 4] developed Levine and Schwinger's approach to include the presence of subsonic flow out of the pipe. In the Munt's analysis, the jet exhaust is considered to be separated from the ambient, stagnant or co-flowing, fluid by an unstable cylindrical vortex layer. Munt's solution assumes a full Kutta condition (smooth separation from the trailing edge) at which all the vorticity is shed from the duct wall. Munt's

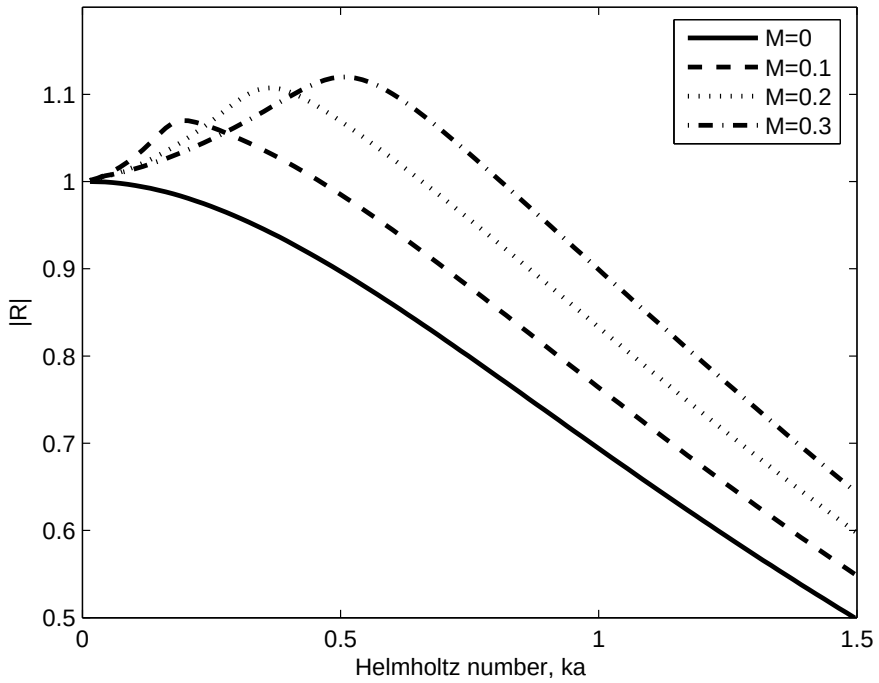

FIGURE 1.4: Theoretical reflection coefficient for a simple unflanged duct with outflow [2–4].

model yields a number of interesting results, most notably, the possibility of the modulus of the pressure reflection coefficient exceeding a value of unity for certain values of Helmholtz number.

Figure 1.4 is a plot of the pressure reflection coefficient as predicted by Levine and Schwinger for no flow, and Munt for mean outflow Mach numbers of 0.1, 0.2 & 0.3. The pressure reflection coefficient is plotted as a function of Helmholtz number, ka. Published experimental results [20, 21, 23, 24] generally support the prediction, but variation in the peak magnitude and frequency do exist. For example, Schlinker's [24] results are in excess of Munt's theory by up to 20%. The reason for these differences has yet to be fully explained. However, Rienstra [5, 6] extented Munt's analysis to include an edge condition parameter, Γ, to account for the amount of vorticity shed from the duct termination. To the authors knowledge, this edge condition has yet to be determined experimentally for an unflanged duct termination with flow. In Chapter 2 measurements of the pressure reflection coefficient of an unflanged duct with different wall thicknesses are compared with that of Munt's prediction. The results are then used to determine the edge condition parameter, as proposed by Rienstra.

1.3.3 End correction

The acoustic end correction is an imaginary extension to the end of the duct. This correction when added to the end of the duct allows for the correct value of acoustic inertance to be determined [25]. This end correction can be related to the phase of the pressure reflection coefficient [9]. Levine and Schwinger's[2] model of an simple unflanged duct with no flow, which assumes an infinitely thin duct wall edge, predicts the end correction, δ, to be a smooth function of ka with a low frequency limit $0.6133a$. Dalmont et al [26] provide a fit to Levine and Schwinger's prediction for $ka < 1.5$ as

$$\delta = 0.6133a \left(\left(\frac{1 + 0.044ka^2}{1 + 0.19ka^2} \right) - 0.02 \left(sin^2(2ka) \right) \right). \tag{1.10}$$

The other extreme case for duct wall thickness is that of an infinite flange. Noris and Sheng [27] paper on acoustic radiation from a circular pipe with an infinite flange provides an expression for the end correction, δ_∞, of such a geometry for $ka < 3.5$ as

$$\delta_\infty = 0.8216a \left[1 + \frac{0.77ka^2}{1 + 0.77ka} \right]. \tag{1.11}$$

However, rather than a infinitely thin duct wall or an infinite flange, a typical unflanged duct will have a certain wall edge thickness, providing an end correction somewhere between that provided by eqn 1.10 and eqn 1.11. Dalmont et al [26] provide an expression for the end correction of an unflanged circular duct with a finite wall thickness as

$$\widetilde{\delta} = \delta_\infty + \frac{a}{b} * (\delta - \delta_\infty) + \frac{0.057a^2}{b} \left(1 - (a/b)^5 \right). \tag{1.12}$$

where a is the duct inner radius and b is the duct outer radius. It should be highlighted that eqn 1.12 is equivalent to that of Levine and Schwinger's prediction for $a/b = 1$. Peters et al's [20] published experimental results of the acoustic end correction for an unflanged duct with flow with an inner duct radius to outer duct radius ratios, a/b of $= 1$ (tapered wall edge), 0.85, and 0.7 over the range $0.03 \leq ka \leq 0.28$. Comparing their results with that predicted by eqn 1.12 indicates the experimental results are 10.6%, 3.77% and 4.1% higher for a/b of 1,

0.85 and 0.7 respectively. In comparison to this, Allam and Abom [21] published results for an unflanged duct with $a/b = 0.875$ which match the expression of Levine and Schwingers to within 1.4%. This is surprising, as eqn 1.12 predicts a duct termination with $a/b = 0.875$ to have an end correction which is larger by between 6.1% and 8.2% than that of an infinitely thin duct wall.

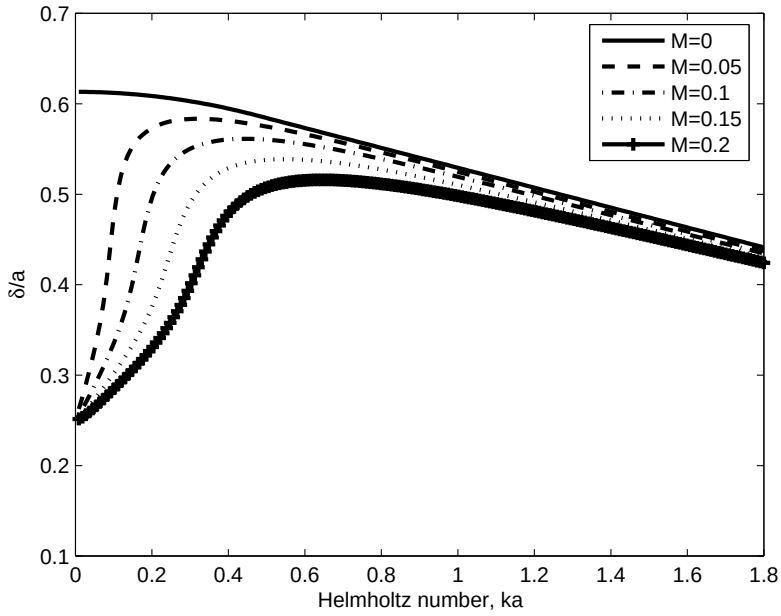

FIGURE 1.5: Rienstra's[5] prediction of the normalised acoustic end correction, δ/a, of a simple unflanged duct with different outflow Mach numbers as a function of ka.

Further modifications to the end correction are predicted by Rienstra [5, 6] when there is mean flow from the duct termination. Rienstra predicts that the end correction of a simple unflanged duct with outflow tends toward a Strouhal number limit of $\delta = 0.2554a\sqrt{1 - M^2}$. As well as this, Rienstra predicts a general decrease in the magnitude of the end correction with increasing flow velocity. The end correction predicted by Rienstra for a range of flow Mach numbers is plotted in figure 1.5. The low Strouhal number collapse predicted is supported by published results of Peters [20], though the results indicate that the low Strouhal number limit is $0.19a$ for a/b ratios of 1, 0.85, & 0.7. However, experimental results by Allam [21] for a/b=0.875 suggest the low frequency limit is in fact closer to $0.25a$ as predicted by Rienstra. Obviously some confusion exists over the effect of the duct wall edge thickness and outflow on the end correction due to conflicting published work. Since the magnitude of the end correction can be a significant proportion of the total length of a duct when the duct length is relatively short or the duct

diameter large it is considered important that it be clearly defined. In chapter 2 new measurements of this end correction are presented and compared with the previously published literature.

1.4 Measurement of aeroacoustic properties in ducts with flow

In order to determine the aeroacoustic properties it is essential that precise measurements of the magnitude and phase of the pressure wave components are taken. A number of techniques for measuring for determining these components are available. These include the impedance tube technique, the two microphone wave decomposition technique and the multi-microphone wave decomposition tecnique.

1.4.1 Impedance tube technique

The impedance tube technique is an experimental method to assess the acoustic properties of ducts at frequencies at which the wave motion is substantially one-dimensional. The technique involves traversing a microphone axially inside the duct and recording the acoustic signal at the microphone as a function of position [23, 28, 29]. This allows the standing wave (SW) ratio to be determined which in turns allows the travelling wave amplitudes at a given position to be determined.

Alfredson and Davies implemented the technique to assess the acoustic field inside a simple engine exhaust pipe [28]. In the paper the technique was implemented to determine the pressure reflection coefficient of the tailpipe termination as well as the net energy flux in the tailpipe with flow. The results indicate the method is valid in the presence of mean flow for determining such quantities. Alfredson and Davies also implemented the technique to assess the acoustic performance of a number of silencer components [23]. The results were compared with those predicted by a one-dimensional linear theory for sound propagation in exhaust systems with mean gas flow.

In the presence of mean flow in the duct system the microphone probe can interfere with the flow field, which can affect the signal-to-noise ratio of the results. This can be overcome to some degree if the probe is slid flush along the duct wall [30].

There is also difficulty in accurately locating the pressure maxima, particularly if there is jitter [31], though this may be somewhat overcome by interpolating from successive minima [32] or using a least squares procedure [33, 34].

Further severe limitations with this technique are apparent. Long measurement tubes are required to determine the SW pattern at low frequencies and only straight through silencers may be evaluated, as an open passage is required to axially traverse the pressure transducer through the duct. Further to this the technique is labourious and time-consuming with the experiment required to be repeated for each frequency of interest.

1.4.2 Two microphone wave decomposition technique

The two-microphone wave decomposition technique was first introduced in the 1970's along with the development of digital signal acquisition and processing. The technique consists of acquiring pressure time histories from a pair of microphones mounted flush with the inner wall of the duct. The method allows for the determination of acoustic characteristics within the duct from the cross-spectrum [35, 36] or the transfer function [37, 38] between the two microphone signals.

Seybert and Ross[35] published a paper presenting an assessment of the technique in a simple duct with broadband acoustic excitation. They concluded that the results from the two-microphone method compared favourably with that of the impedance tube technique highlighting the considerable savings in time and labour. The paper also discusses the importance of relative phase and magnitude calibration of the pressure transducers. The results indicate the technique is error prone at frequencies equivalent to multiples of one half wavelength.

Chung and Blaser [37] presented a transfer function method of measuring normal incident induct acoustic properties. The issue of relative phase and magnitude calibration is also discussed with a sensor switching calibration technique proposed as an appropriate solution to the problem. A companion paper by the same authors [38] tested the technique in a simple duct with no flow. The method was implemented to measure the pressure reflection coefficient of an unflanged duct with flow. Comparison of the results with those from the impedance tube technique as well as theoretical predictions indicated the method was valid. The paper also validates the sensor switching calibration procedure by comparing the calibrated

and uncalibrated transfer function of two signals with artificial distortion on one channel with the transfer function of two signals with no artificial distortion.

Bhattacharya[39] reported the testing of the method with mean flow in a duct in his PhD thesis. The thesis verifies that the technique provides results that were at least as reliable as the impedance tube technique. It emphasises the importance of appropriate selection of transducer spacing with respect to the frequency range of interest for obtaining reliable results. The thesis concludes that the technique is useful for experimentally determining the characteristics of silencer units with flow. Bento Coelho [40] used the technique to assess the acoustic characteristics of silencers with a perforated bridge across the chamber of different porosity. In his thesis he also points at the possibility of implementing the technique in the identification of sources in ducts arising from flow acoustic interaction.

More recently Holland and Davies [41] and Holland et al [42] implemented the technique to measure the sound power flux in ducts with flow. The publications indicate the issues with measurement of the sound power flux in such duct systems due to the high levels of flow noise. Such signal-to-noise ratio issues are overcome by using a slow sine sweep and a selective averaging technique rather than conventional broadband excitation. The signal-to-noise ratio can be further improved by implementing a coherence function method to remove uncorrelated noise from the results [43, 44].

Overall, the two-microphone wave decomposition technique can be considered a tried and tested method of measuring the acoustic characteristics of a duct with flow. It is important to note that relative calibration of the microphones is essential to obtain meaningful results. The technique is advantageous over the impedance tube technique as it offers considerable time saving. Unlike the impedance tube technique it causes minimal interference to the duct flow and acoustic field. As well as this, the two microphone method is capable of obtaining data for very low Helmholtz numbers, at which the standing wave method does not yield accurate results [28]. It is also possible to improve the signal-to-noise ratio by using a slow sine-sweep as the excitation signal and implementing a selective averaging technique rather than conventional broadband excitation. It is deemed possible to use the technique to identify aeroacoustic sources in ducts with flow.

1.4.3 Multi-Microphone wave decomposition technique

In the two-microphone wave decomposition technique it is assumed that there is only two unknowns to be determined from the pressure time histories, namely, the forward and backward pressure wave components in the duct. However, if there are more unknown parameters a multi microphone technique must be implemented with the number of microphone positions at least equal to the number of unknowns. If more microphone positions than the number of unknowns are used then a non-linear regression technique [45] can be used to solve the resulting set of overdetermined non-linear equations.

Ronneberger and Ahrens [45] implemented a multipoint microphone technique and non-linear regression processing procedure to determine the wall shear stress and viscothermal attenuation coefficient in a duct with flow. A similar technique was implemented by Peters et al [20] to determine the damping and reflection coefficients on an open pipe at low Mach and low Helmholtz numbers. The paper concludes that the technique can determine the reflection coefficient to an accuracy of 1% and damping coefficient to within 2%. Comparison of the results with those obtained using the two microphone and SWR technique as well as theoretical predictions reinforce this conclusion. More recently Allam [21] similarly applied a multi-point microphone technique to assess the aeroacoustic characteristics of a simple unflanged duct with flow.

The multi-microphone wave decomposition technique seems a powerful method for assessing the aeroacoustic properties of simple ducts with flow under plane wave conditions. However, it should be noted that the length of duct required for an appropriately spaced array of microphones may be in excess of that available in typical expansion chamber geometries.

1.5 Aeroacoustic sources in ducts with flow

Sound generation typically occurs with high speed flows consisting of turbulent fluid motion in which a certain amount of kinetic energy is transferred to an acoustic field. Since the acoustic energy represents only a small fraction of the energy in the flow the direct prediction of such sound generation can be difficult. Lighthill [46, 47] considers the sound field generated under such turbulent conditions to

be a small perturbation of the flow to provide an analogy between the turbulent fluctuations and an acoustic source. One important prediction from Lighthill's analogy is that the acoustic power radiated to the far field by a free turbulent isothermal jet scales as the eight power, U^8, of the jet velocity. Lighthill's analogy was extended by Curle [48] to incorporate the presence of a fixed boundary within the flow. Curle's analysis indicates that a flow field will generate a dipole sound field as a result of the unsteady hydrodynamic forces acting on a surface. The acoustic power generated by such a sound field scales as the sixth power, U^6, of the flow velocity. In practice the velocity dependence varies from system to system between U^4 and U^8. Such variability reinforces the need for experimental results for individual systems.

With regards to the spectral characteristics of internal flows, what should be considered is the potential of feedback from the acoustic field. This feedback is inherent in Howe's vortex sound theory[49] which indicates that the acoustic power generated by flow is at a maximimum when high levels of vorticity couple with the kinetic part of the acoustic field. This theoretical insight is supported by apparent coupling of acoustic resonances to periodic flow disturbances resulting from an instability flow disturbance. This process has been identified in wind instruments [50, 51], wall cavities[52], side-branches[53], and expansion chambers [54]. In addition to the effect of the acoustic field on the frequency characteristics of these sources, Hardin et al [55] indicates a Strouhal number dependent source. Comparison of the Hardin et al's model with results published by Nelson et al [56] seems to validate this Strouhal number dependence. However, the majority of research seems to indicate that the frequency characteristics of the source of internal flows is primarily determined by the geometry of the system rather than the Strouhal number. Whereas the acoustic power radiated by the sources seems proportional to the flow velocity, as previously discussed. It was also discovered that the source characteristics can be modified by seemingly slight changes in the system geometry. Bruggeman et al's [53] analysis of the aeroacoustic behaviour of ducts with closed side-branches indicated that the aeroacoustic source amplitude decreases by replacing a round edge T-joint side branch with one with sharp edges.

A number of methods have been employed over the years to measure the source characteristics of internal flows. Nelson and Morfey's [57] measurements of sound production by a spoiler in a duct with low velocity flow indicate that the acoustic power generated scales in a similar fashion to that of the dipole source distribution

presented by Curle above the cut-on of the first higher order mode. However, at frequencies below the cut-on frequency of the first higher order mode, the presence of the duct drastically modifies the radiation with a consequent U^4 velocity dependence of the radiated sound power. This result, however, conflicts with measurements by other authors such as Gordon [58, 59] whose experimental results of the power radiated from spoiler generated flow noise in a duct scaled as the sixth power of the flow velocity at frequencies below the cut-on frequency, whereas he found it scaled to the eight power of the flow velocity above the cut-on frequency. Obviously, the dependence of an aeroacoustic source on the flow velocity in a duct lacks clarity.

1.5.1 Expansion chamber aeroacoustic source measurements

Relatively sparse published research exists with respect to aeroacoustic sources in expansion chambers. Davies and Holland [54] indicate that acoustically controlled vortex shedding in an expansion chamber can act as a major source of sound generation. Further to this, they state that the spectral characteristics of the source is dominated by the acoustic resonances of the system, most notably the tailpipe and the chamber resonances. Davies and Holland [60] published some results of sound radiated from flow excited expansion chambers for a range of mean Mach numbers below 0.4. Analysis of the results indicate that the acoustic power radiated scales proportional to the mean flow velocity, raised to a power lying between 4 and 6. The paper also presents a plot of the power spectrum of the radiated sound power identifying the tailpipe and chamber resonances. Desantes et al [8] assesses the flow noise generation in a simple expansion chamber experimentally as well as developing simple computational models of the flow. Their analysis indicates the aeroacoustic source associated with flow through an expansion chamber exhibited dipole like behaviour similar to that determine by Nelson and Morfey [57] for a spoiler in a duct.

1.5.2 Methods for aeroacoustic source measurement

Nelson and Halliwell [57] determined the aerodynamic noise generated by spoilers in low velocity flow ducts by measuring the sound power radiated from an open exhuast termination. A reverberation chamber was used to determine the sound

power radiated from the duct exit. The was performed for 1/3 octave band centre frequencies between 63Hz and 10kHz. Though the technique seemed successful by determining the power over 1/3 octave bands specific detail of the frequency characterisitics of the source are lost. In addition, only the source power radiated downstream from the spoiler is measured with no information of the source power radiated upstream gathered.

Gordon [58] similarly assessed the flow noise by a spoiler in a duct by measuring the sound power radiated from the duct termination. This was done by locating the duct termination in an anechoic chamber and surveying the radiated field by traversing with a microphone at a known radius from the duct termination. Using this the total radiated field is computed by integrating the square of the pressure measurements with respect to the relative directivity pattern for each frequency. This same method was used by Holland and Davies [41] for frequencies below the the cut-on of the first higher-order mode. In their experiment they used single microphone in an anechoic chamber at a fixed position and distance from the duct termination assuming a monopole type radiation pattern. Also assuming monopole radiation and in the abscence of a fully anechoic chamber, Torregrosa et al [61] used an intensity probe at a fixed radial position and angle from an exhaust termimation to assess the noise radiated from an IC engine exhaust system. This farfield microphone method seems to have its advantages particularly in avoiding signal-to-noise ratio issues associated with uncorrellated flow noise as the microphone is removed from the flow. However, it chooses to ignore the effect of the shear layer which forms at the duct exit on the acoustic power radiated, as well as this it fails to provide information of the sound power radiated upstream from the source or the sourec location.

Other methods of measuring the acoustic source detail within ducts tends to rely on microphones mounted flush with the inner wall of duct wall. Bruggeman et al's [53] analysis of self-sustained pressure pulsation associated with closed side branches in a duct with flow relied on a microphone positioned at the closed end of a side branch. Since this is a known pressure antinode this allowed the maximum pressure associated with the side branch pulsation to determinded. Ziada and Shine [62] also used this technique as well as numerous other authors [56, 62–66]. The technique has the advanatage of simplicity both in the experimental procedure and the processing of data. However, at low frequencies the duct system under investigation will consist of a series of pressure nodes and antinodes

irrespective of the source location. This will dictate spectral shape of acoustic pressure measurement. It addition the acoustic pressure spectrum will be a sum of all sources within the system rather than just the source of interest.

1.6 Conclusions

It has been discussed that sound propagation and generation in ducts is an important issue with regard to the structural integrity of gas transport systems as well as automotive exhaust systems and industrial exhaust stacks. The modeling of such systems requires a detailed knowledge of the effects of flow on the acoustic wave propagation within the duct and of the aeroacoustic source characteristics associated with common duct geometries. After a review of the current literature it can be concluded,

- The original research dealing with plane wave propagation in ducts with flow adopted an *ad hoc* formulation for the complex wave numbers. This *ad hoc* solution has since been superseded by Dokumaci's formulations for the propagation constants with flow. This suggest that the original research of the viscothermal attenuation coefficient may have weaknesses. Since the propagation of sound waves is dependent on the complex wave number it is important that the parameters which define it be known to a high level of precision. This justifies the need for an assessment of the viscothermal attenuation coefficient with flow employing Dokuamici's formulation.

- Flow affects the basic aeroacoustic characteristics of ducts including the pressure reflection coefficient of an unflanged duct termination and the acoustic end correction. Most importantly it seems the extent of vorticity shed at the open end of a duct plays an important role in the modification of the pressure reflection coefficient. However, to the authors knowledge, experimental evidence regarding this relationship between the vorticity and the pressure reflection coefficient of an unflanged duct termination has yet to be published.

- A review of the current techniques for measuring the aeroacoustic characteristics of ducts with flow at frequency below the cut-on of the first higher order mode suggest the two-microphone wave decomposition technique to be

a robust and reliable technique. In addition, the technique can be expanded to a multi-microphone method should further experimental unknowns be required.

- Vortex shedding plays an important role in the conversion of fluid kinetic energy to acoustical energy. More specifically, aeroacoustic sources in ducts are dependent the phase relationship of the vorticity and the kinetic part of the local acoustic field.

- There is a limited amount of published experimental results providing detailed source measurements. In addition, many published results of the acoustic power radiated from spoilers and orifices in a duct with flow disagree in the velocity dependence determined from the experimental results. Also, detail of the spectral characteristics is lost or not provided in the majority of the previous research reviewed.

This thesis provides a large body of experimental results regarding the viscothermal attenuation coefficient, pressure reflection coefficient and end correction of an unflanged duct with flow. In addition, and experimental technique for measuring the acoustic source power at frequencies below the cut-on of the first higher order mode is presented. The technique is employed to measure the aeroacoustic source power of an orifice plate and a simple expansion chamber. The measurements are compared throughout with published theories and empirical models.

1.6.1 Novel work

- A novel technique for determining the viscothermal attenuation coefficient with flow is presented in section 2.6. Experimental results determined using the technique are presented and compared with current published theory supporting the validity of the technique.

- In section 2.7 pressure reflection coefficient measurements for an unflanged duct with two different edge conditions with mean outflow are presented. The measurements are used in conjunction with a computational model of Rienstra and Munt's theoretical predictions to establish the extent of vorticity shed. The results establish the importance of the edge condition on

the extent of vorticity shed. In addition the importance of vorticity on the magnitude of the pressure reflection coefficient is highlighted.

- Measurement of the end correction of a simple unflanged duct with and without flow are presented for two different edge conditions. Though similar results have been presented in recently published literature [21] the effect of the edge on the magnitude of the end correction differs to that of previously published work.

- A novel technique for measuring the acoustic source strength in ducts with flow is presented in section 3.5. The method is valid for frequencies below the cut-on of the first higher order mode and is verified experimentally for a range of frequencies and amplitudes by creating an artificial source in a duct.

- In section 4.4 an expression for the acoustic power loss at an expansion in a duct is derived. The expression is limited to frequencies below the cut-on of the first higher order mode. The expression highlights the dependence of the amount of absorption on the local acoustic phase. Most importantly, that the absorption will be highest at frequencies corresponding to pressure nodes immediately downstream of the expansion. Predictions of the amount of absorption from flow through an in-duct orifice are compared with experimentally results.

- Measurement of the aeroacoustic source strength of an in-duct orifice determined using the novel technique described in chapter 3 are presented in chapter 4. The results are used to determine the spectral characteristic and velocity dependence of the source. The results indicate that the duct-to-orifice area ratio has a important effect on the spectral characteristics and velocity dependence of the source.

- A describing function method presented by Mast and Pierce [67] for modeling flow excited resonators is adopted and modified to model a flow excited expansion chamber.

- New measurements of the aeroacoustic source strength of a simple flow excited expansion chamber are presented in chapter 5. The results indicate that lock-on flow tones occur when hydrodynamic modes which form in the chamber match the tailpipe resonant frequencies.

- The determined lock-on flow tones are compared with the frequencies predicted using describing function theory. The measurements and theory match well, supporting the validity of the theory.

Chapter 2

Measurement of the plane wave aeroacoustic characteristics in ducts with flow

2.1 Introduction

This chapter provides an overview of the experimental techniques adopted to determine the pressure wave components in a duct with steady mean flow along with detail of the experimental set-up developed.

The techniques are implemented to assess the aeroacoustic characteristics of a simple exhaust pipe, specifically the viscothermal attenuation coefficient, the plane wave reflection coefficient and acoustic end correction of a simple unflanged duct with flow. The novel aspect of these measurements include a 4 microphone technique developed for determining the viscothermal attenuation coefficient, as well as the employment of the plane wave pressure reflection coefficient results to determine the extent of vorticity shed from an unflanged cylindrical duct with flow with two different conditions. The results from the technique are presented and discussed with regard to relevant published literature.

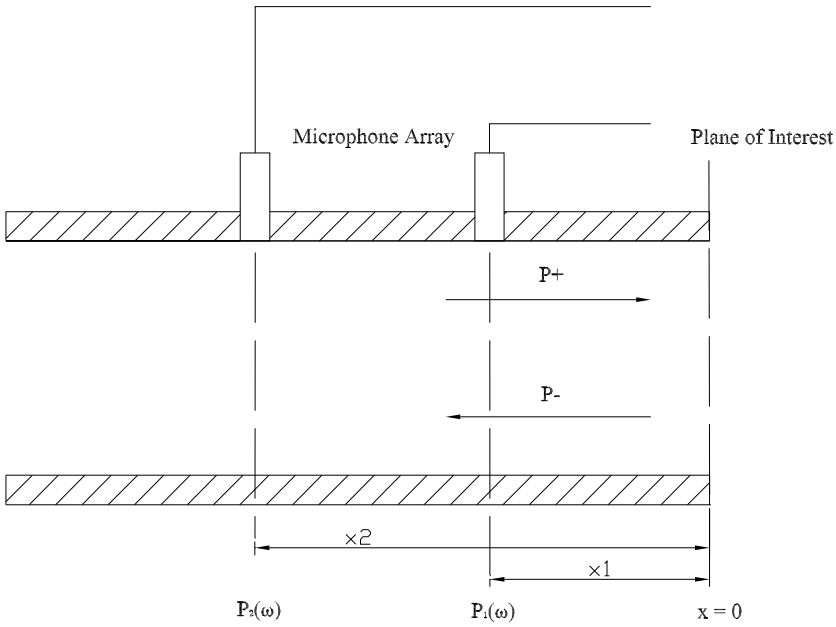

FIGURE 2.1: Simple Duct Termination

2.2 Calculation of sound field components

The plane wave pressure components are determined in similar fashion to that presented by Holland and Davies[41]. Here the pressure wave component spectra are determined from the autospectra, cross spectra and transfer functions between a pair of microphones located flush with the inner wall of the duct system under investigation. Considering such a pair of miniature microphones labeled 1 and 2, located at x_1 and x_2 respectively, and arbitrarily assigning $x = 0$ at the cross sectional plane of interest (see Figure 2.1). The pressure at each microphones may be written as

$$\hat{p}_1(x,\omega) = \hat{p}_0^+ e^{-j\hat{k}^+ x_1} + \hat{p}_0^- e^{j\hat{k}^- x_1}, \tag{2.1}$$

$$\hat{p}_2(x,\omega) = \hat{p}_0^+ e^{-j\hat{k}^+ x_2} + \hat{p}_0^- e^{j\hat{k}^- x_2}. \tag{2.2}$$

Let G_{22} be the autospectrum of the pressure at position 2 defined as

$$G_{22} = \hat{p}_2 \hat{p}_2^* = \left(\hat{p}_0^+ e^{-j\hat{k}^+ x_2} + \hat{p}_0^- e^{j\hat{k}^- x_2}\right)\left(\hat{p}_0^+ e^{-j\hat{k}^+ x_2} + \hat{p}_0^- e^{j\hat{k}^- x_2}\right)^*. \tag{2.3}$$

Where * represent the complex conjugate. The cross spectrum, $\hat{G}_{12}$, between the pressures at microphones 1 and 2 is defined as

$$\hat{G}_{12} = \hat{p}_1\hat{p}_2^* = \left(\hat{p}_0^+ e^{-j\hat{k}^+x_1} + \hat{p}_0^- e^{j\hat{k}^-x_1}\right)\left(\hat{p}_0^+ e^{-j\hat{k}^+x_2} + \hat{p}_0^- e^{j\hat{k}^-x_2}\right)^*. \tag{2.4}$$

Dividing $\hat{G}_{12}$ by G_{22} yields

$$\frac{\hat{G}_{12}}{G_{22}} = \frac{\left(\hat{p}_0^+ e^{-j\hat{k}^+x_1} + \hat{p}_0^- e^{j\hat{k}^-x_1}\right)}{\left(\hat{p}_0^+ e^{-j\hat{k}^+x_2} + \hat{p}_0^- e^{j\hat{k}^-x_2}\right)}. \tag{2.5}$$

The complex reflection coefficient at $x = 0$ can be written as

$$\hat{R} = \frac{\hat{p}_0^-}{\hat{p}_0^+}. \tag{2.6}$$

Dividing above and below of equation 2.5 by $\hat{p}_0^+$ gives

$$\frac{\hat{G}_{12}}{G_{22}} = \frac{e^{-j\hat{k}^+x_1} + \hat{R}e^{j\hat{k}^-x_1}}{e^{-j\hat{k}^+x_2} + \hat{R}e^{j\hat{k}^-x_2}}. \tag{2.7}$$

Rearranging this, it can be observed that the reflection coefficient at $x = 0$ may found by the two measured quantities , $\hat{G}_{12}$ and G_{22}, and the known values of k, M and α. The complex reflection coefficient can thus be written as

$$\hat{R} = -\left\{\frac{\hat{G}_{12}e^{-j\hat{k}^+x_2} - G_{22}e^{-j\hat{k}^+x_1}}{\hat{G}_{12}e^{j\hat{k}^-x_2} - G_{22}e^{j\hat{k}^-x_1}}\right\}, \tag{2.8}$$

which is equivalent to

$$\hat{R} = -\left\{\frac{\hat{H}_{12}e^{-j\hat{k}^+x_2} - e^{-j\hat{k}^+x_1}}{\hat{H}_{12}e^{j\hat{k}^-x_2} - e^{jk^-x_1}}\right\}, \tag{2.9}$$

where $\hat{H}_{12} = \frac{\hat{p}_1}{\hat{p}_2} = \frac{\hat{G}_{12}}{G_{22}}$ is the transfer function between locations 1 and 2. Using the definition of $\hat{G}_{22}$ and $\hat{R}$ it can be shown that the incident wave component at $x = 0$ is

$$\left|\hat{p}_0^+\right| = \frac{(\hat{G}_{22})^{\frac{1}{2}}}{\left|e^{-j\hat{k}^+x_2} + \hat{R}e^{j\hat{k}^-x_2}\right|}, \tag{2.10}$$

and that the reflected wave component is

$$\hat{p}_0^- = \hat{R}\left|\hat{p}_0^+\right|. \tag{2.11}$$

Arbitrarily assigning $x_1 = 0$ provides the magnitude of the pressure wave components at transfer plane $x_1 = 0$. The fact that this only provides the modulus of $\hat{p}_1^+$ is irrelevant as the phase of $\hat{p}_1^+$ can arbitrarily be chosen as zero with no loss in generality, whilst $\hat{p}_0^-$ is generally complex.

2.3 Data acquisition and analysis method

The wave decomposition method described in section 2.2 considers a system in which the acoustic excitation is harmonic. In this situation the linear spectrum (LS) provides spectral peaks equivalent to RMS value of the harmonic signals present in the measured time series and is relatively independent of frequency resolution. However, if the character of the acoustic system is primarily random in nature the spectral magnitude of the linear spectrum will vary with the frequency resolution chosen. In this situation the magnitude of the power spectral density (PSD) remains relatively independent of the frequency resolution chosen. Consequently, when comparing signals primarily random in nature it is preferable to use the PSD rather than the linear spectrum or power spectrum (LS^2), whereas if the signals are primarily harmonic in nature it is better to use the linear spectrum. Obviously a conundrum exist when deciding how to present the data if it is a combination of harmonic and random signals. The key to all this is the relationship between the linear spectrum and the PSD;

$$LS = \sqrt{PSD \times ENBW} \tag{2.12}$$

where $ENBW$ is the effective noise bandwidth which is defined as the normalised effective noise bandwidth (NENBW) times the spectral binwidth, f_{res}. The normalised effective noise bandwidth is a function of the window type [68] employed

in the analysis. Therefore so long as the ENBW is known one can convert from PSD to LS and back again. As shall be seen later in this thesis when the system of interest is excited via a loudspeaker a sine sweep is employed and so the measured signals are considered primarily harmonic. When assessing the aeroacoustic sound generation from an in-duct orifice and a simple expansion chamber the source characteristics are a combination of tonal and broadband. However, since the tonal sources were found to dominate the system was also considered primarily harmonic. Despite this assumption the relationship between the linear spectra and the PSDs (i.e. ENBW) is specified the same for all the analysis.

For the experimental results presented in this thesis output signals from the microphone amplifier used are acquired using a National Instruments (NI) PXI-4472 8 channel 24bit acquisition card. The card is mounted in a NI 1042 PXI chassis with a Windows XP operating system. A LabView programme was specifically written for data acquisition. Unless stated, all data is acquired at a sampling rate, f_s, of 44.1kHz and written to a hard disk in 32 bit floating point format. Using specifically written Matlab code the data from each channel is converted to the frequency domain via a Fast Fourier Transform with an FFT window length of 32768. The resulting transforms are used to create the autospectra, cross spectra and transfer functions necessary to determine the spectral wave components with a spectral binwidth of 1.3458Hz. A Hanning window with a 50% overlap is implemented in the averaging of data. The NENBW of a Hanning window is 1.5 bins which in turn provides a ENBW of 2.0187 for the spectra determined.

2.3.1 Anti-aliasing filters

To avoid aliasing in the control system, one must remove all higher frequency signal components above the Nyquist frequency. The Nyquist frequency is equivalent to half the sampling frequency f_s. The National Instruments PXI-4472 signal acquisition cards used have both analog and real-time digital filters implemented in the hardware to prevent aliasing. Input signals are first passed through fixed analog filters to remove any signals with frequency components beyond the range of the ADCs. The inbuilt digital anti-aliasing filters then automatically adjust their cutoff frequency to remove any frequency components above half the programmed sampling rate.

2.3.2 Sine-sweep/selective averaging technique

It was decided not to use a white noise signal to excite the system. Holland and Davies [41] demonstrate the poor signal to noise ratio which results from acoustically exciting a duct system with flow with white noise. Since both white noise and boundary layer noise are random it is difficult to separate the two. To overcome this issue a slow sine sweep was adopted instead of white noise. By acquiring the sweep signal simultaneously with the microphone output signals it is possible to exclude from the averaging process all signals except those within a narrow frequency band around the excitation frequency. This method is referred to as selective averaging. Holland and Davies show that using sweep sine excitation and selective averaging it is possible to separate the acoustic signal from the boundary layer noise and thus provides a much higher coherence function (coherence ≈ 1) even when the signal to noise ratio is much less than unity. The selective averaging technique also ignores any higher harmonics of the fundamental frequency created as a result of non-linearity. Figure 2.2 plots the coherence of measurements using

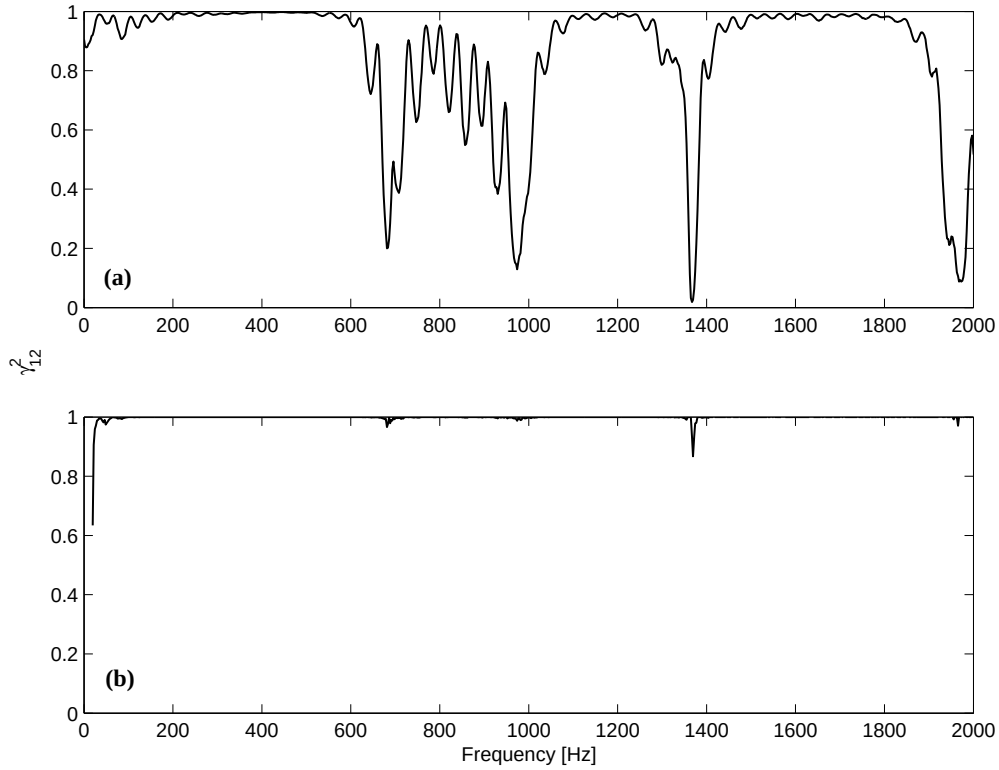

FIGURE 2.2: Coherence between microphone pair in a duct with a mean flow Mach number of 0.1. (a) Broadband excitation (b) Sine-sweep excitation with selective averaging technique.

a pair of microphones in a simple duct with flow using both broadband excitation

and a sine-sweep/selective averaging technique. The mean flow Mach number in the duct was 0.1. It can be clearly seen that the sine-sweep/selective averaging technique achieves a more desirable coherence level over the whole frequency range of interest.

2.3.3 Calibration procedure

The acoustic fields within the systems of interest are typically highly reactive. For this reason the phase and hence the imaginary part of the cross spectra is very close to zero over much of the frequency band. In order to ensure precise calibration of both the relative magnitude and phase between microphones a sensor switching method [37, 38, 41, 69] is adopted. The pressure, p, at a given frequency at

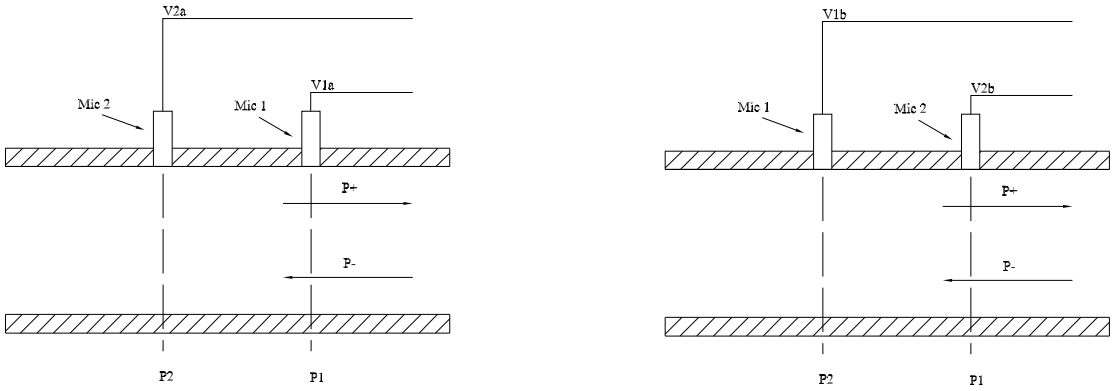

FIGURE 2.3: Phase and relative magnitude calibration using a sensor switching technique.

each microphone location can be considered as the measured voltage output, V, multiplied by some calibration factor, C. For the two configurations a and b as described in figure 2.4 it follows;

$$p_1 = C_1 V_{1a} = C_2 V_{2b}, \tag{2.13}$$

$$p_2 = C_2 V_{2a} = C_1 V_{1b}, \tag{2.14}$$

letting $H = \frac{p_1}{p_2} = \frac{C_1 V_{1a}}{C_2 V_{2a}} = \frac{C_2 V_{2b}}{C_1 V_{1b}}$ and manipulating the equations provides the calibration factor for configuration a as

$$C = \frac{C_1}{C_2} = \frac{V_{2a} V_{2b}}{V_{1a} V_{1b}}. \tag{2.15}$$

Thus, the calibrated transfer function H_c for configuration a is defined as $H_c = \frac{V_{1a}}{V_{2a}} \times C$. A typical calibration factor for the transfer function between an induct microphone pair with a microphone spacing of 75mm is illustrated in figure 2.4. This microphone spacing was choosen as it allowed for a frequency range of up to approximately 2200Hz to be assessed without discontinuities in the measurements occuring. These discontinuities occur at frequencies which approach the half wavelength of the microphone spacing [70]. It is apparent from figure 2.4 that both the magnitude and phase of the calibration factor is a smooth function of frequency. The minor spikes at approximately 800Hz, 1150Hz and 1650Hz are associated with low signal-to-noise ratios due to pressure nodes existing at the microphone measurement planes within the duct. More examples of such calibration functions are plotted in Appendix A.1. In order to obtain actual pressure values for the acquired

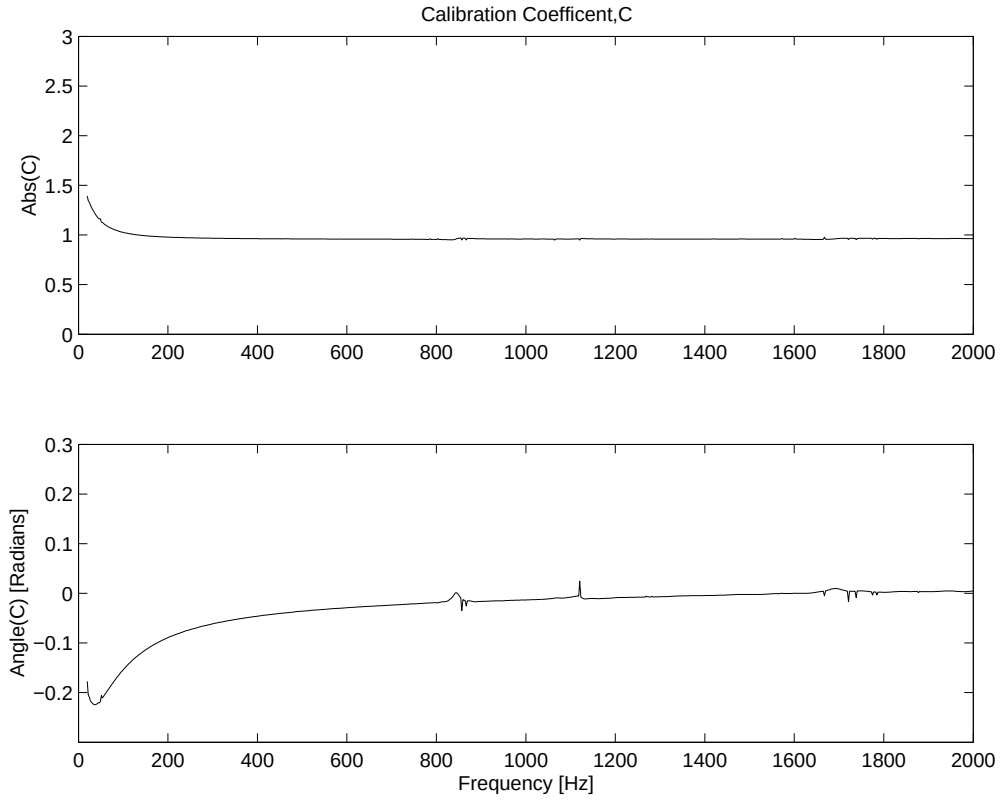

FIGURE 2.4: Typical calibration coefficient between two induct microphones.

data absolute calibration of just one of the microphones is necessary. This is done by using a Bruel and Kjaer piston phone set at 124dB.

2.4 Experimental Set-up

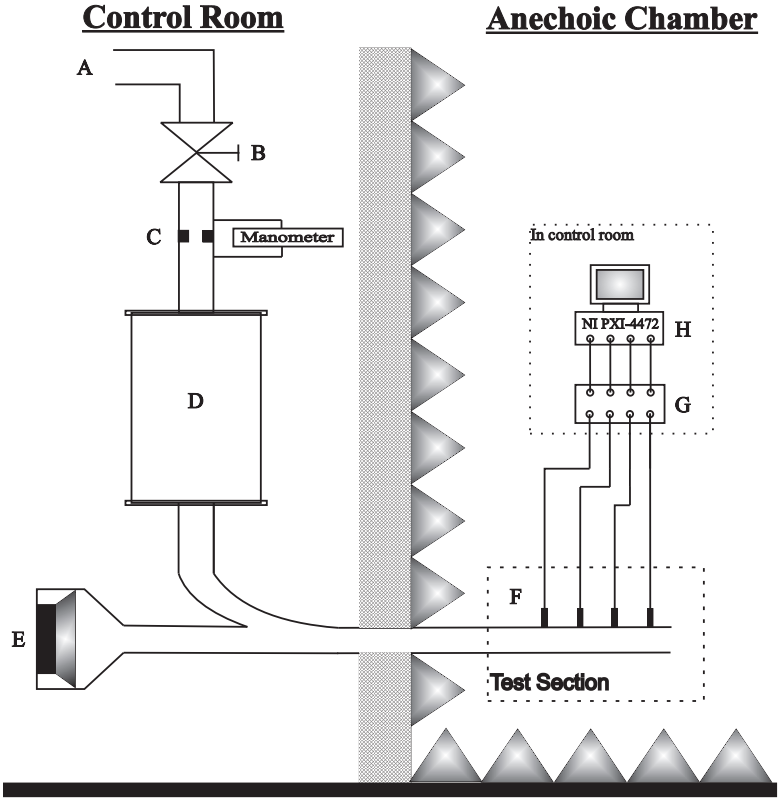

FIGURE 2.5: Experimental Rig : (A) ISVR high pressure supply, (B) Flow control valve, (C) Orifice plate, (D)Absorptive flow silencer, (E) Loudspeaker, (F) Knowles Electronics CA-8374 microphones, (G) Charge amplifiers, (H) Data acquisition system.

In order to investigate flow acoustic characteristics in a variety of different systems a multi-purpose rig capable of being easily adapted was developed and assembled in the ISVR Doak Lab. The test section and microphones were located in an anechoic chamber with dimensions 10.6m x 6.4m x 9m. Acoustic excitation was provided by means of a compression driver coupled with the duct system and located in a separate room to that of the anechoic chamber in order to isolate any noise being radiated from the speaker casing from the test section. Air flow was provided by the ISVR high pressure air supply typically with a 6 bar line pressure. The mass flow rate through the system was controlled using a Fisher control valve. This was controlled further via a tuning valve. The flow was passed through a

large absorptive silencer to attenuate any aeroacoustic noise generated prior to entering the test section. The connections to the ISVR air supply and to and from the silencer have an internal diameter of 40mm. Thus, for ease of connectivity and to prevent any unwanted discontinuities this internal diameter was adopted as the default value. The sound pressure time-histories were measured using Knowles

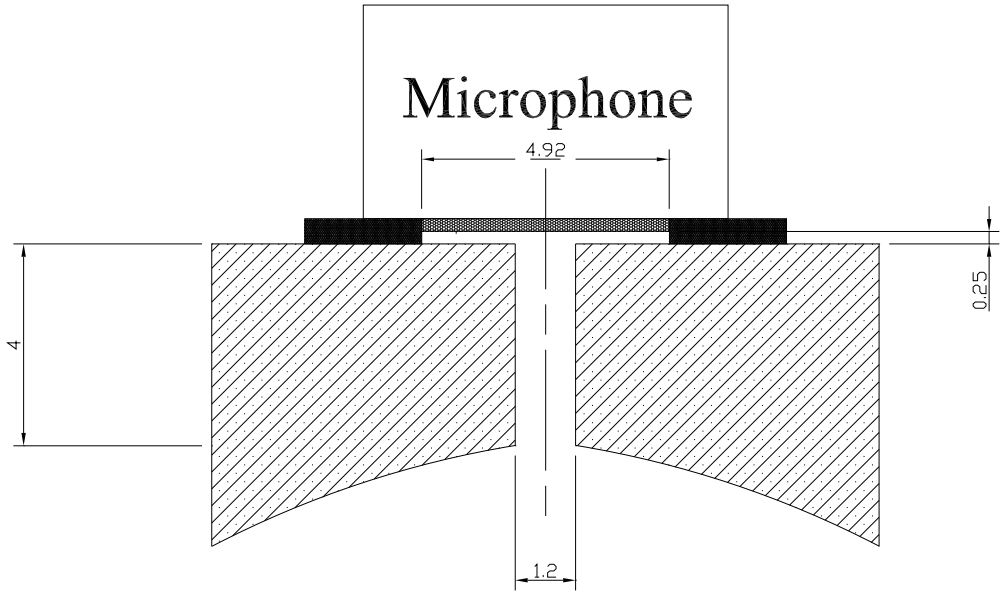

FIGURE 2.6: Configuration of pressure gauges in duct wall. All dimensions in millimeters

Electronics CA-8374 high performance microphones capable of measuring sound pressure levels of up to 152dB thus making them suitable for the high sound pressure levels in highly reactive duct systems. The microphones have a typical sensitivity of -72dB relative to 1 Volt/0.1 Pa. Each microphone is mounted in a specifically designed holder which sits in the duct wall. The geometric configuration of the microphone holders is shown in figure 2.6. The microphone holders have a Helmholtz resonant frequency of approximately 18.7 kHz and a quarter wave resonant frequency of approximately 21 kHz, both of which are considerably above the maximum frequency of interest.

2.4.1 Measurement of mean flow velocity

In order to measure the mean flow velocity an orifice plate was designed and constructed. The orifice plate consisted of a thin sheet of aluminium with a hole in the middle as described by figure 2.7 fitted between a flanged connection in the main pipe. Pressure tappings are located a distance D upstream and $D/2$ downstream of the orifice plate where D is the main pipe diameter. The volumetric flow rate, $\dot{Q}$, can then be determined using [71]

$$\dot{Q} = C_d S_o \left[\frac{2\Delta \bar{P}}{\rho(1 - (D_o/D)^4)} \right] \tag{2.16}$$

where $\Delta \bar{P}$ is the differential pressure across the orifice plate, S_o is the orifice hole cross sectional area, D_o is the orifice plate hole diameter. C_d is a dimensionless quantity known as the discharge coefficient that takes account of any viscous losses and vena contracta effect and is typically determined by calibration. The orifice plate was calibrated by measuring the velocity profile across the duct for a number of orifice differential pressures. This allowed for the volumetric flow rate to be calculated and which in turn allowed for C_d to be determined using eqn 2.16. Examples of the flow profile measured for different orifice differential pressures are plotted in figure 2.9.

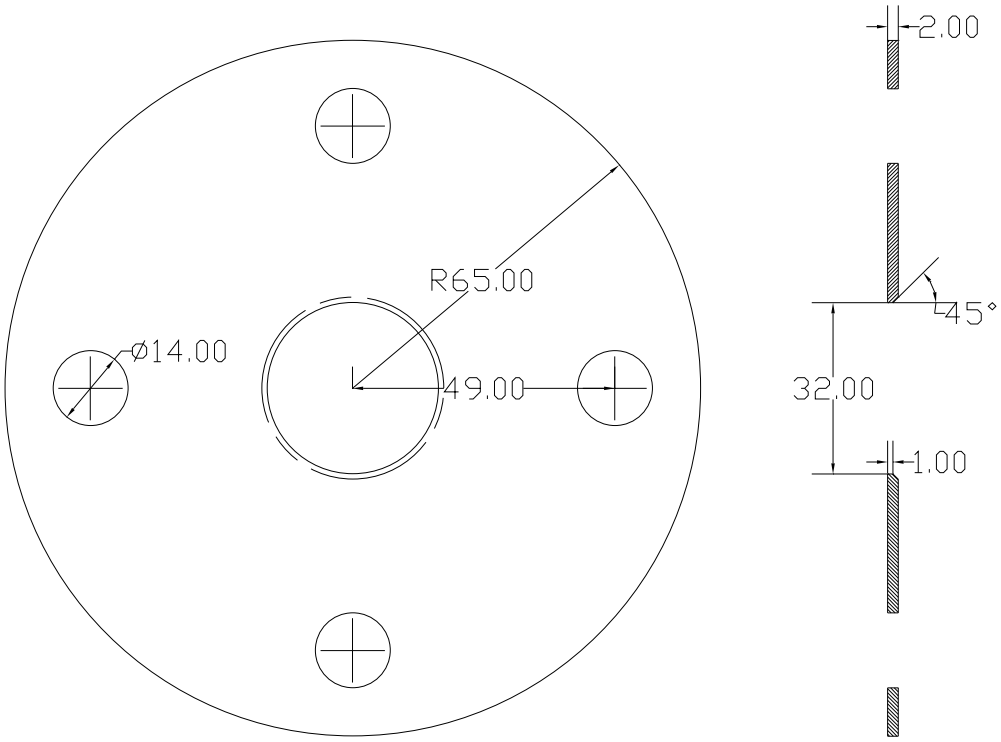

FIGURE 2.7: Orifice plate to sit within the duct flanges

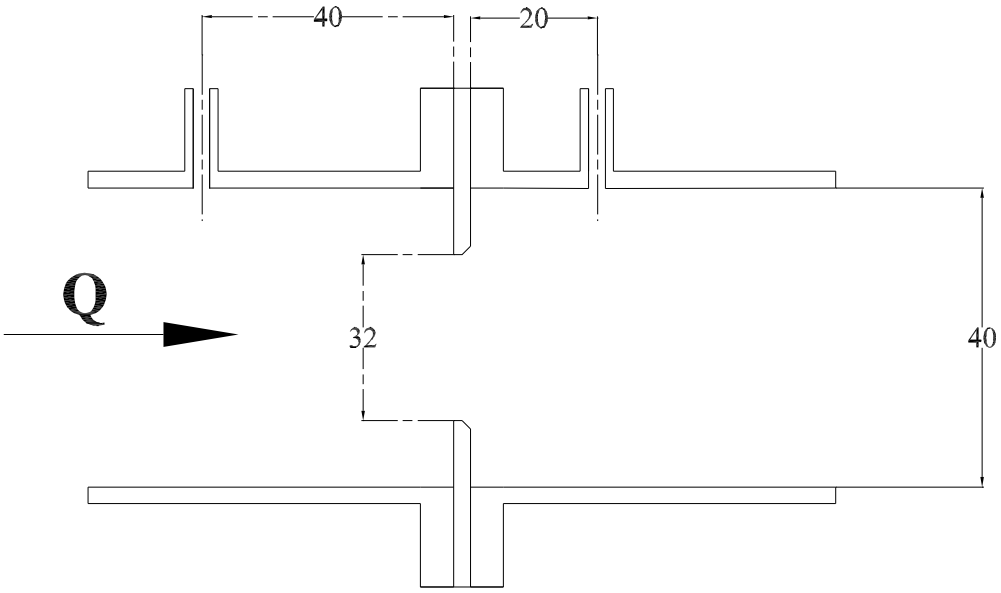

FIGURE 2.8: Orifice plate configuration. Dimensions in mm.

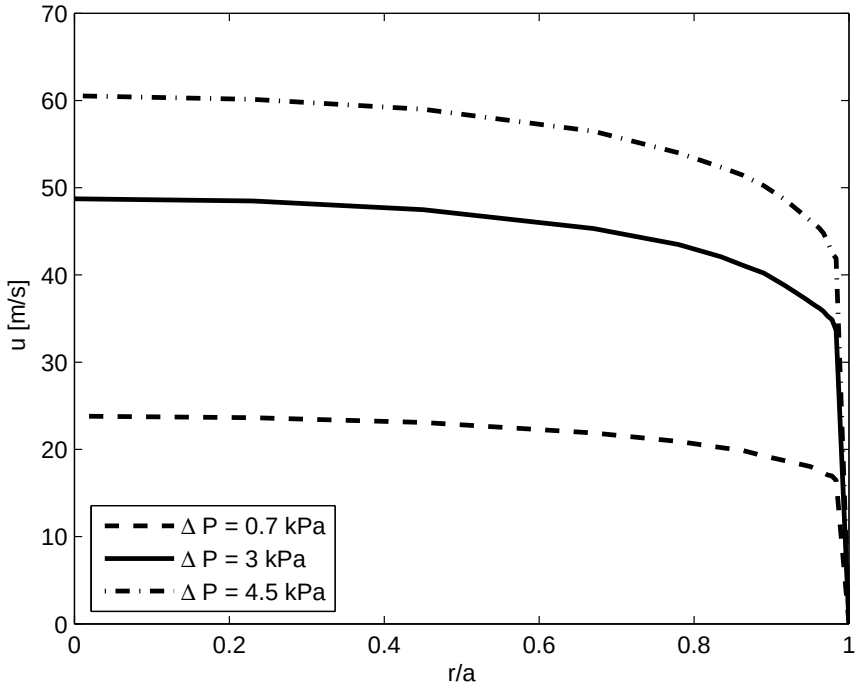

FIGURE 2.9: Flow Profile from duct centre axis to duct wall for different orifice differential pressures.

2.5 Error analysis

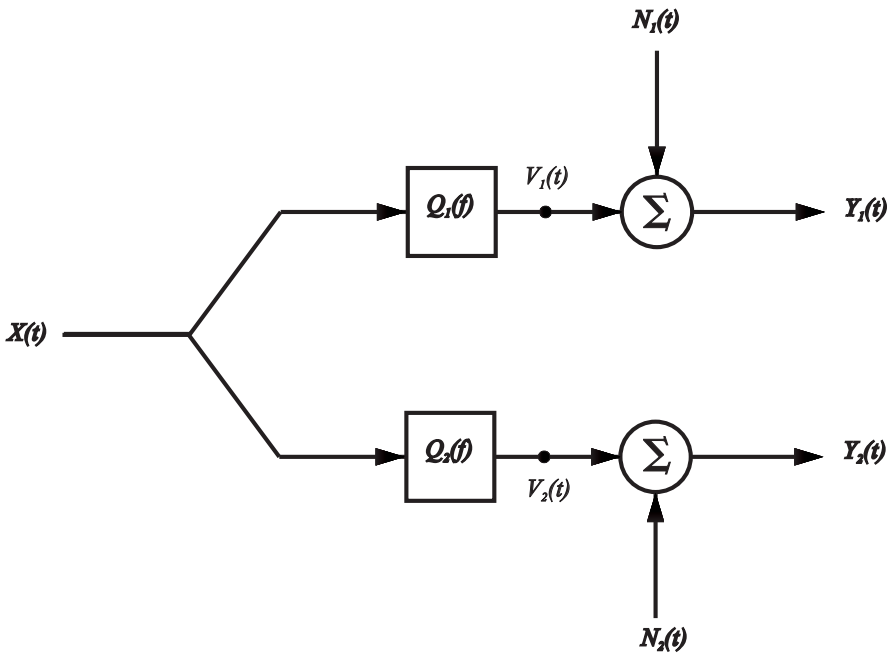

FIGURE 2.10: Single-input/two-output system

Figure 2.10 describes a single-input/two-output system. Such a model can be used to describe the two-microphone measurement method implemented for the estimation of in duct acoustic properties such as the reflection coefficient, end correction, and impedance. In such a system the input $X(t)$ represents the acoustic system and is considered unknown. $Q_1(f)$ and $Q_2(f)$ are simply the frequency response function of each channel. $V_1(t)$ and $V_2(t)$ represent the desired measured data from the two microphones as a function of time t. The measurements are assumed to be affected by extraneous noise, $N_1(t)$ and $N_2(t)$. Such noise sources are assumed to be uncorrelated with each other and with the input $X(t)$. It is assumed that any systematic error in the system is removed using appropriate phase and amplitude calibration of the system prior to each experiment. The error affected time series measurements, $Y_1(t)$ and $Y_2(t)$, provide a number of estimates that can be made by transforming the signals into the frequency domain via Fourier analysis. Such estimates include the autospectrum $G_{11}(f)$, the cross-spectrum $\hat{G}_{12}(f)$, the transfer function $\hat{H}_{12}(f)$, and the coherence function $\gamma^2_{12}(f)$ between the outputs, $Y_1(t)$ and $Y_2(t)$. The coherence function is an indication of how linearly correlated two quantities are, such that it equals one when the quantities are totally correlated and zero when they are not correlated at all. The

coherence is defined as [43]

$$\gamma_{12}^2(f) = \frac{\left|\hat{G}_{12}(f)\right|^2}{G_{11}(f)G_{22}(f)}. \tag{2.17}$$

For such a system the normalised random error, ϵ_r, in the estimates of interest can typically be described as a function of spectral averages n_d and the coherence γ_{12}^2 such that the error in the estimates tend to zero as n_d tends to infinity and/or γ_{12}^2 tends to one [43]. The normalised random error, ϵ_r, in autospectrum, cross spectrum and transfer function estimates is defined by Bendat & Piersel[43] as;

$$\epsilon_r\left[G_{11}(f)\right] = \frac{1}{\sqrt{n_d}}. \tag{2.18}$$

$$\epsilon_r\left[\left|\hat{G}_{12}(f)\right|\right] = \frac{1}{|\gamma(f)_{12}|\sqrt{n_d}}. \tag{2.19}$$

$$\epsilon_r\left[\left|\hat{H}_{12}(f)\right|\right] = \frac{\left[1-\gamma_{12}^2(f)\right]^{1/2}}{|\gamma_{12}(f)|\sqrt{2n_d}}. \tag{2.20}$$

For the system described it is a assumed that $Y_1(t)$ and $Y_2(t)$ can come from an unmeasured common source $X(t)$ via unknown linear transformation. So long as the extraneous output noise is small compared to the signal terms a high value of γ_{12}^2 can be expected.

2.5.1 Estimated error in measurements

In order to gain further insight into the sensitivity of a certain parameter to experimental error for a given set-up the system under investigation is modeled using the linear acoustic theory described in section 1.3 to provide theoretical transfer functions. A known error can then be induced on the transfer functions, or the Mach number, and the consequential error in the quantities of interest be calculated.

Figure 2.11 is a plot of the estimated error in the measured value of $|R|$ for a given percentage error in the magnitude of the transfer function as a function of frequency. It is apparent from the plot that the error sensitivity of $|R|$ for an error in the measured transfer function is a function of frequency. It can also be observed that the error sensitivity passes through zero at values of $ka \approx 0.16, 0.37\&0.53$. This is because this particular error is a function of the relative difference in $\hat{p}_1$ and

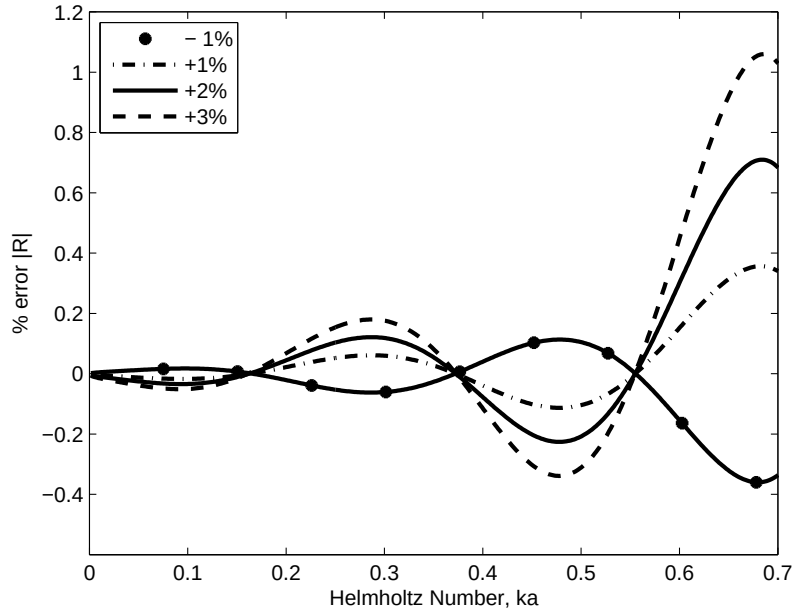

FIGURE 2.11: Estimated error in measurement of $|R|$ for a given percentage error in transfer function.

$\hat{p}_2$ which tends toward zero at these Helmholtz number. This is not to say that the total error is zero at these frequency but rather just the error associated bias in the transfer function. The effects of other errors, such as that associated with the mean flow Mach number, have been assessed individually. With a knowledge of these sensitivities a more insightful examination of the experimental results can be undertaken. Further details of such error sensitivities are provided in Appendix A.2.

2.6 Attenuation of sound at low frequencies in a simple duct with flow

In this section a measurement method for the viscothermal attenuation coefficient in a cylindrical duct in the direction of and against flow is presented. The values of $\alpha^{\pm}$ determined using the method are compared with those predicted using Howe's expression as defined below.

$$\alpha^{\pm} = \frac{\sqrt{2\omega}}{cD_p(1 \pm M)} \quad Re\left[\sqrt{2}e^{\frac{-j\pi}{4}}\left(\frac{\nu}{(1\pm M)^2}\right)\right] \quad \times F_A\left[\sqrt{\frac{j\omega\nu}{\kappa_k^2 u_*^2}}, \delta_\nu\sqrt{\frac{j\omega}{\nu}}\right] \quad (2.21)$$
$$+\frac{\beta c^2\sqrt{\chi}}{C_p} \quad \times F_A\left(\xi^2\sqrt{\frac{j\omega\chi}{\kappa_k^2 u_*^2}}, \delta_\nu\sqrt{\frac{j\omega}{\chi}}\right)$$

where

$$F_A(a,b) = \frac{j(H_1^1(a)cos(b) - H_0^1(a)(b))}{H_0^1(a)cos(b) + H_1^1(a)sin(b)} \quad (2.22)$$

$\chi = k_{th}/\rho C_p$, $\kappa_K \approx 0.41$, $\beta = 1/T$ and $D_p = 4A/l_p$ is the hydraulic diameter of the duct. H_j is the Hankel function of order J and u_* is the friction velocity. A method for determining the friction velocity required to satisfy eqn 2.22 is presented in Appendix A.5. The measurements for the viscothermal attenuation coefficient in a cylindrical duct in the direction of and against flow are included and discussed.

2.6.1 Measurement method

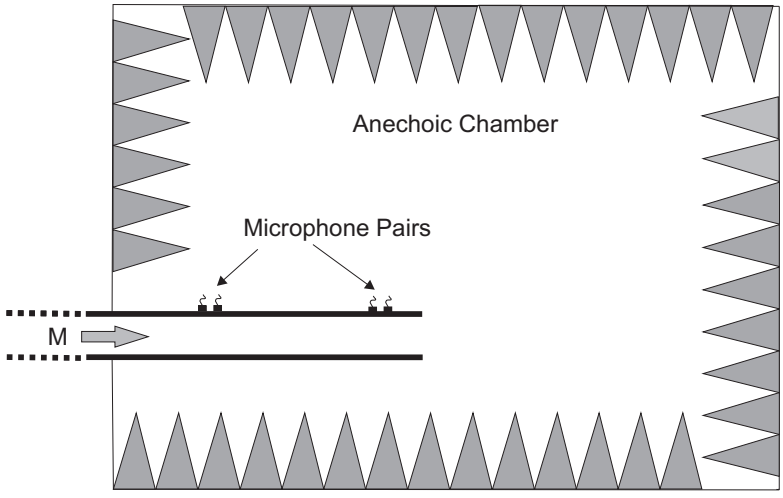

FIGURE 2.12: Experimental set-up for a simple pipe with two pairs of microphones flush with the duct wall

Figure 2.12 is a schematic of the experimental setup. All measurements were carried out using extruded Perspex tube, with a 40mm internal diameter and 4mm wall thickness. Four microphones are fitted flush with the inner wall of the duct

at locations x_1, x_2, x_3 and x_4, equivalent to 160mm, 235mm, 755mm and 830mm upstream from the duct termination respectively. Simultaneous pressure time histories were acquired from the microphones under flow and no flow conditions with and without acoustic excitation. A duct Mach number range of 0-0.14 is investigated. Excitation was via a loudspeaker upstream. A slow-sine sweep/selective averaging technique was implemented to provide a much improved signal to noise ratio to that of broadband excitation when flow was used. A sampling rate of 20kHz is used for all measurements. The air temperature was measured at 780mm upstream.

2.6.1.1 Determination of α with no flow

According to linear acoustic theory

$$\hat{p}_1^+ = \hat{p}_3^+ e^{-j\hat{k}\Delta_{13}}, \tag{2.23}$$

where Δ_{13} is the distance between microphone 1 & 3. Letting

$$\left|\frac{\hat{p}_1^+}{\hat{p}_3^+}\right| e^{j\phi} = e^{-j(k+\alpha)\Delta_{13}} e^{-\alpha\Delta_{13}}, \tag{2.24}$$

and equating the imaginary parts of phase yields

$$\alpha = -(k + \frac{\phi}{\Delta_{13}}). \tag{2.25}$$

Similarly equating real parts yields

$$\left|\frac{\hat{p}_1^+}{\hat{p}_3^+}\right| = e^{-\alpha\Delta_{13}} \tag{2.26}$$

providing

$$\alpha = \frac{ln\left|\frac{\hat{p}_1^+}{\hat{p}_2^+}\right|}{\Delta_{13}} \tag{2.27}$$

This process can be repeated for using $\hat{p}_1^-$ and $\hat{p}_3^-$. This will allow a total of four values of α to be determined which can be averaged. The fact that a theoretical value of α_k was used to calculate the pressure wave components is irrelevant so long as the microphone spacing for each microphone pair is the same, the error (if any) is eradicated when $\hat{p}_1^+$ is divided by $\hat{p}_3^-$.

2.6.1.2 Determination of $\alpha^{\pm}$

Due to this relatively recent development in the definition of the propagation constants there are a limited amount of published measurements of the viscothermal attenuation coefficient with flow, $\alpha^{\pm}$, employing Dokumaci's formulation. Most recently Allam and Abom[21] experimentally determine $\alpha^{\pm}$ via Dokumaci's formulation using a multi-microphone technique and a nonlinear regression solver. What is presented next is an alternative novel technique which directly determines the viscothermal attenuation coefficient in the direction of, α^{+}, and against, α^{-}, the flow from measurements of the pressure wave components $\hat{p}^{+}$ and $\hat{p}^{-}$ at two distinct positions in a duct. The method requires two pairs of microphones mounted flush with the duct wall. All microphones must be phase and amplitude matched.

Consider the forward propagating wave number $\hat{k}^{+}$

$$\hat{k}^{+} = k\hat{K}_{o}^{+}. \tag{2.28}$$

Substituting equations 1.7 & 1.5 into equation 2.28 and expanding provides

$$\hat{k}^{+} = k\hat{K}^{+} = \frac{k\left(\omega c + \alpha^{+}c^{2}(1-j)\right)}{\left(\omega c + \omega\bar{U} + \alpha^{+}\bar{U}c\right) - \alpha^{+}\bar{U}cj}, \tag{2.29}$$

where α^{+} is the viscothermal attenuation in the direction of the flow. Multiplying the top and bottom of equation 2.29 by $\left(\omega c + \omega\bar{U} + \alpha^{+}\bar{U}c\right) + \alpha^{+}\bar{U}cj$ yields

$$\hat{k}^{+} = \frac{k\left(\omega c + \alpha^{+}c^{2}(1-j)\right)\left(\omega c + \omega\bar{U} + \alpha^{+}\bar{U}c + \alpha^{+}\bar{U}cj\right)}{\left(\omega c + \omega\bar{U} + \alpha^{+}\bar{U}c\right)^{2} + (\alpha^{+}\bar{U}c)^{2}}. \tag{2.30}$$

Expanding $\left(\omega c + \omega\bar{U} + \alpha^{+}\bar{U}c\right)^{2} + (\alpha^{+}\bar{U}c)^{2}$ yields

$$\left(2\bar{U}^{2}c^{2}\right)\alpha^{+^{2}} + \left(2\omega\bar{U}c^{2} + 2\omega\bar{U}^{2}c\right)\alpha^{+} + \left(\omega^{2}c^{2} + 2\omega^{2}\bar{U}c + \omega^{2}\bar{U}^{2}\right). \tag{2.31}$$

Using the substitutions $d = \left(2\bar{U}^{2}c^{2}\right)$, $e = \left(2\omega\bar{U}c^{2} + 2\omega\bar{U}^{2}c\right)$ and $f = \left(\omega^{2}c^{2} + 2\omega^{2}\bar{U}c + \omega^{2}\bar{U}^{2}\right)$ provides the result

$$\left(\omega c + \omega\bar{U} + \alpha^{+}\bar{U}c\right)^{2} + (\alpha^{+}\bar{U}c)^{2} = d\alpha^{+^{2}} + e\alpha^{+} + f. \tag{2.32}$$

Expanding $k\left(\omega c+\alpha^{+}c^{2}(1-j)\right)\left(\omega c+\omega\bar{U}+\alpha^{+}\bar{U}c+\alpha^{+}\bar{U}cj\right)$ yields

$$k\left(\left(2\bar{U}c^{3}\right)\alpha^{+^{2}}+\left(\omega c^{3}+\omega\bar{U}c^{2}\right)\alpha^{+^{2}}+\left(\omega^{2}c^{2}+\omega^{2}\bar{U}c+\omega\bar{U}c^{2}\right)-\left(2\bar{U}c^{3}\right)\alpha^{+^{2}}\right). \tag{2.33}$$

Using the substitutions $L=\left(2\bar{U}c^{3}\right)$,$M=\left(\omega c^{3}+\omega\bar{U}c^{2}\right)$,$N=\left(\omega^{2}c^{2}+\omega^{2}\bar{U}c+\omega\bar{U}c^{2}\right)$, and $T=\left(2\bar{U}c^{3}\right)$ gives

$$k\left(\omega c+\alpha^{+}c^{2}(1-j)\right)\left(\omega c+\omega\bar{U}+\alpha^{+}\bar{U}c+\alpha^{+}\bar{U}cj\right)=k\left(L\alpha^{+^{2}}+M\alpha^{+}N+T\alpha j\right). \tag{2.34}$$

hence

$$\hat{k}^{+}=\frac{k\left(L\alpha^{+^{2}}+M\alpha^{+}N+T\alpha j\right)}{d\alpha^{+^{2}}+e\alpha^{+}+f}. \tag{2.35}$$

In the presence of flow

$$\hat{p}_{1}^{+}=\hat{p}_{3}^{+}e^{-j\hat{k}^{+}\Delta_{13}}. \tag{2.36}$$

Letting

$$\left|\frac{\hat{p}_{1}^{+}}{\hat{p}_{3}^{+}}\right|e^{j\phi}=e^{-j\hat{k}^{+}\Delta_{13}} \tag{2.37}$$

and equating the magnitude either side of equation (2.37) provides the equation

$$Qd\alpha^{+^{2}}+(Qe-kT)\alpha^{+}+Qf=0. \tag{2.38}$$

where $Q=(ln\frac{p_{1}^{+}}{p_{3}^{+}})/\Delta_{13}$. Similarly equating the phase yields

$$(d\phi+kL\Delta_{13})\alpha^{+^{2}}+(\phi e+kM\Delta_{13})\alpha^{+}+(\phi f+kN\Delta_{13})=0 \tag{2.39}$$

The roots of equation 2.38 and 2.39 can then be determined providing an estimate of α^{+}. This process can be repeated using $\hat{p}_{1}^{-}$ and $\hat{p}_{3}^{-}$ and K_{o}^{-} to determine the attenuation coefficient, α^{-}, against the flow direction. Unfortunately the author did was unable to simplify the roots into a convenient expression despite the use of the mathematics software *Mathematica*. It should be noted that only one of the roots provides a realistic value for $\alpha^{\pm}$ with the other providing an unrealistic value several orders of magnitude higher than the theoretical value provided by Kirchoff [10]. It is unclear to the author whether these 'unrealistic roots' have any physical meaning however they are ignored in the current analysis.

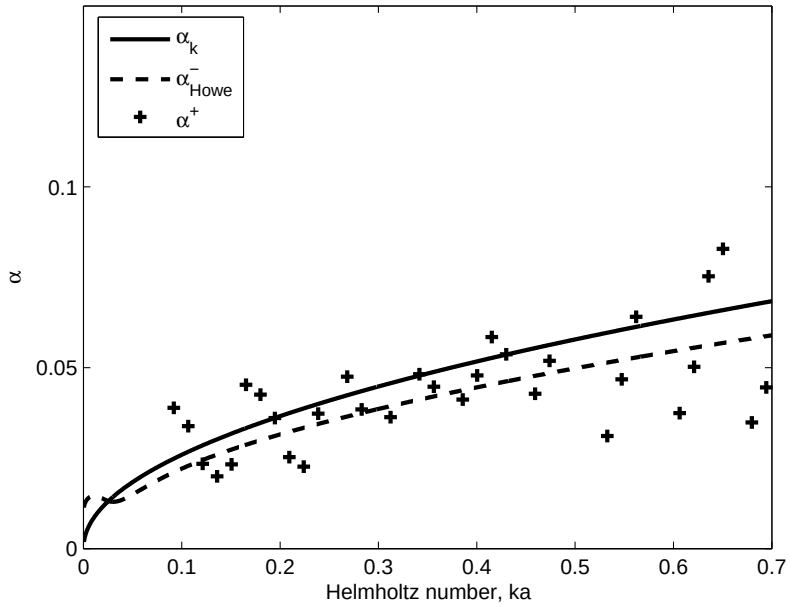

FIGURE 2.13: Measured value of α^+ compared to that predicted by Howe for a mean flow Mach number of 0.052 as a function of ka for $a = 0.02$. Results indicate degree of scatter in the measurements when there is flow.

2.6.2 Results

This section presents the results for the viscothermal attenuation coefficients measured in a cylindrical duct with and without mean flow. The results where determined using a sinusoidal excitation over the range 20-2000Hz. The results using this method alone provide attenuation coefficient spectra with a lot of scatter. This can be observed in figure 2.13 which shows the measured value of α^+ for a mean flow Mach number of 0.052. To improve on this only results with a coherence between microphones 1&2 and microphones 3&4 exceeding 0.999 were adopted. Assuming that $\alpha^{\pm}$ is a smooth function of ka as suggested in figure 1.2 the average of these values measured between frequency bands of 250Hz were calculated.

Figure 2.14 is a plot of the viscothermal attenuation coefficient, α, compared with that predicted by Kirchoff's expression. Initial observations of the measured values indicate α to be a smooth function of ka with slight modulation in amplitude at $ka = 0.092$ and $ka = 0.46$. Examination of the error sensitivity of α, as shown in Figure A.3, suggests that this is attributed to higher error sensitivity of the technique at these frequencies. Further to this, assuming that α should exhibit a smooth spectral trend such as that of α_k, any modulation or scatter in the

results allows for the error in the transfer functions to be estimated. Comparison of the data with the predicted error plotted in Figure A.3 suggest the error in the measured transfer functions is less than 1%. Excluding the value at $ka = 0.092$, which is lower than the prediction of Kirchoff by 31.12%, there is a general increase in the magnitude of α_o from -9.9% to 21.96% of α_k with increasing ka. In comparison to this measurements by Peters et al[20] determined α_o to be within 2% of α_k. However, Peter's measurements are within the range $0.02 < ka < 0.05$ and this reinforces the result at $ka = 0.184$ which is within 1.3% α_k. Other measurements by Dalmont[72] taken in a closed ended duct are also within $\pm 2\%$ of α_k. Such results stengthen the validity of Kirchoff's expression, it is therefore assumed that the variance of the data acquired is an indication of the error limits of the experiment rather than being associated real effects. Figures 2.15 - 2.20 show plots of the viscothermal attenuation coefficient measured in the direction of the mean flow and contra to the flow direction for mean outflow Mach numbers of 0.052, 0.096, and 0.14. On each graph, each set of experimental data is compared with the respective prediction provided by Howe's expression for $\alpha\pm$, as well as Kirchoff's expression of the no flow case.

It is apparent from the plots that Howe's expression predicts a general increase in α^-_{Howe} with increasing mean duct outflow Mach number, compared to a general decrease in α^+_{Howe} under the same conditions. Additionally, it is apparent that there is a modulation in the spectral trend in both α^-_{Howe} & α^+_{Howe} at low Helmholtz numbers. The range of ka over which this occurs increases with increasing flow velocity.

Examination of the experimental data plotted in Figures 2.15, 2.16 & 2.17 suggest that α^- does tend to increase with increasing flow velocity as predicted by eqn 2.22. The relative difference in magnitude of the measured values with those predicted by Howe's expression are within -16.1% and +2.5% for M=0.052, -11.6% and +3.8% for M=0.096, increasing to between -23% and 25.27% for M=0.14. This level of variance of α_- with that of α^-_{Howe} is associated with the error limits of the experiment as previously concluded. The increase in the variance noticeable for M=0.14 is assumed to be related to the increase in error sensitivity with increasing Mach number as indicated in Figure A.4.

Similarly, inspection of Figures 2.18, 2.19 & 2.20 suggest that α^+ does tend to decrease with increasing Mach number in a similar fashion to that predicted by

α^+_{Howe}. The relative magnitude of α^+ to α^+_{Howe} is between -16.28% and 11.53% for M=0.052, -26.2% and 30.8% for M=0.96, and -38.44% and 22.73% for M=0.14. This high level of variance is yet again attributed to the error in the Mach number. The error sensitivity of α^+ to errors in the measured value of Mach number is displayed in Figure A.5. The distinctive dip at $ka = 0.55$ in Figure A.5 is also apparent in the measured value of α^+ reinforcing this assumption.

Considering the error limits of the results it is deemed not possible to make any conclusion regarding the low ka modulation in the spectra of the attenuation coefficient predicted by Howe's expression. However, the results generally support the prediction of Howe with α^- increasing with increasing mean flow velocity and α^+ decreasing with increasing flow velocity. The results also compare well with recently published results of Allam & Abom [21] which were determined using an alternative experimental technique. This agreement with published theory and experimental results helps validate the measurement technique presented. Finally, it can be concluded that Howe's model of $\alpha^{\pm}$ can be used in conjunction with Dokumaci's formulation of the propagation constants to provide an appropriate description of the complex wave numbers with flow.

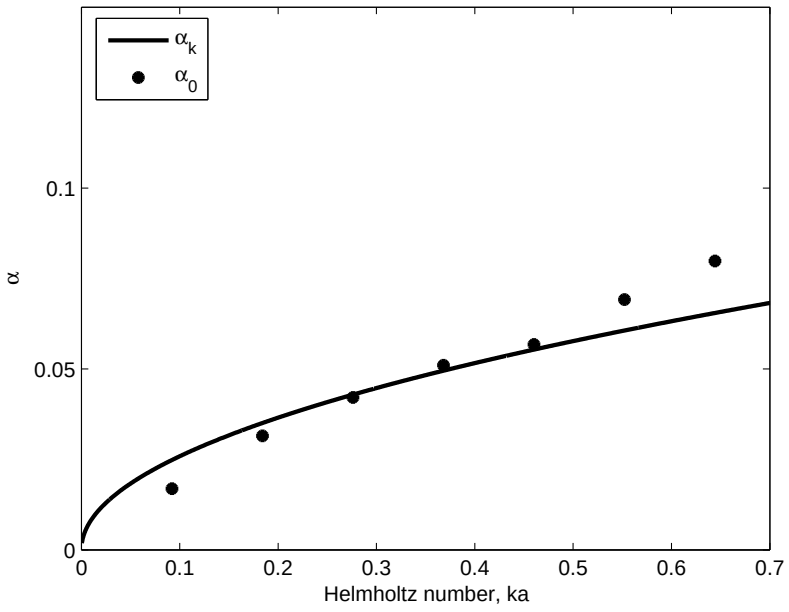

FIGURE 2.14: Measured value of α_0 compared with that predicted by Kirchoff as a function of ka for $a = 0.02$.

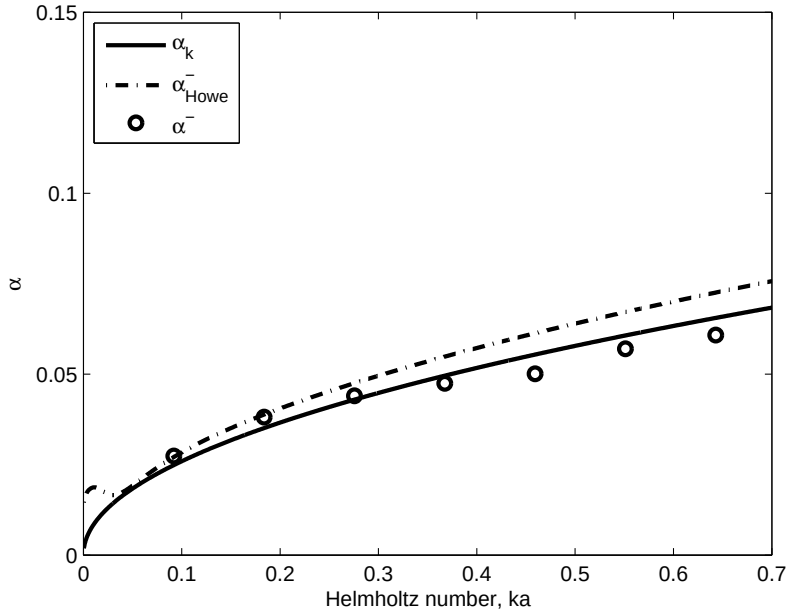

FIGURE 2.15: Measured value of α^- compared to that predicted by Howe for a mean flow Mach number of 0.052 as a function of ka for $a = 0.02$.

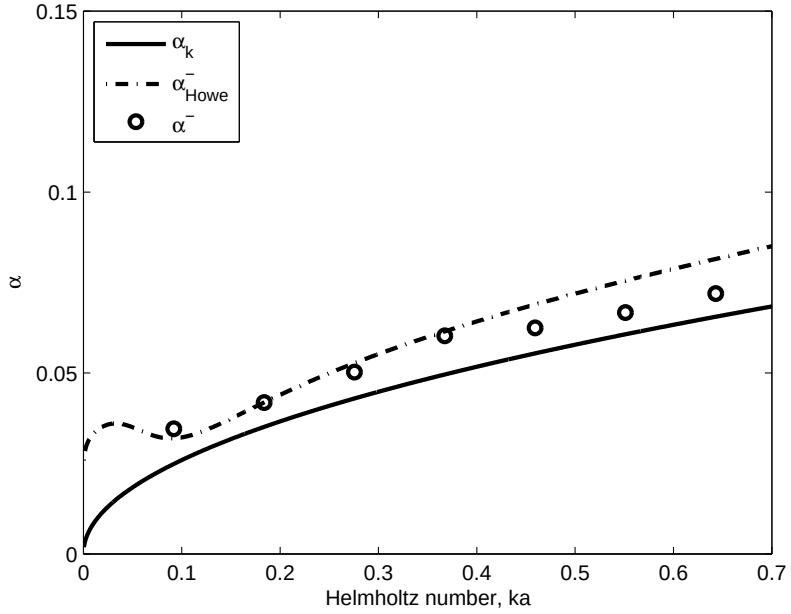

FIGURE 2.16: Measured value of α^- compared to that predicted by Howe for a mean flow Mach number of 0.096 as a function of ka for $a = 0.02$.

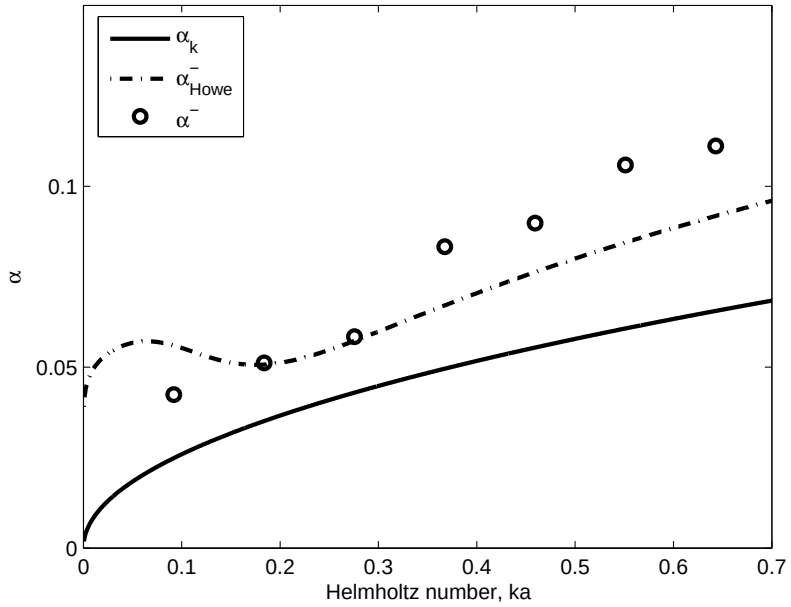

FIGURE 2.17: Measured value of α^- compared to that predicted by Howe for a mean flow Mach number of 0.14 as a function of ka for $a = 0.02$.

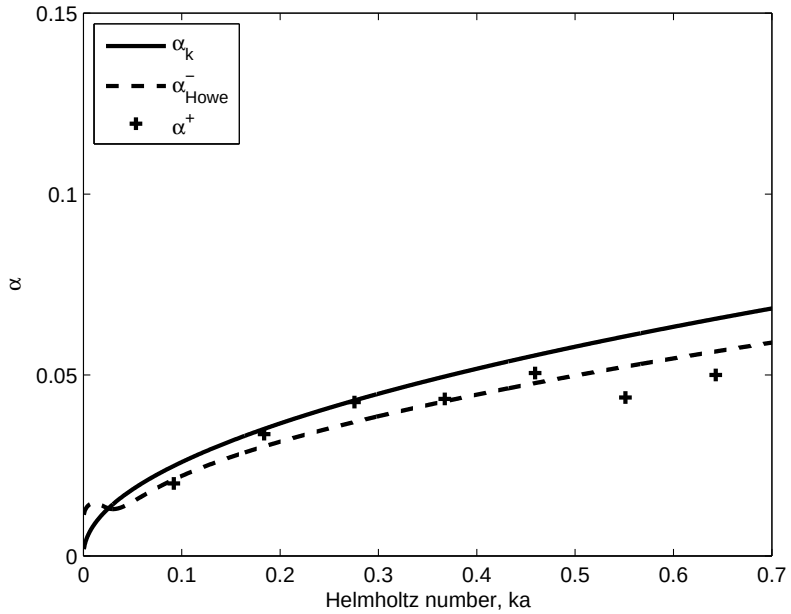

FIGURE 2.18: Measured value of α^+ compared to that predicted by Howe for a mean flow Mach number of 0.052 as a function of ka for $a = 0.02$.

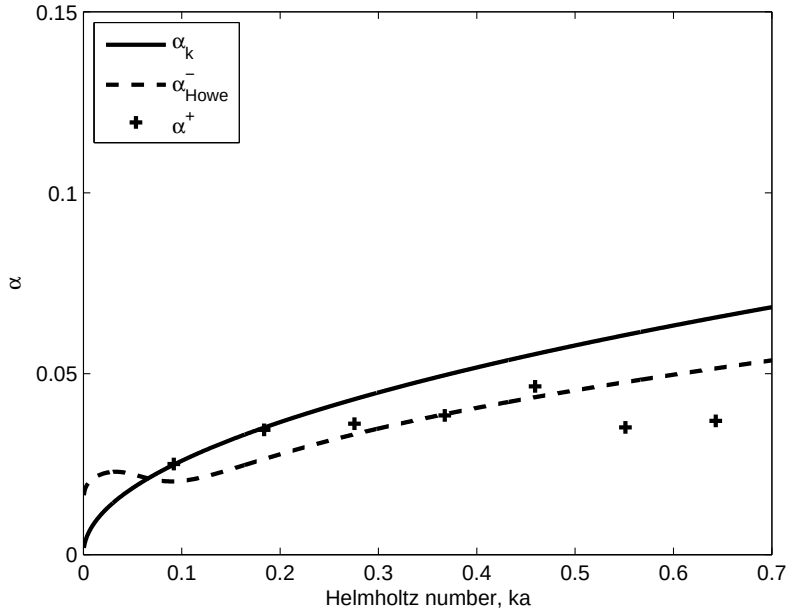

FIGURE 2.19: Measured value of α^+ compared to that predicted by Howe for a mean flow Mach number of 0.096 as a function of ka for $a = 0.02$.

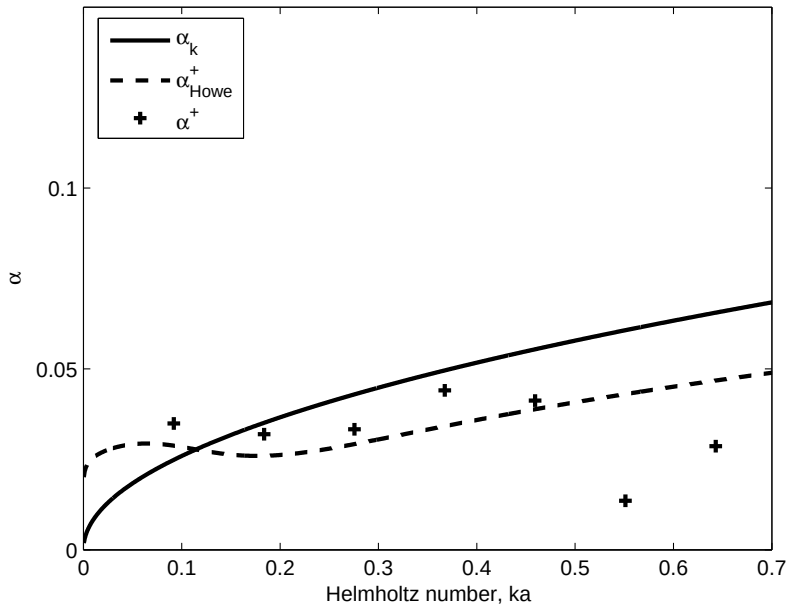

FIGURE 2.20: Measured value of α^+ compared to that predicted by Howe for a mean flow Mach number of 0.14 as a function of ka for $a = 0.02$.

2.7 Pressure Reflection Coefficient

In this section experimental results of the pressure reflection coefficient for an unflanged duct with outflow are compared with those predicted by Munt's solution [3, 4] with a full Kutta condition assumed. In addition, Gabard[1] used similar mathematical techniques to that of Munt and Rienstra[6] to model sound radiation from an annular duct with flow. Using Gabard's Matlab code in conjunction with measured experimental results it is possible to solve for the edge condition parameter, Γ, proposed by Rienstra. This was done by incrementally modifying Γ in the Matlab code until the predicted pressure reflection coefficient converges with that measured. To the author's knowledge, this is the first determination of Γ by using experimental results in conjunction with computational model. The results highlight the importance of the edge condition of the duct termination on the extent of vorticity shed and consequently, the magnitude of the pressure reflection coefficient.

2.7.1 Measurement method

.

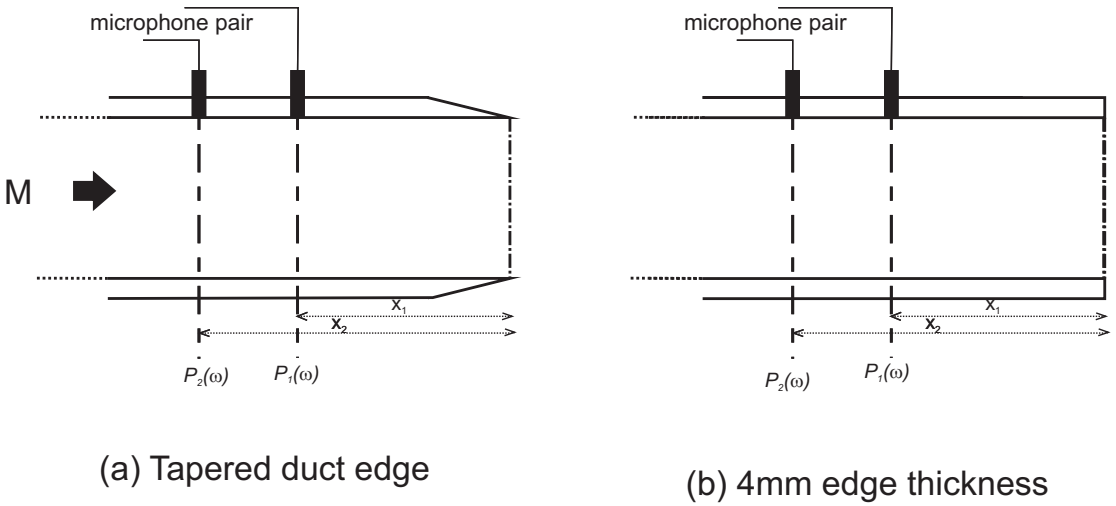

FIGURE 2.21: Duct Termination Types (a) 30° Tapered wall edge, (b) 4mm wall edge thickness.

Figure 2.21 is a schematic of the basic experimental set-up used to determine the reflection coefficient a simple exhaust pipe. The in-duct acoustic pressure was measured simultaneously at x_1 amd x_2 using a microphone pair mounted flush

with the inner wall of the duct. x_1 and x_2 are 120mm and 195mm upstream of the duct termination respectively. All measurements are performed on extruded Perspex tubing, with 40mm internal diameter and 4mm wall thickness, located in an anechoic chamber. The experiment was caried out on two configuration (a) the duct has a 30° tapered edge at the open end to closely represent an infinitely thin duct wall (b) the duct termination has a 4mm edge thickness. The velocity is varied from zero to Mach 0.14. In order to ensure accurate calibration of both the relative magnitude and phase between microphones a sensor switching method discussed in section 2.3.3 is adopted. A slow sine sweep is used when the system is acoustically excited and a selective averaging technique is implemented to provide a much improved signal to noise ratio than that achieved by white noise excitation. The pressure wave components at the duct terminations are calculated using a wave decomposition method discussed in section 2.2, allowing $\hat{R}$ to be calculated.

2.7.2 Results

Figure 2.22 shows the pressure reflection coefficient of an open ended duct with no flow measured for a duct with a tapered edge compared with that predicted by Levine and Schwingers analysis for a semi-infinite duct with an infinitely thin wall thickness. First observations of the comparison highlight the striking similarity between the theoretical prediction and the experimental results. Analysis of the results indicates that the experimental data lies 0.25% lower than the prediction for $0.05 \leq ka \leq 0.45$, with a variance of 0.1% and for $ka < 0.05$ the difference tends toward 0%. The difference increase from 0.25% to 1.5% from $ka = 0.45$ to $ka = 0.7$.

The error analysis of $\left|\hat{R}\right|$ indicates that a modulation in the spectral trend should occur if any error of note should be present in the transfer function measurement, as shown in Figure A.7. Such a modulation is not apparent in the spectra suggesting the any error in the transfer function measurement is much less than 1%. That said, it is apparent that the error sensitivity of the reflection coefficient is highest between $0.5 \leq ka \leq 0.7$ range which may explain the slight increase in difference between Levine and Schwingers prediction and the experiment within this range. In comparison with these results, Peters et al [20] measured the $\left|\hat{R}\right|$ to within 1.1% of Levine and Schwingers prediction over the range $0.03 \leq ka \leq 0.3$ In addition, Allam and Abom [21] measured $\left|\hat{R}\right|$ to within 3% of that predicted for

$0.01 \leq ka \leq 1.25$. Considering the support of previous publication and the close comparison of the current results, Levine and Schwinger's model can be considered accurate to within the precision of the measurement experimental technique implemented. It is also concluded that this result reinforces the reliability of the experimental techniques involved.

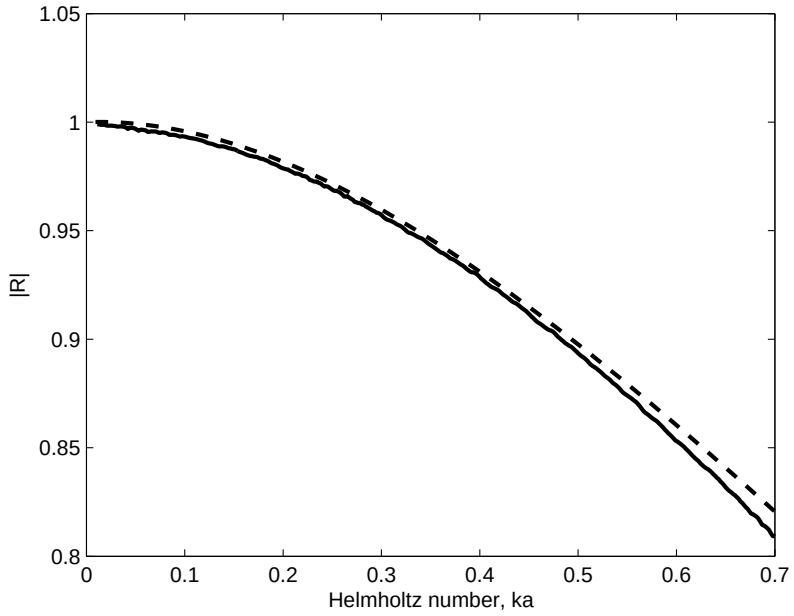

FIGURE 2.22: Pressure reflection coefficient of an open ended duct with no flow: (- -) Levine and Schwinger [2],(-) Tapered edge duct measurement.

Figures 2.23, 2.24 & 2.25 show the pressure reflection coefficients of an open ended duct with outflow Mach numbers of 0.0468, 0.0935 & 0.1426 respectively. Each plot includes the measurements for a duct with a tapered edge, a 4mm wall thickness, and a plot of Munt's theoretical prediction assuming a full Kutta condition. Initial analysis of the results indicated that generally the experimental measurements behave in a similar way to that of Munt's prediction with the peak magnitude pressure reflection increasing with increasing Mach number, and the value of Helmholtz number at which this peak occurs also increasing with Mach number. However, further assessment highlights some important differences. Firstly the peak value of the measured results for both the tapered duct wall and the 4mm wall, occurs at a Helmholtz number approximately 27%, 20% and 16% higher than the Munt's predicted value for repective Mach numbers of 0.0468, 0.0935 & 0.1426. Second to this, the peak magnitude of the measured reflection coefficient exceeds

that predicted by Munt by a maximum of 2.9%, 4.9% and 6.7% for a tapered duct and 4.8%, 7.2% & 8.3% for a 4mm edge thickness, with increasing Mach numbers.

The results raise the questions of what is different between Munt's solution and the experimental results, and why is there difference between the results of a tapered duct wall and a 4mm wall edge thickness when there is flow considering they effectively match with no flow? On this basis, we turn to the validity of the full Kutta condition assumption employed by Munt. By assuming that the difference in the measured and predicted results are as a consequence of the extent of vorticity shed, the value of the function Γ can be calculated via comparision of the measured $\hat{R}$ and that predicted for different values of Γ. Figures 2.26 & 2.27 plot the results of such a comparison as a function of $\frac{\omega\delta_{ac}}{U}$, with δ_{ac} is the acoustic boundary layer thickness defined as $\sqrt{\frac{2u_*^2}{\nu\omega}}$. The results indicate that the full Kutta condition ($\Gamma = 1$) is not valid for all frequencies and flow rates. Rather, the full Kutta condition is only valid when $\frac{\omega\delta_{ac}}{U} \rightarrow 0$. As the frequency and flow rate increase the value of Γ tends to decrease, until after the peak value of $\hat{R}$ has been reached, at which point it begins to increase toward the full Kutta condition once more. This turning point seems to lie between $1 \times 10^3 \leq \frac{\omega\delta_{ac}}{U} \leq 2 \times 10^3$. Further to this, examination of the results indicate that Γ is generally higher for a tapered edge than for a 4mm wall thickness with a peak difference between the edge conditions of 76.2%, 57.6% and 50.7 % occuring at the minimum value of Γ for increasing jet Mach numbers. In addition, the extent of vorticity shed generally increases with increasing flow velocity.

From the analysis it can be concluded edge condition plays an important role in the extent of vorticity shed. Significantly, the extent of vorticity shed from the duct edge has an effect on the magnitude of the pressure reflection coefficient. In addition, as we discussed in chapter 1 the vorticity can be an important parameter in the generation and absorption of sound. Importantly from an engineering point of view, selecting an appropriate edge condition can be significant factor if sound absorption or generation is a concern or if the amount of acoustic reflection at a pipe discontinuity with flow is a consideration.

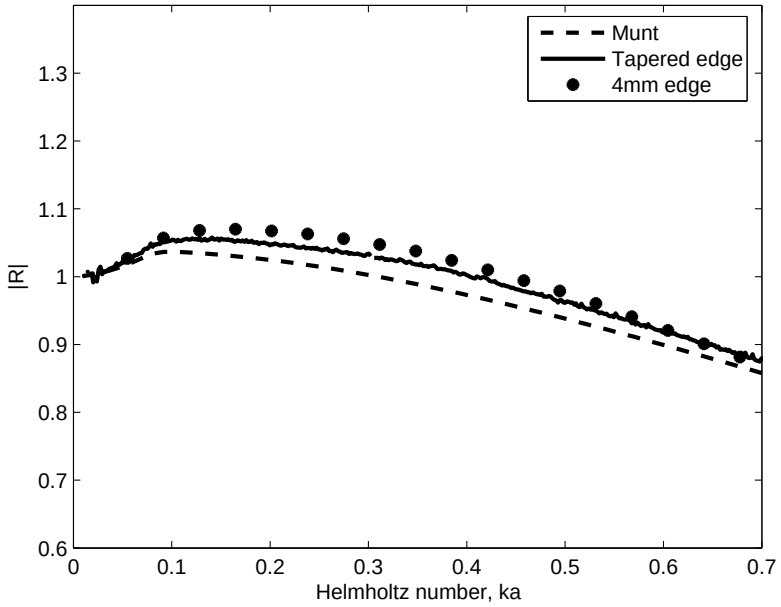

FIGURE 2.23: Pressure reflection coefficient of an open ended duct with outflow Mach number 0.0468: (- -) Munt [3],(-) Tapered edge duct measurement, M=0.0468, (*) 4mm edge measurement, M=0.0525.

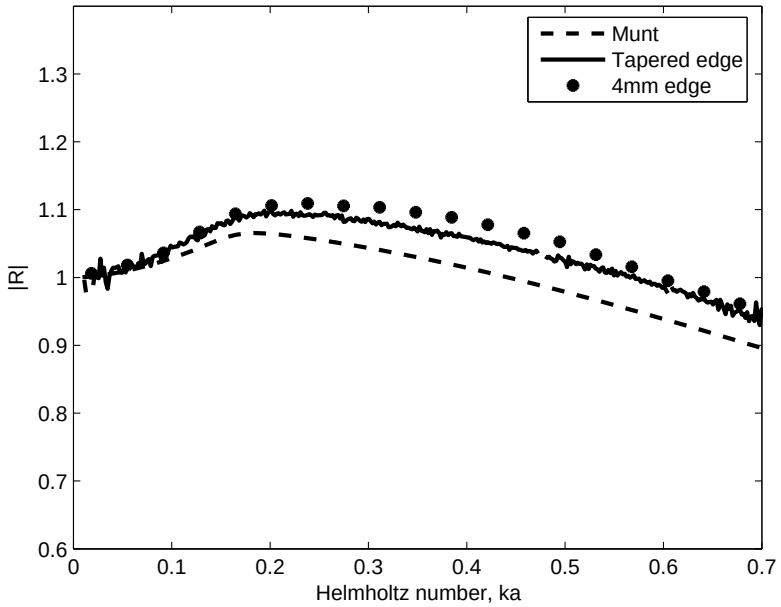

FIGURE 2.24: Pressure reflection coefficient of an open ended duct with outflow Mach number 0.0935: (- -) Munt [3],(-) Tapered edge duct measurement, M=0.0935, (*) 4mm edge measurement, M =0.0963.

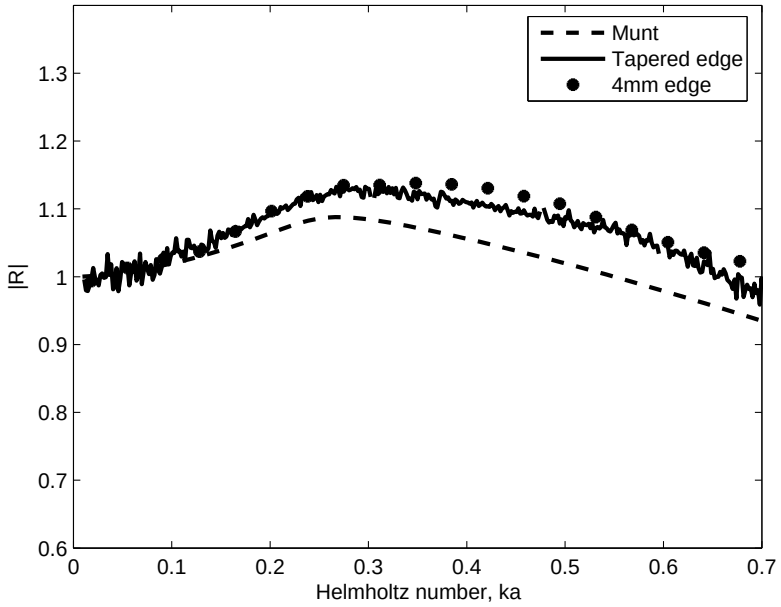

FIGURE 2.25: Pressure reflection coefficient of an open ended duct with outflow Mach number 0.1426: (- -) Munt [3],(-) Tapered edge duct measurement, M=0.1426 (*) 4mm edge measurement, M=0.1411.

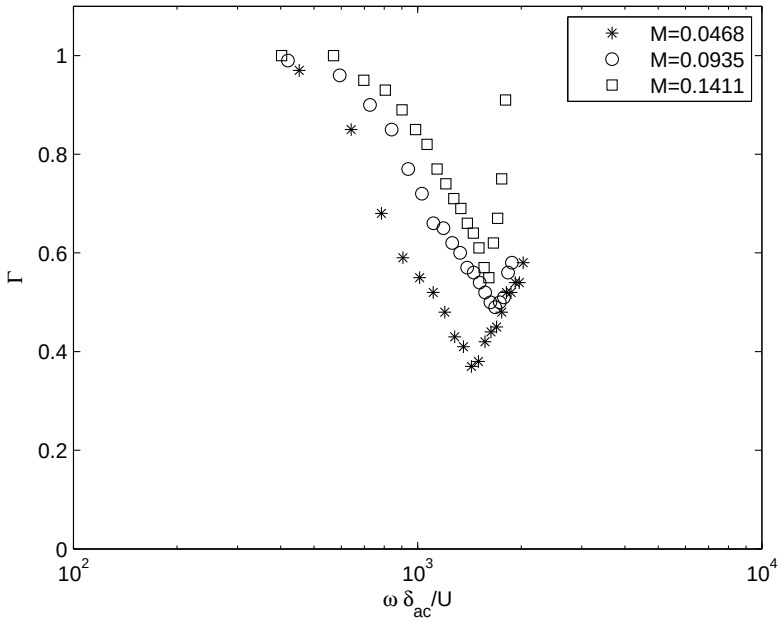

FIGURE 2.26: Extent of vorticity shed, Γ, from an open ended duct with a tapered wall edge as a function of Strouhal number.

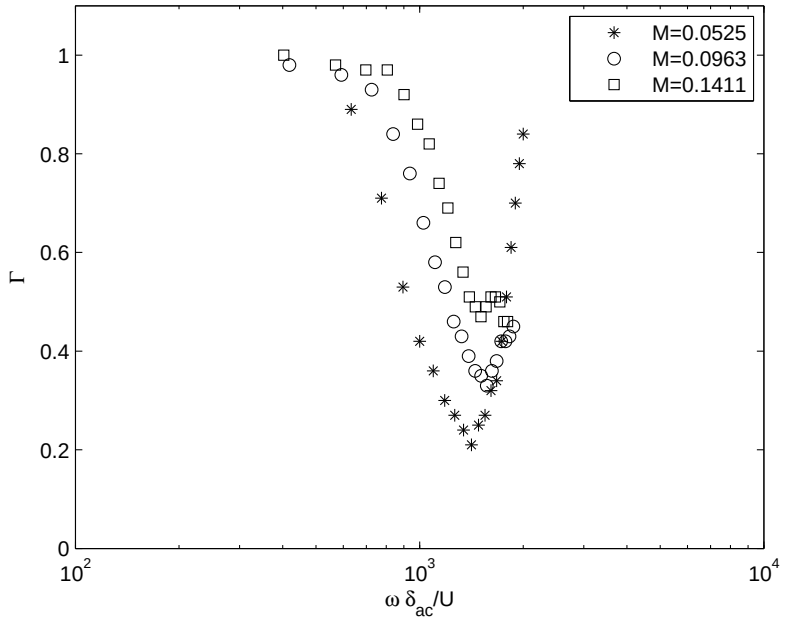

FIGURE 2.27: Extent of vorticity shed, Γ, from an open ended duct with a 4mm duct edge as a function of Strouhal number.

2.7.2.1 Energy reflection coefficient

To gain more insight of the effect of the duct termination on the acoustics of the system it is often useful to plot the energy reflection coefficient, R_E. Peters et al[20] define the energy reflection coefficient as

$$R_E = \left|\hat{R}\right|^2 \left(\frac{1-M}{1+M}\right)^2 \tag{2.40}$$

Figure 2.28 shows a plot of the energy reflection coefficient, as a function ka for a duct with a tapered wall edge. It is apparent from the plot that there that there is a general decrease in the magnitude of the R_E with increasing Mach number. The magnitude of R_E remains below unity over the range of Helmholtz and Mach numbers presented. The results indicate that less acoustic energy is reflected as the flow velocity is increased. This would suggest that an increase in the amount of acoustic power radiated from the duct termination with increasing flow velocity. However, as shall be shown in chapter 3 this is not necessarily the case.

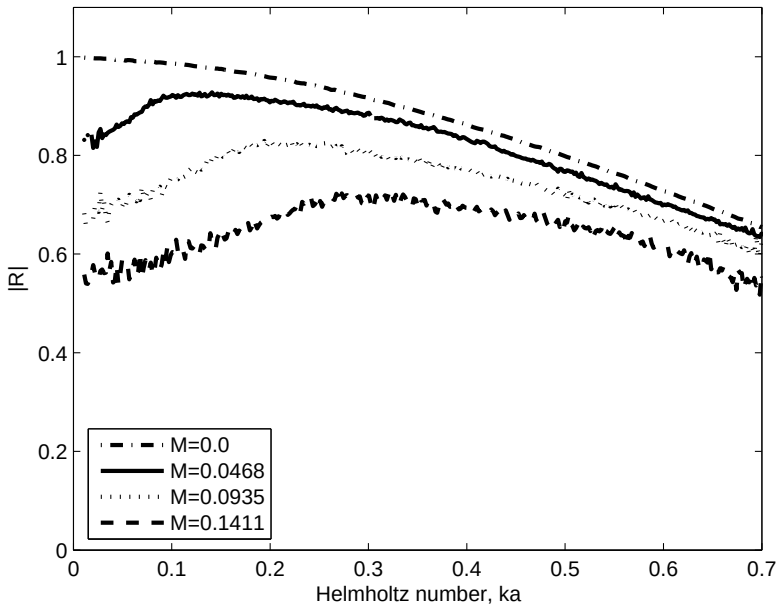

FIGURE 2.28: Energy reflection coefficient, R_E, as a function of Helmholtz number, ka, for a duct with a tapered wall edge and mean outflow.

2.8 Acoustic End Correction

This section details new broadband measurements of the end correction for two different duct edge condition (i) a/b Tapered duct wall & (ii) a/b=0.83 a Mach number range of $0 \leq M \leq 0.15$. The results are compared with the prediction of Levine and Schwinger [2] and Dalmont et al [26] for the two different edge condition with no flow. In addition the results with mean outflow are compared with the prediction of Reinstra[5]

2.8.1 Measurement Method

The pressure reflection coefficient at the duct termination can be estimated using the method described in section 2.7.1. If the pressure reflection coefficient of the open end, $\hat{R}(0)$, is found experimentally the end correction may be estimated as follows.

Consider the reflection coefficient with respect to the location of the end correction, δ,

$$\hat{R}(\delta) = \frac{\hat{p}^-(\delta)}{\hat{p}^+(\delta)}. \tag{2.41}$$

The end correction is assumed to extend beyond the physical end of the pipe to a plane at which the phase of the reflection coefficient is zero, hence,

$$\hat{R}(\delta) = \frac{\hat{p}^-(0)e^{j\hat{k}^-\delta}}{\hat{p}^+(0)e^{-j\hat{k}^+\delta}} = \hat{R}(0)e^{j(\hat{k}^-+\hat{k}^+)\delta}. \tag{2.42}$$

Letting the measured reflection coefficient $\hat{R}(0) = \left|\hat{R}(0)\right| e^{j\theta}$ and the reflection coefficient at the end correction be $\hat{R}(\delta) = \left|\hat{R}(\delta)\right| e^{j\pi}$ then

$$\left|\hat{R}(\delta)\right| e^{j\pi} = \left|\hat{R}(0)\right| e^{j\theta} e^{j(\hat{k}^-+\hat{k}^+)\delta}. \tag{2.43}$$

Separating the phase into real and imaginary part gives

$$\left|\hat{R}(\delta)\right| e^{j\pi} = \left|\hat{R}(0)\right| e^{j\theta} e^{-Im(\hat{k}^- + \hat{k}^+)\delta} e^{jRe(\hat{k}^- + \hat{k}^+)\delta}. \tag{2.44}$$

Equating the the imaginary part of phase and rearranging provides

$$\delta = \frac{\pi - \theta}{Re(\hat{k}^- + \hat{k}^+)}. \tag{2.45}$$

2.8.2 Results

Figure 2.29 plots the measured acoustic end correction of an open ended duct with $a/b = 1$ and $a/b = 0.833$ with no flow compared with that predicted by Levine and Schwinger. Examination of the results indicates that the end correction for a duct termination with sharp edge does not match that predicted by Levine and Schwinger, rather it varies between 3% and 9.5% higher. The error analysis detailed in Figure A.8 suggest the modulation in the amplitude of δ, apparent in figure 2.29 is a result of error in the transfer function, however, the extent of this modulation indicates the percentage error in the transfer function is less than 1%. It is also apparent from Figure A.8 that the error in the measured end correction tends toward a mimimum at $ka = 0.3$, 0.475 & 0.62. Assessing the results at these frequencies indicates that the end correction for $a/b = 1$ is on average 7% higher than that of Levine and Schwingers prediction and is 3% lower than that measured by Peters [20].

The results for a duct with $a/b = 0.833$ are, as expected, higher than those for a/b=1. Analysis of the results with that predicted using eqn 1.12 indicate the results to be between 0.5% and 7.1% higher than Dalmont et al's [26] prediction for a circular duct with a finite wall thickness. Analysis of the results at $ka = 0.3$, 0.475, & 0.62 indicates the results are on average 5.8% higher than that predicted by eqn 1.12. This difference is mainly due to the assumption by Dalmont et al that the end correction of an unflanged duct has a low frequency limit of $0.6133a$ rather than the $0.65a$ measured. In contrast to this, the experimental results published by Allam [21] suggest the end correction for duct with $a/b = 0.875$ matches to within 1.4% that predicted by Levine and Schwinger for an unflanged duct. However, the measured results for δ along with those published by Peters et al and the prediction by Dalmont et al contradict Allam et al's results!

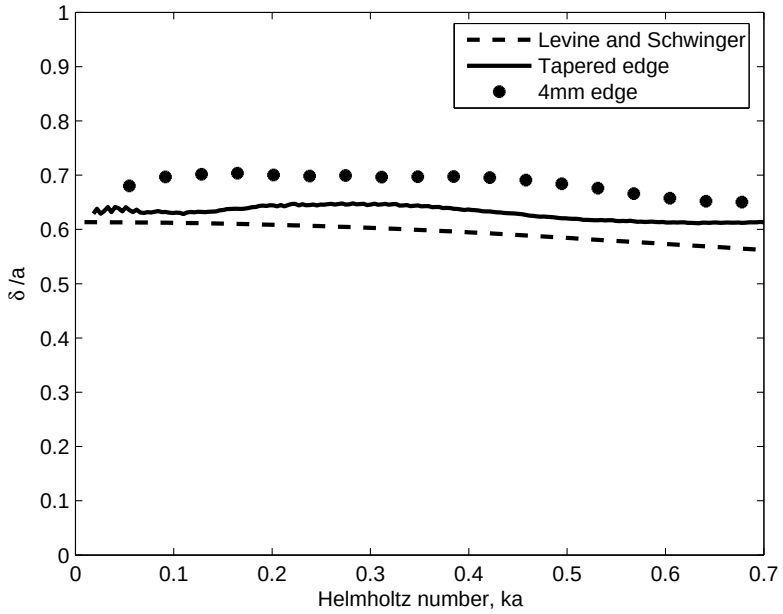

FIGURE 2.29: End Correction of an open ended duct: (- -) Levine and Schwinger [2],(-) Tapered edge duct measurement, (*) 4mm edge measurement.

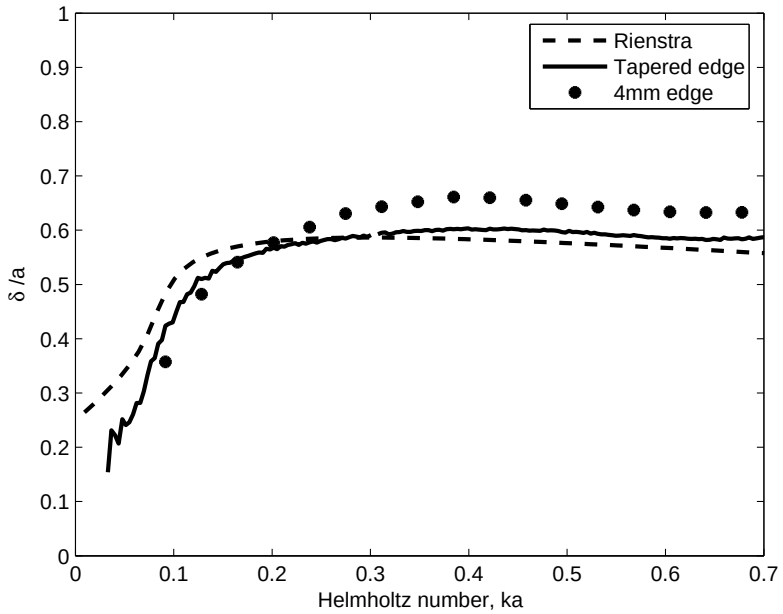

FIGURE 2.30: End Correction of an open ended duct with outflow Mach number 0.0468: (- -) Rienstra [6],(-) Tapered edge duct measurement, M=0.0468, (*) 4mm edge measurement, M=0. 0.0535.

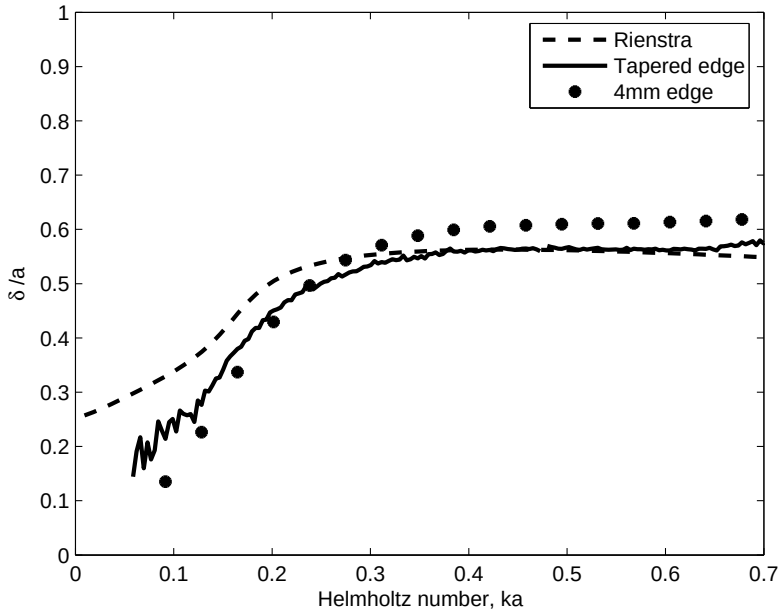

FIGURE 2.31: End Correction of an open ended duct with outflow Mach number 0.0935: (- -) Rienstra [6],(-) Tapered edge duct measurement, M=0.0935, (*) 4mm edge measurement, 0.0963.

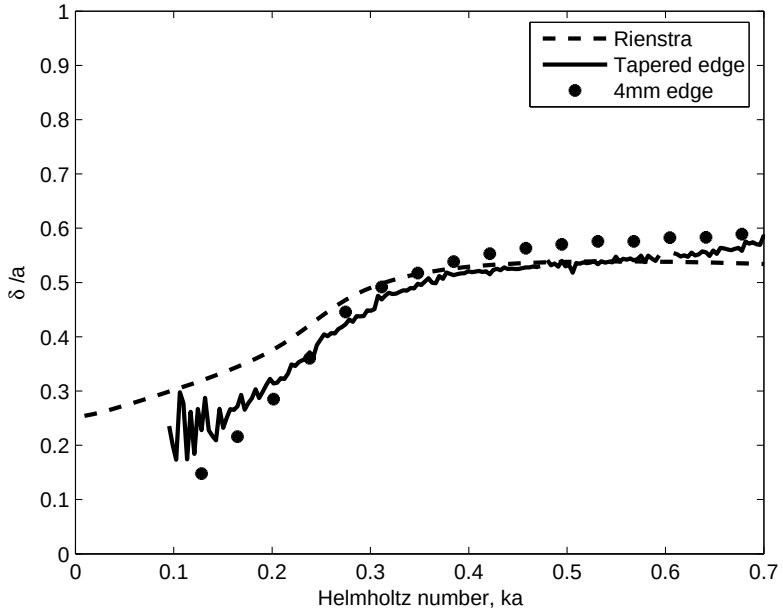

FIGURE 2.32: End Correction of an open ended duct with outflow Mach number 0.1426: (- -) Rienstra [6],(-) Tapered edge duct measurement, M=0.1426, (*) 4mm edge measurement M=0.1411.

Figures 2.30, 2.31 & 2.32 show the end correction measured for a simple unflanged duct of a/b =1 & 0.833 with outflow Mach numbers 0.0468, 0.0935 and 0.1426. The results are compared with those predicted by Rienstra using Gwenael Gabarts code. It is apparent from the plots that the measured results for both edge conditions follows the general trend predicted by Rienstra. However, the results seem to tend toward an average low frequency limit of $0.193a$ and $0.141a$ for $a/b = 1$ and 0.833 respectively. This matches the value determined by Peters et al for an unflanged duct for $a/b = 1$, however they are 27% lower than the $0.19a$ limit determined by Peters et al for $a/b = 0.833$. The reason for this is unclear, as Peters et al's results for ducts with a finite wall thickness also tend toward $\delta = 0.19a$, however Figure A.8 indicates that the sensitivity of δ is high for small errors in the transfer function measured at such low frequencies. The results suggest that Rienstra's low frequency limit of $\delta = 0.2554a$ is approximately 34% to high. This difference is significant when considering the acoustic natural frequencies of ducts of relative short lengths.

Finally, the magnitude of the end correction increases to an average of 5.7% higher than that of Rienstra's prediction for $a/b = 1$ and 11.9% higher for $a/b = 0.833$. This is similar to the corresponding magnitude difference of the results to Levine and Schwingers prediction for δ for an unflanged duct with flow and is attributed to the effect of the duct wall thickness.

2.9 Conclusions

In this chapter the experimental set-up and techniques employed to determine the plane wave pressure wave components in ducts with flow are detailed and discussed. The techniques were implemented to assess the plane wave aeroacoustic characteristics of a simple exhaust pipe with steady subsonic flow, namely, the viscothermal attenuation coefficient, the pressure reflection coefficient and acoustic end correction of an unflanged duct with flow. The following conclusion were made:

- A novel method for the determination of the viscothermal attenuation coefficient at low frequencies in a duct with flow has been presented. The technique was used to determine $\alpha^{\pm}$ for duct Mach numbers of up to 0.1426. The results support the trend predicted by Howe for $\alpha^{\pm}$ to within a variance

of -38.44% to +25.27%. Measurements for α without flow support Kirchoffs prediction. This agreement with published theory and experimental results helps validate the measurement technique presented.

- The good agreement of Howe's prediction for $\alpha^{\pm}$ with the experimental results determined using Dokumaci's formulation of the propagation constants indicates that they provide an appropriate description of the complex wave numbers with flow.

- Measurements of the pressure reflection coefficient with no flow support Levine and Schwingers prediction for an unflanged duct with flow. Results of the pressure reflection coefficient of an unflanged duct with outflow indicate that $\left|\hat{R}_0\right|$ does increase to a value in excess of unity and has a similar spectral trend to that predicted by Munt assuming a full Kutta condition. However, further analysis indicated that the full Kutta condition is only valid in the low frequency limit. Novel results of the extent of vorticity shed from the duct have been determined and found to vary with acoustic Strouhal number and edge thickness. The minimum amount of vorticity shed occurs within the range $1 \times 10^3 \leq \frac{\omega \delta_{ac}}{U} \leq 2 \times 10^3$.

- The end correction of an unflanged duct with flow is found to tend toward a low frequency limit of $0.65a$ rather than the $0.6133a$ predicted by Levine and Schwinger for an unflanged circular duct with flow. As a consequence Dalmonts expression for the end correction of a circular duct with a finite wall thickness is approximately 6% too low.

- The end correction of an unflanged duct with flow is modified by the presence of flow in a similar way to that predicted by Rienstra, however, the low frequency limit seems to tend toward $0.19a$ rather than the $0.2554a$ predicted.

Chapter 3

Acoustic power flux in ducts with flow

3.1 Introduction

This chapter deals with the subject of sound power flux in ducts with flow at frequencies at which the wavelength can be considered substantially planar. A method for determing the sound power flux is presented. The method is first applied to assess the absorption of the sound power through the jet formed at the outlet of a simple unflanged duct with outflow. This involved measuring the acoustic power flux immediately upstream of the duct termination as well as that radiated in the farfield. The sound power flux in simple expansion chambers with flow is assessed with experimental measurements compared with predictions from commercial design software APEX. The results match to within 2dB with no flow supporting the validity of the measurements. However, as flow is increased differences between the measured powerflux and that predicted increase at certain frequencies suggesting the presence of aeroacoustic sources in the chamber.

A method is presented for the measurement of aeroacoustic source strengths in ducts with flow. The source is defined in section 3.5 in terms of acoustic power and is determined by measuring the acoustic power flux both upstream and downstream of the source region in a duct. The method adopts a plane wave approximation and determines the acoustic power flux by calculating the pressure wave components using the wave decomposition technique described in section 2.2. The

method was assessed experimentally by creating a source in a duct at a number of known frequencies and modifying its magnitude by a known amount. This experimental verification is detailed in section 3.6. The results confirm the validity of the technique.

3.2 Determination of acoustic power flux in ducts with flow

Acoustic power, W, has a physical definition as time-averaged acoustic energy crossing a surface, S, per unit time [73]. Mathematically this is defined as

$$W = \int_S I \cdot \mathbf{n} dS, \tag{3.1}$$

where I is the time averaged acoustic intensity vector and $\mathbf{n}$ is the unit normal vector to the surface S.

Davies [9] defines the acoustic intensity in a duct in which acoustic wave propagation is restricted to frequencies below the cut-on of the first higher mode and a plug flow profile exists as

$$I = I^+ - I^- = \frac{1}{\rho c}\left(\left|\hat{p}^+\right|^2 (1+M)^2 - \left|\hat{p}^-\right|^2 (1-M)^2\right) \tag{3.2}$$

Resulting in the acoustic power for such a system being defined as,

$$W = W^+ - W^- = IS. \tag{3.3}$$

Munro and Ingard [74] presented a different technique in which the sound intensity is determined by estimating the acoustic pressure and particle velocity at a plane between two closely spaced microphones using a finite difference approximation. The intensity, I_{fd}, can then be determined by measuring the cross-spectrum and autospectra using

$$
\begin{aligned}
I_{fd} = &-\frac{(1-M^2)(1+3M^2)}{\omega\rho\Delta x}[Im\hat{G}_{12}] \\
&+\frac{M(1+M^2)}{2\rho c}[G_{11}+G_{22}+2Re\hat{G}_{12}] \\
&+\frac{M(1+M^2)}{2\rho c}\frac{([G_{11}-G_{22}]\Delta x^{-1})^2+4(Im\hat{G}_{12}\Delta x^{-1})^2}{G_{11}+G_{22}+2Re\hat{G}_{12}}.
\end{aligned} \tag{3.4}
$$

The intensity measurement which employs eqn 3.2 has advantages over that of eqn 3.4 as it allows for the acoustic intensity propagating upstream and downstream to be determined in addition to the net acoustic intensity. Figure 3.1 plots the ratio of intensity determined using eqn 3.2 to eqn 3.4 for different microphone spacings Δx. It is apparent from the results that the methods diverge with increasing microphone spacing and frequency. This divergence is a result of the linear gradient approximation assumed in the finite difference intensity method [41] becoming less valid as the acoustic wavelength decreases relative to the microphone spacing [75]. Consequently, eqn 3.2 was adopted to calculate the intensity, and hence the power flux, from measured data.

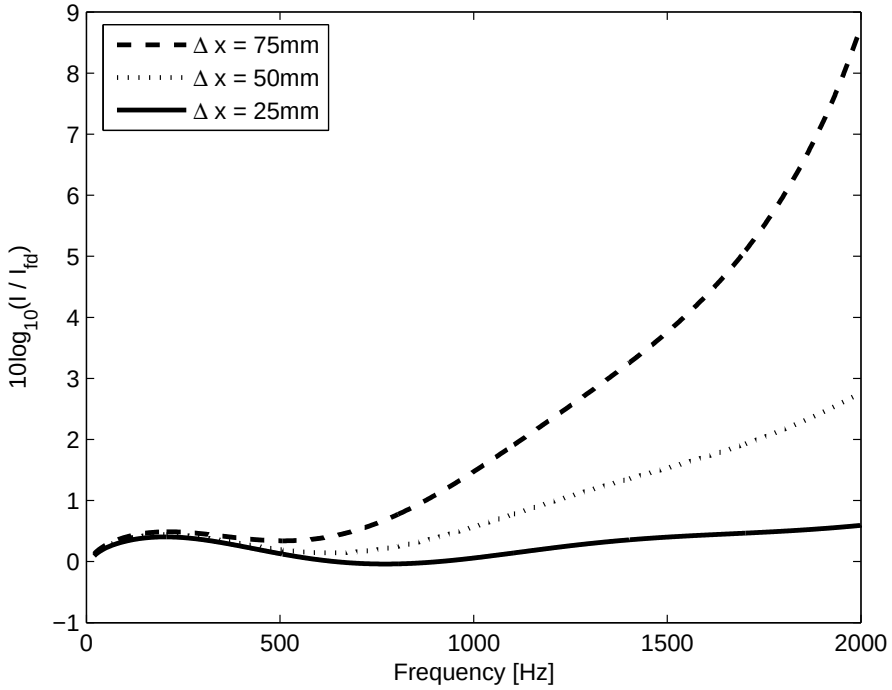

FIGURE 3.1: Ratio of intensity determined using eqn 3.2 to eqn 3.4 for different microphone spacings Δx. Ratio plotted in dB.

3.3 Sound absorption through a jet from an unflanged exhuast pipe

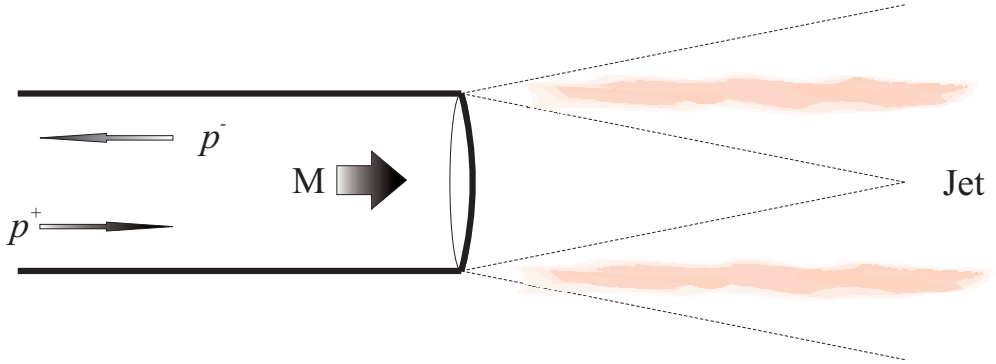

FIGURE 3.2: Simple unflanged duct termination with flow.

As a first application it was decided to employ the method to assess the effect of the jet formed as flow exits an unflanged duct on the sound radiated to the farfield. A number of publications, both theoretical [5, 76, 77] and experimental [41, 69], deal with the subject and highlight that low frequency sound absorption occurs due to the vortex shedding from the duct termination. Cargill [76] provides an expression for the acoustic power radiated, W_c from an unflanged duct with flow as

$$W_c = \frac{|\hat{p}^+|^2}{\rho c}(ka)^2 \frac{1 + M^2/3}{(1 - M^2)^3} S, \tag{3.5}$$

where $\hat{p}^+$ is the pressure wave component in the duct immediately incident to the duct termination and S is the duct cross-sectional area. By measuring the sound power flux immediately upstream of the duct termination as well as that radiated into the farfield the extent of absorption of acoustic power can be determined. The radiated sound power, W_r, was determined by measuring the farfield pressure, p_f, and assuming monopole radiation from the duct termination using

$$W_r \approx \frac{4\pi r^2 |p_f|^2}{\rho c} \tag{3.6}$$

where r is the radial distance of the farfield microphone from the centre of the duct termination. The assumption of monopole radiated was tested by measuring the

directivity of the sound field radiated from the duct termination. The results of this assessment are detailed in Appendix A.3. The results indicate that although the radiated field is not strictly monopole by positioning the farfield pressure at 60^o to the duct central axis an acoustic pressure within 10% of the mean acoustic pressure of the radiated field is determined over the frequency range of 50-2000Hz.

In this section a comparison of the measured acoustic absorption with that predicted by Cargill is presented. The comparison of such results allow for the validity of the source measurement method to be further assessed. In addition the comparison provides a validation of Cargills prediction of the sound absorption with flow.

3.3.1 Experimental set-up

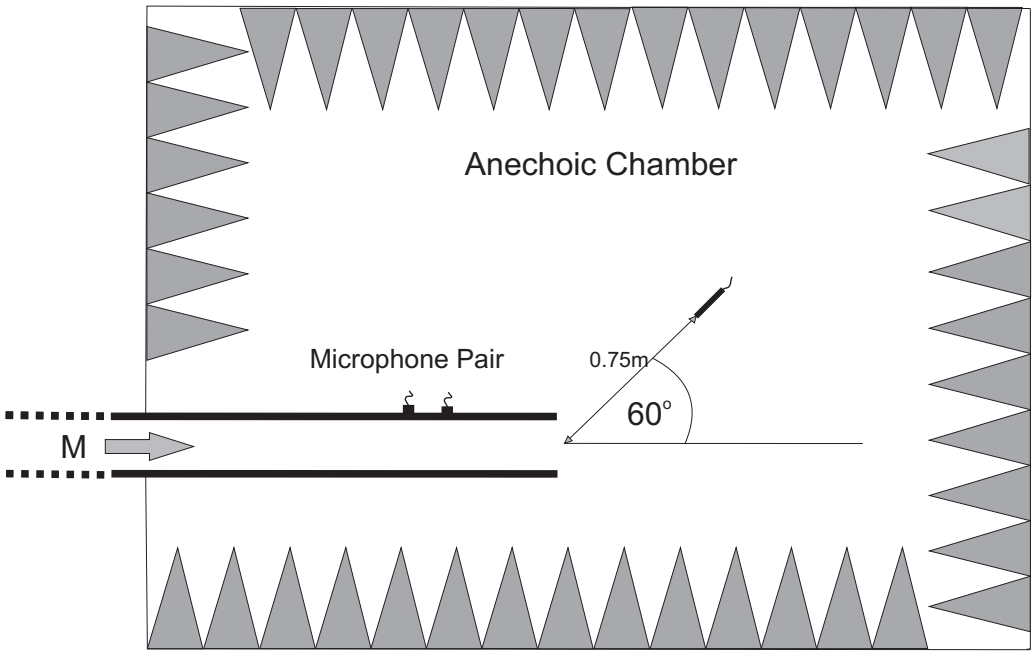

FIGURE 3.3: Experimental set-up for measurement of acoustic sink due to jet formed at a duct exhaust.

Figure 3.3 describes the experimental configuration employed to measure the extent of sound absorption due to a jet formed at a duct exhaust. It consists of a pair of flush wall mounted microphones position at 120mm and 195mm upstream of the duct termination. An additional microphone was positioned in the anechoic chamber 750mm from the duct termination at 60° to the duct central axis. The system was excited using a loudspeaker located upstream in the duct as detailed in

the section 2.4. The microphone's relative phase and magnitude were calibrated using the sensor switching technique discussed in section 2.3.3. Pressure time series were acquired simulateously from all the microphones for a range of duct mean outflow Mach numbers between 0 and 0.3. A sine-sweep/selective averaging technique as discussed in section 2.3.2 was used for all measurement to provide an improved signal-to-noise ratio to that of broadband excitation.

3.3.2 Results

Figures 3.4-3.9 compare the measured acoustic power radiated from an unflanged duct with that predicted using eqn 3.5. Both the measured and predicted sound power are normalised using the power flux experimentally determined at the duct termination and plotted in dB. Each plot is for a different jet mean Mach number with the solid line indicating the measured radiated sound power and the dotted line indicating the prediction of Cargill. It should be noted that although the FFT analysis used to the assess the results provided a spectral binwidth of 1.346Hz the results displayed were smoothed by averaging over 20Hz steps.

It can be observed from the figures that the prediction and measurements follow a similar trend with the extent of absorption of acoustic power from the jet increasing with decreasing Helmholtz number. Also, both the prediction of Cargill and the measured results are within 1.5dB of each other above ka =0.1. Below this value of ka the difference increases to up to 5dB, however this is likely due to the low signal-to-noise ratio which existed at this low frequencies.

Essentially the results in conjunction with the prediction of Cargill indicate that the sound power radiated from an unflanged duct with flow is absorbed by the jet. The level of absorption tends to increase with increasing flow velocity as well as decreasing Helmholtz number. Consequently, it is possible to control the amount of sound power absorption at a duct termination by modifying the Helmholtz number of the duct termination. For example, to increase the absorption for at a specific frequency the duct radius at the exit should be decreased which will simultanouesly increase the flow velocity for a given mass flow rate and decrease the Helmholtz. Finally, the close match of the measured radiated power with that predicted using the sound power flux determined in the duct adds confidence to the sound power flux measurement technique employed.

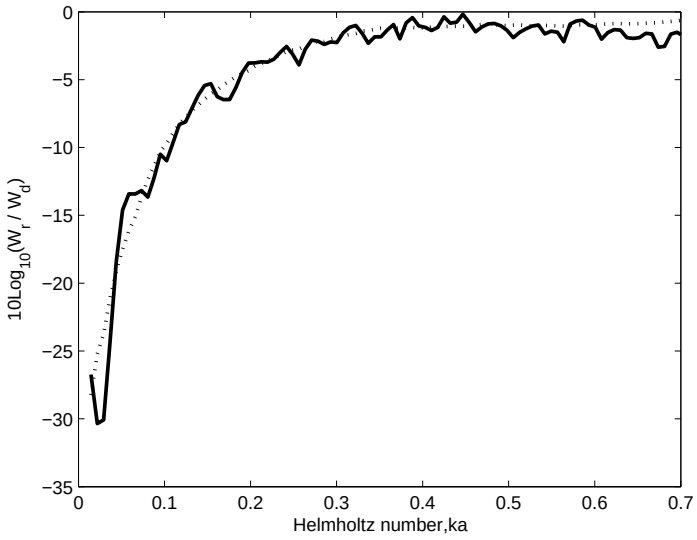

FIGURE 3.4: Comparison of measured radiated acoustic power (-) to that predicted by Cargill(..) for a jet mean Mach number of 0.049. Results normalised with sound power flux determined immediately upstream of duct termination.

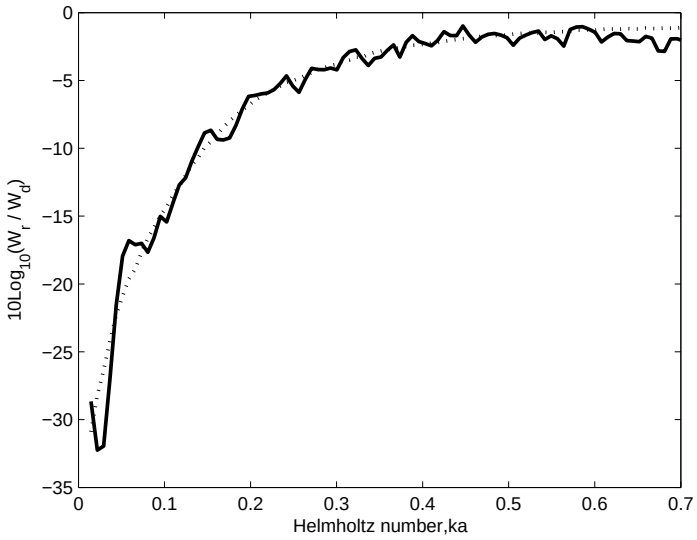

FIGURE 3.5: Comparison of measured radiated power (-) to that predicted by Cargill(..) for a jet mean Mach number of 0.09. Results normalised with sound power flux determined immediately upstream of duct termination.

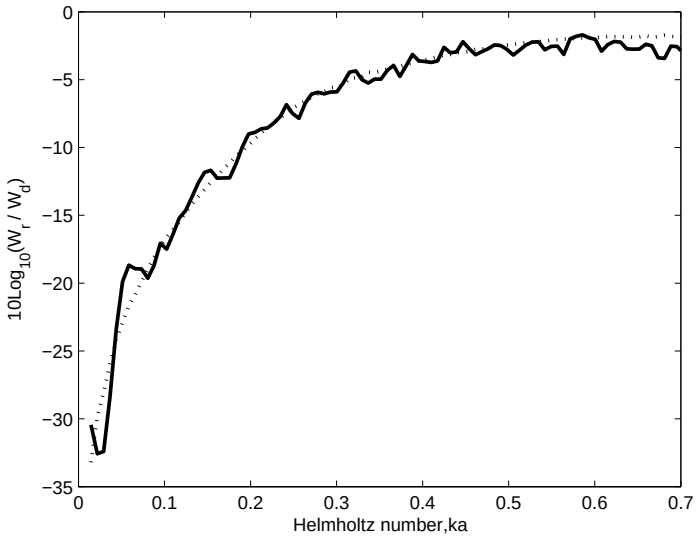

FIGURE 3.6: Comparison of measured radiated power (-) to that predicted by Cargill(..) for a jet mean Mach number of 0.14. Results normalised with sound power flux determined immediately upstream of duct termination.

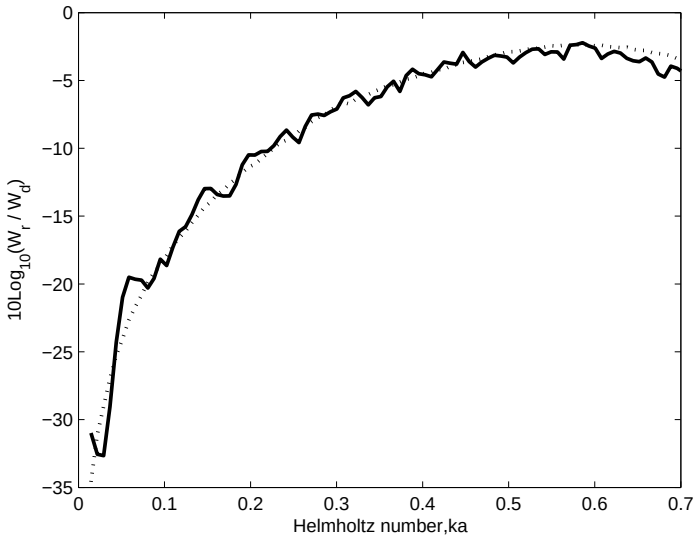

FIGURE 3.7: Comparison of measured radiated power (-) to that predicted by Cargill(..) for a jet mean Mach number of 0.184. Results normalised with sound power flux determined immediately upstream of duct termination.

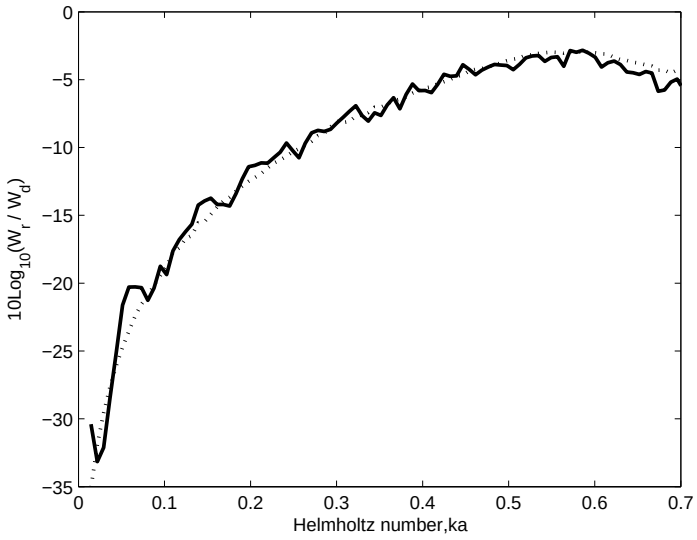

FIGURE 3.8: Comparison of measured radiated power (-) to that predicted by Cargill(..) for jet mean Mach number of 0.235. Results normalised with sound power flux determined immediately upstream of duct termination.

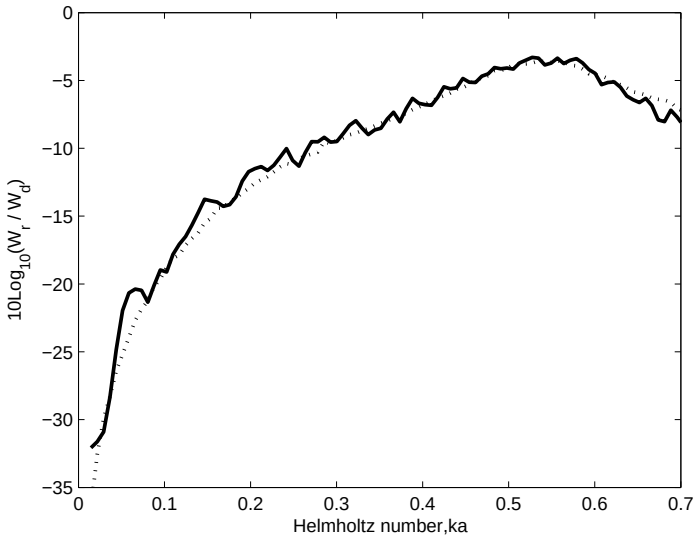

FIGURE 3.9: Comparison of measured radiated power (-) to that predicted by Cargill(..) for jet mean Mach number of 0.282. Results normalised with sound power flux determined immediately upstream of duct termination.

3.4 Acoustic power flux in a simple expansion

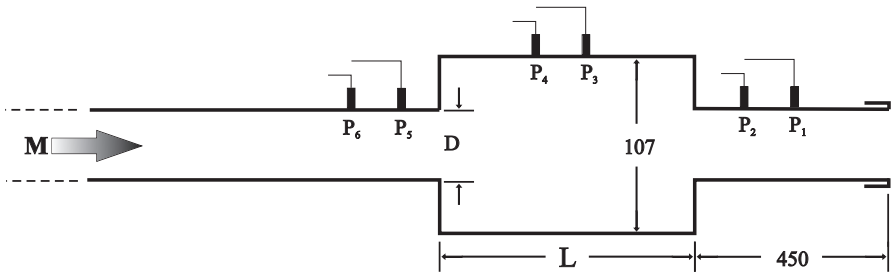

FIGURE 3.10: Schematic of experimental set-up used to measure the sound power flux in a simple expansion chamber.

Measurements of the acoustic power flux were made at different locations in a simple expansion chamber with and without flow. Figure 3.10 describes the general experimental set-up with pairs of microphones positioned flush with the inner wall of the tailpipe, chamber and inlet pipe. The system was acoustically excited using a loudspeaker upstream as described in figure 2.5 of section 2.4. The acoustic pressure wave components were determined using the wave decomposition technique described in section 2.2 at measurement locations 1, 3, & 5 described in figure 3.10. Figure 3.11 is a plot of the measured amplitude and phase of the acoustic transfer function between microphone location 1 & 5 with that predicted using APEX. APEX is a commercial software package that models the plane wave acoustic characteristics of ducts with flow and is based on a combination of linear acoustic theory and empirical data[78]. Significantly, APEX does not include effects of aeroacoustic sources.

It is apparent from the comparison that the magnitude of the measured transfer function remains well within 0.5dB of the prediction for the majority of the frequency range. The discrepancies between the APEX prediction and the measurements at higher frequencies are likely attributable to subtle difference the effect of evanescent higher order modes at the chamber inlet and outlet. However, the results indicate the higher precision at which the transfer function amplitude and phase were measured. Such transfer function measurements were used to determine the pressure wave components at each microphone measurement plane as described in section 2.2.The acoustic power flux was then determine using eqns 3.2 & eqns 3.3. In order to determine the sound power loss across the chamber the duct system was excited at very high sound pressure levels and the mean tailpipe Mach number kept below 0.1. Consequently, it is believed that the sound power

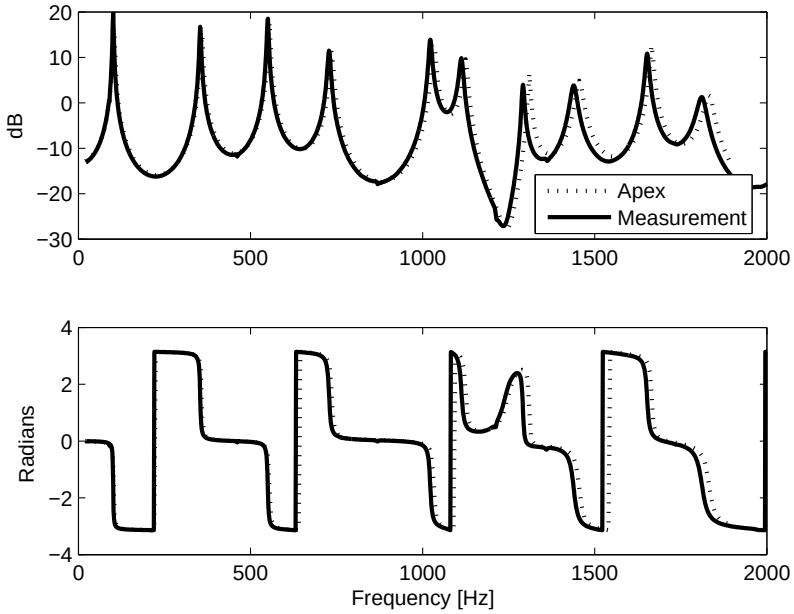

FIGURE 3.11: Amplitude and phase of predicted and measured transfer function , H_{15}, between microphones 1 & 5.

level generated by any aeroacoustic source would be secondary to that generated by the loudspeaker.

Figure 3.12a is a plot of the sound pressure level (SPL) [ref 20μPa] measured at microphone location 5 for a system excited by the loudspeaker with no flow for a chamber of Length, $L = 10D$. It is apparent from the figure that the SPL is generally very high achieving levels of up to 140dB and that the SPL varies as a function of frequency. The sharp peaks which occur at approximately every 90Hz are associated with resonances of the total system from the silencer exit to the tailpipe termination. The significant dips at approximately 870Hz, 1215Hz and 1363Hz are associated with pressure nodes existing at the microphone measurement plane. The dip in the SPL at 970HZ is associated with low excitation levels generated by the loudspeaker. This can be verified by examining Figure 3.12b which shows a plot of the net acoustic power flux determined at microphone measurement plane 5. A dip in the acoustic power flux is clearly apparent at 970Hz. Further investigation indicated that the length of flexible coupling which attached the loudspeaker to the duct system has a length comparable to a half wavelength of this frequency. It is likely that the acoustic impedance is high at the loudspeaker at this frequency due to a half wave resonance of this coupling.

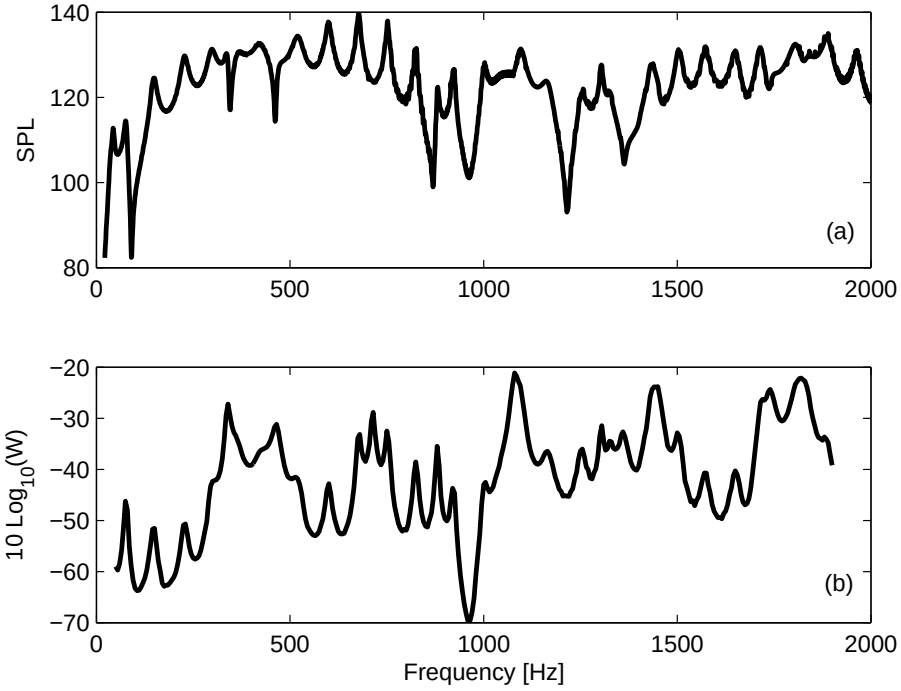

FIGURE 3.12: Sound pressure level (a) and acoustic power flux (b) measured at microphone 5 for a system excited by the loudspeaker upstream with no flow.

3.4.1 Comparison between measurement and prediction

In this section a comparison is made between the measured sound power flux with that predicted using APEX. Figures 3.13, 3.14 & 3.15 are plots the acoustic power flux for expansion chambers of length 6D, 8D, and 10D respectively. The acoustic power flux is plotted as a ratio of the net acoustic power flux in the tailpipe to that in the inlet pipe in dB. This allows for ease of comparison with the APEX predictions which provides normalised acoustic pressure wave components and allows for the effect of the chamber on the powerflux to be quantified. Examination of the plots for a mean tailpipe Mach number of zero indicates that the prediction of APEX and the measurement match within 2dB over the frequency range assessed which supports the validity of the measurements. It can be observed that the chamber has the effect of attenuating the acoustic power flux. The only attenuating mechanism is this case is the viscothermal attenuation coefficient. However, the extent of absorption is minimal at frequencies 365Hz, 375Hz, 1080Hz, 1440Hz & 1810Hz. This corresponds to the tailpipe resonance frequencies indicating that chamber sound power absorption is low at frequencies at which a pressure node exists at the tailpipe entrance. At this point it should be noted that the sharp

peak at 970Hz in figures 3.13 & 3.14 for M=0 & 0.033 is due to an increase in the error sensitivity at this frequency. This is due to the low signal levels generated by the loudspeaker at this frequency as discussed in the previous section. This disappears as the flow velocity increases as sufficient noise is generated by the flow to overcome this issue.

As the flow increases the spectral shape of the sound power absorbed is modified with additional peaks occurring in both the measured and predicted results apparent. However, differences between the APEX prediction and the measured results are greater than in the no flow case. Significantly the extent of sound absorption is less in the measured data than that predicted at frequencies at which the sound absorption is considered to be high i.e. at the dips in the spectra around 240Hz, 500Hz, 950Hz, 1240Hz & 1740Hz. For example, the difference is 5.5 dB at 1010Hz for an expansion chamber of length 6D with mean tailpipe Mach number of M = 0.033. There are a number of possible reasons for this (i) increased error in the results due to the presence of flow (ii) The prediction of Apex overestimating the sound power absorption or (iii) the presence of an aeroacoustic sources in the chamber. The author expects it likely to be a combination of (i) and (iii). The effect of aeroacoustic sound generation in simple expansion chambers will be addressed in chapter 5.

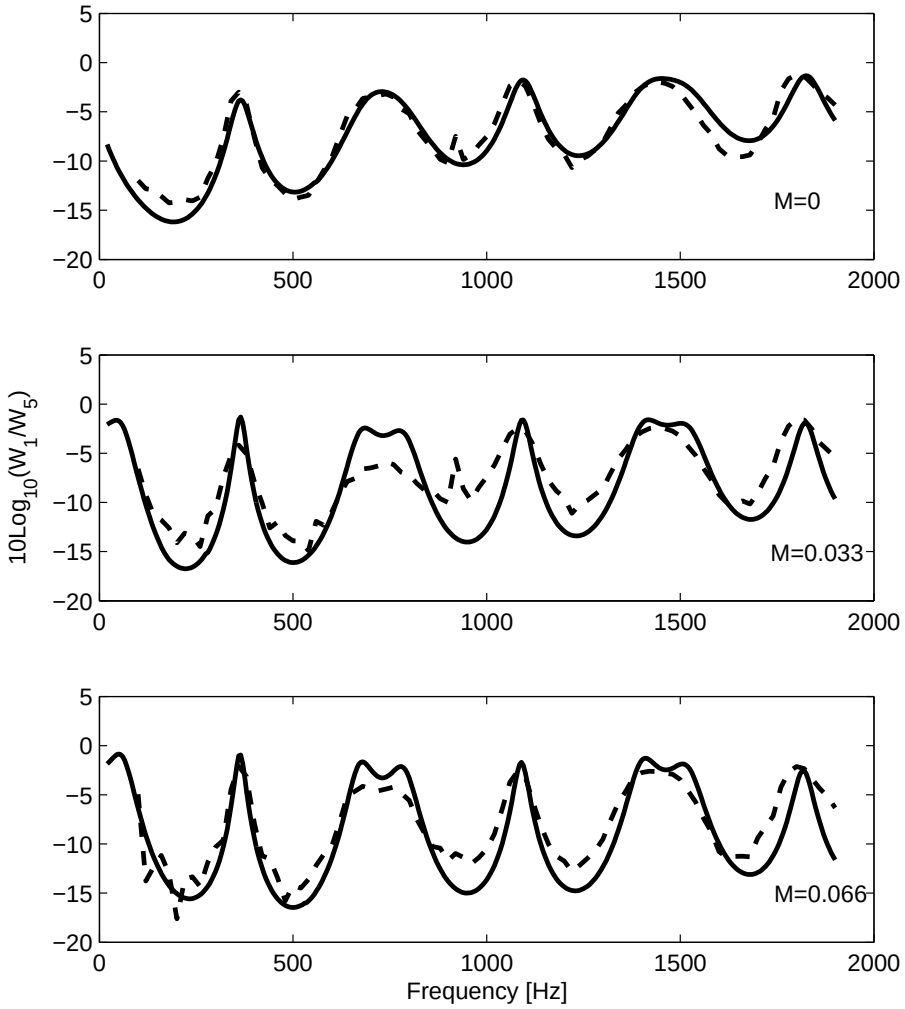

FIGURE 3.13: Ratio acoustic power flux measured downstream of chamber to that measured upstream of chamber. Chamber length 6D. Measured (- -) and predicted (-).

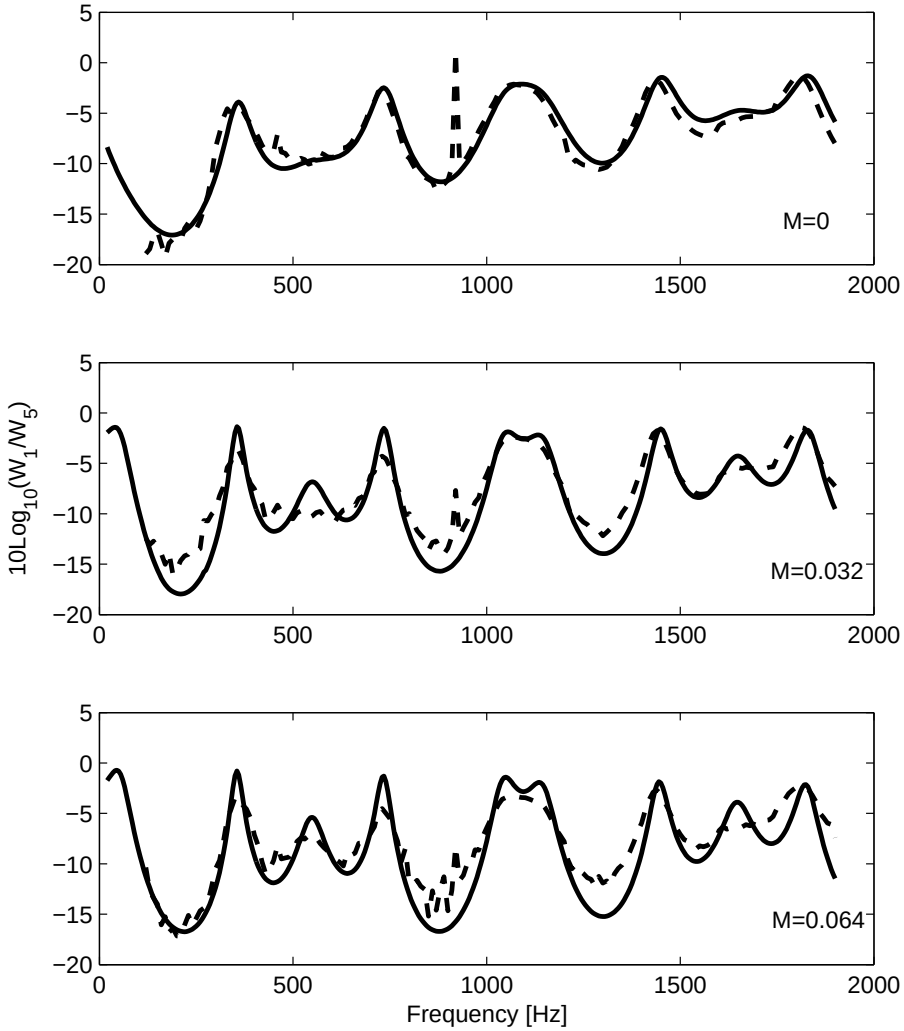

FIGURE 3.14: Ratio acoustic power flux measured downstream of chamber to that measured upstream of chamber. Chamber length 8D. Measured (- -) and predicted (-).

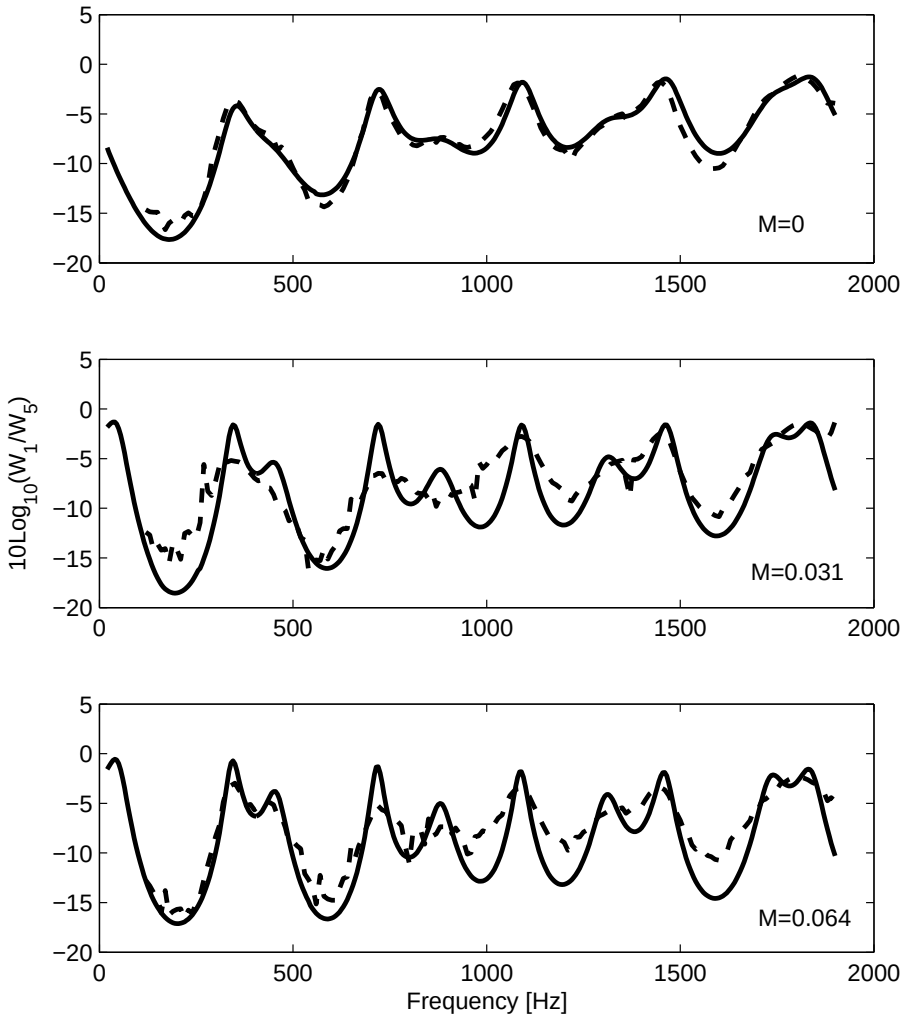

FIGURE 3.15: Ratio acoustic power flux measured downstream of chamber to that measure upstream of chamber. Chamber length 10D. Measured (- -) and predicted (-).

3.5 Method for measurement of aeroacoustic source strength

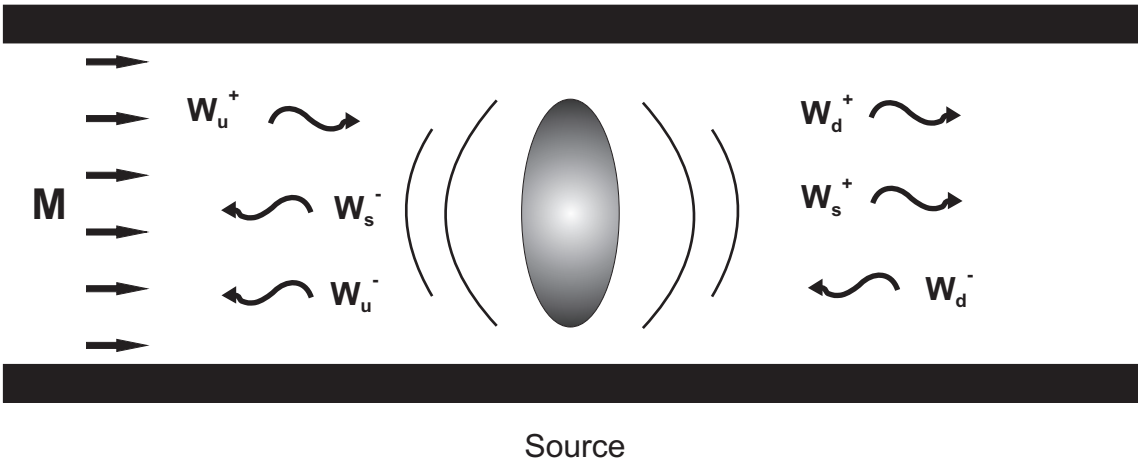

FIGURE 3.16: Aeroacoustic source in a duct

As mentioned, in the absence of an aeroacoustic source or sink, the net sound power flux in a duct with flow does not change. However, if a source or sink is present the net sound power flux either side of the source of sink is modified. Considering this figure 3.16 decribes a simple source in a duct with flow. The net acoustic power flux immediately upstream of the source, $\bar{W}_u$, can be defined as

$$\bar{W}_u = W_u^+ - W_u^- - W_s^+, \tag{3.7}$$

where W_u^+ is the acoustic power flux incident to the acoustic source, W_u^- is the acoustic power flux associated with the reflected pressure wave component in the duct, and W_s^- is the acoustic power flux associated with the aeroacoustic source itself. Similarly, the net acoustic power flux immediately downstream of the source, $\bar{W}_d^-$ can be defined as

$$\bar{W}_d = W_d^+ - W_d^- + W_s^+. \tag{3.8}$$

Based on this, the total aeroacoustic source strength can be defined as

$$\bar{W}_s = W_s^+ + W_s^- = \bar{W}_d - \bar{W}_u. \tag{3.9}$$

Using this definition of an acoustic source, the acoustic source strength can be determined by measuring the acoustic powerflux both upstream and downstream of the source region in a duct.

3.6 Verification of measurement technique

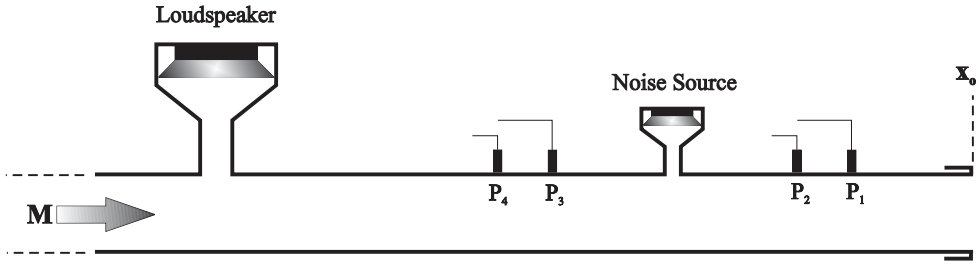

FIGURE 3.17: Schematic describing experiment creating an artifical source

In order to test the validity of the source measurement technique an experiment was developed to create a known source within a duct. Figure 3.17 describes the basic experimental setup. It consists of a straight Perpex tube with a 40mm internal diameter, terminated with an unflanged open end with a 4mm wall thickness located in an anechoic chamber. Four microphones are mounted flush with the inner wall of the duct at 160mm, 235mm, 755mm &830mm upstream of the duct termination, corresponding to locations 1,2,3 & 4 respectively. A noise source was created between locations 2 & 3 at 595mm upstream of the duct termination. The noise source was a loudspeaker connected to the main duct system via a side-branch with a 10mm internal diameter. A thermocouple was mounted at 730mm upstream of the duct termination. Figure 3.18 is a picture of the experimental rig. During measurement the loudspeaker used to create the artificial noise source is covered with absorptive foam to ensure any sound radiating from the speaker casing is sufficiently attenuated. In order to determine the acoustic powerflux pressure time histories are acquired simultaneously from each of the microphones. The transfer function between microphones 1 & 2, and microphones 3 & 4 allow for pressure wave components $\hat{p}^+$ and $\hat{p}^-$ to be determined either side of the noise source as detailed in 2.2. Sound power flux can then be determined either side of the source location using

$$\bar{W} = \frac{S}{\rho c}\left(\left|\hat{p}^+\right|^2 (1+M)^2 - \left|\hat{p}^-\right|^2 (1-M)^2\right). \tag{3.10}$$

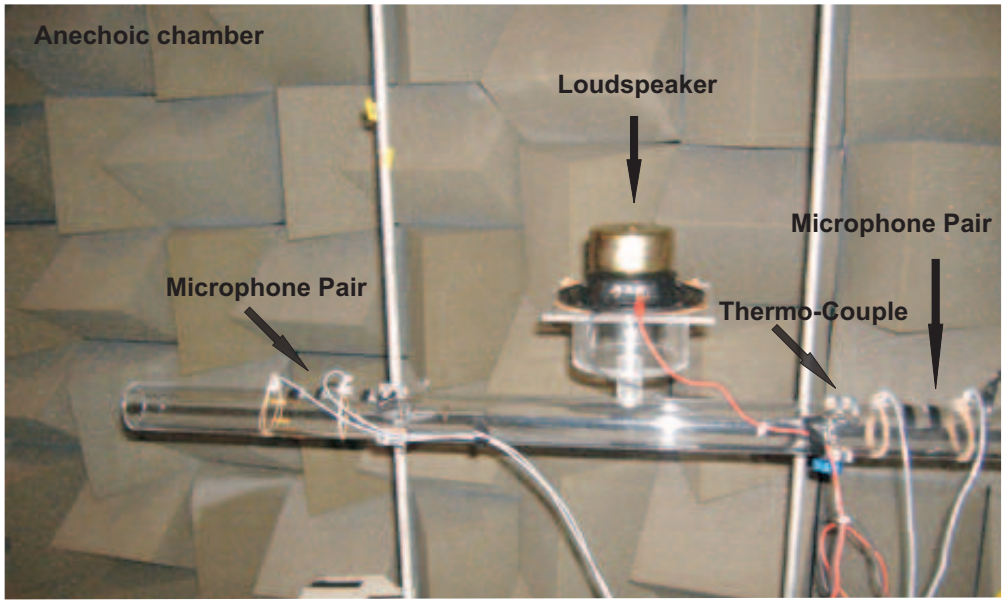

FIGURE 3.18: Experimental Set-up

To assess the validity of the technique an artificial source is created at the known frequencies of 400Hz, 800Hz, 1200Hz, 1800 Hz. The voltage of the signal into the amplifier of the speaker for each test is 0.5V, 1.0V, 2.0V & 4.0V. Since the amplitude response of the speaker and speaker amplifier is linear each doubling of input voltage should represent a 6dB increase in the source strength measured. This is valid so long the wave amplitude generated by the speaker remains significantly below that at which wave steepening occurs and the yielding of the duct wall is minimal. In addition, to remove any contribution of uncorrelated flow or system noise the results the coherent sound power flux spectrum is calculated.

$$\bar{W}_{nm} = \bar{W}_{nm} * \gamma^2_{nm} \tag{3.11}$$

where $\bar{W}_{nm}$ represents the sound power flux calculated by pressure time series measurements at measurement planes n and m [43].

3.6.1 Results

Figure 3.19 plots the source strength determined using the source measurement technique for an speaker amplifier input signal at 400Hz with signal input voltages of 0.5V, 1V, 2V & 4V. The source strength is plotted in dB [ref 1V] for each of the voltage amplitudes of the amplifier input signal and clearly exhibit peaks in

the spectra at 400Hz. In addition, the background noise level over the rest of the spectra generally remains less than -100dB with notable exceptions at harmonics of the source frequency and below 100Hz when there is an increase up to -80dB. This analysis was repeated for amplifier input frequencies of 800Hz, 1200Hz and 1800Hz. The magnitude of the source strengths measured are plotted in figure 3.20 as a function of amplifier signal input voltage. It is apparent from figure 3.20 that the magnitude increases approximately 6dB as expected for each doubling of input signal magnitude at all frequencies tested. Further examination indicates that the magnitude response for each doubling of input voltage varies over the range 5.68 - 6.06dB. From the results it is concluded that the source measurement technique allows for the source frequency and amplitude to be determined over the frequency range assessed to within approximately 0.5dB.

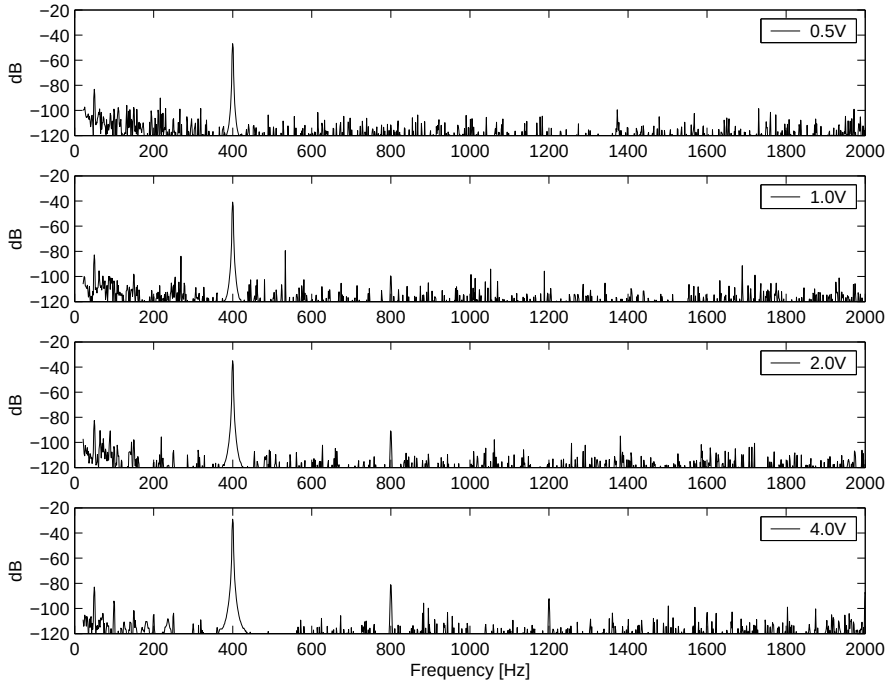

FIGURE 3.19: Acoustic power of artifical source, W_s, determined at side branch transfer plane using the source measurment technique described in sec 3.5 for a range of speaker amplifier input signal voltages at 400Hz. Results plotted in dB [ref 1W].

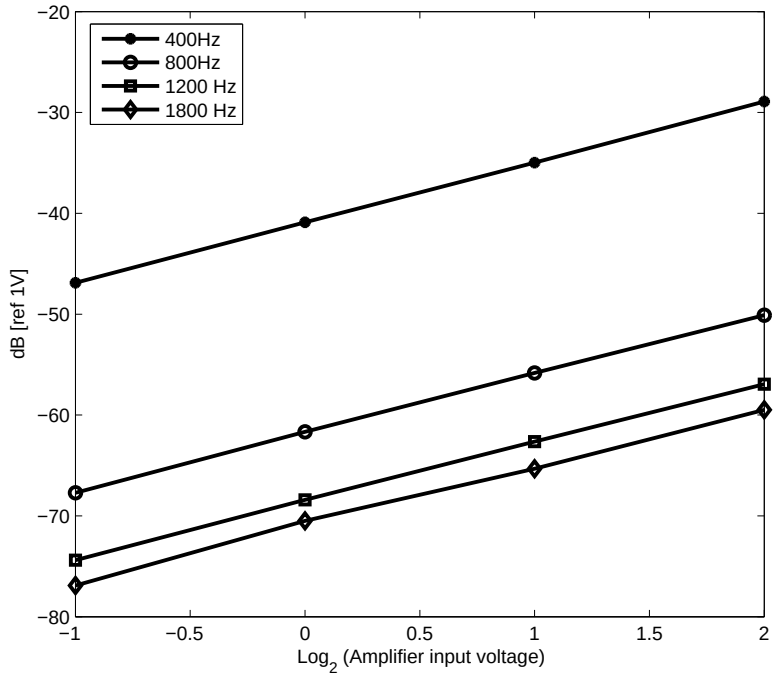

FIGURE 3.20: Magnitude of acoustic power of artificial source, W_s, determined at side branch transfer plane using the source measurement technique described in sec 3.5 as a function of speaker amplifier input signal voltages at 400hz, 800hz, 1200hz & 1800Hz. Results plotted in dB [ref 1W].

3.7 Conclusions

In this chapter a method for the measurement of the acoustic power flux in ducts with flow has been presented. The method is applied to assess the sound absorption of sound power by the jet formed at the exit of a simple duct termination with flow, as well as the absorption of sound power in a simple expansion chamber. Comparison of the results with that predicted by theory and commercial software APEX indicate that the sound power flux measurement technique is valid. The results indicate that aeroacoustic sources possibly exist in the expansion chamber. A technique for measuring the aeroacoustic source strength in ducts with flow has been presented. The experimental technique has been validated by creating an artificial source in a duct with no flow. The results from the experiment show that the technique can determine the frequency and amplitude of acoustic source to within 0.32dB. This technique will be applied in the subsequent chapters to measure the aeroacoustic source strength of standard duct geometry such as the in-duct orifice and the expansion chamber.

Chapter 4

Aeroacoustics of an in-duct orifice

4.1 Introduction

In-duct orifices are common elements in piping systems used as part of flow measurement streams as well as a means of restricting the flow rate (gas flare systems). In addition, they are also used as features in exhuast systems as a means of attenuating sound propagation. It is the objective of this chapter to assess the aeroacoustic characteristics of a simple orifice in a duct with flow applying the measurment techniques presented in chapters 2 & 3. This chapter assesses both the subject of sound absorption and of sound generation from flow through an in-duct orifice for frequencies below the cut-on of the first higher order mode. Section 4.4 presents an equation for the sound power absorbed by the shear layer which forms immediately downstream of the orifice. A comparison of the sound power absorption predicted with that measured is presented and discussed. Section 4.5 compares published semi-emperical models for the sound power radiated from an in-duct orifice with flow. The section also presents in-duct source measurements determined by applying the source measurement technique presented in chapter 3. The results of both the sound absorption and source measurements highlight the importance of the local acoustic field on both the extent of sound absorption and the source strength.

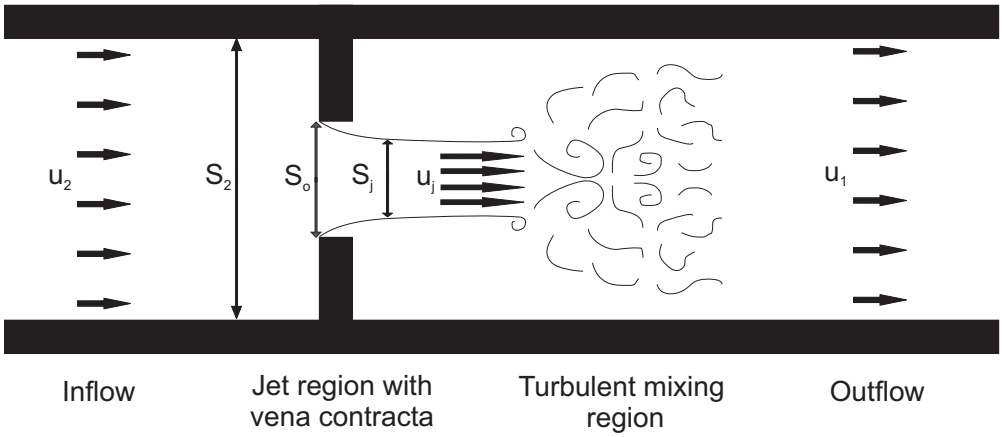

FIGURE 4.1: Schematic drawing of steady flow through an orifice in a duct. The inflow region can be considered fully developed turbulent pipe flow. The flow is then accelerated through the orifice where it seperates at the leading edge and forms a jet [7]. The jet eventually fully expands into a turbulent mixing region at approximately 5-7 orifice diameters downstream [8]

4.2 Background theory

Figure 4.1 is schematic detailing the general character of flow through an orifice in a duct which is divided in a number of characteristic zones. The inflow region consists of fully developed turbulent pipe flow. The flow is then accelerated through the orifice and separates to form a jet [7]. The flow separation causes an additional contraction of the flow further downstream from the orifice upstream edge. This is known as a vena contracta effect with the vena contraction ratio, $\frac{S_j}{S_o}$, a function of orifice to duct cross-sectional area ratio, $\frac{S_o}{S_j}$, as well as jet Mach number, M_j [7]. The jet fully expands resulting in a turbulent mixing after be approximately 5 orifice diameters downstream for an area ratio of 3, reaching values of up to 7 as the area ratio increases [8]. The flow then undergoes recovery toward fully developed turbulent flow at large distances downstream of the orifice plate [79].

The vortex shedding associated with the jet shear layer is the fluid dynamic mechanism by which sound is either generated or absorbed [80]. Insight into such energy transfer is provided by Howe's acoustic power integral [49]

$$\langle W \rangle = -\rho \int_V \left\langle \left(\varpi \times \bar{U} \right) \cdot \hat{u} \right\rangle dV \tag{4.1}$$

where ϖ is the vorticity vector and V is the volume enclosing the vorticity. Eqn 4.1 indicates that acoustic power is effectively generated when there exists an

appropriate phase relationship between the vortical structures and the acoustic particle velocity. In addition the transfer of energy from the vortical field to the acoustic field is at a maximum when the acoustic particle velocity is at a maximum i.e. at a pressure node.

4.3 Measurement method

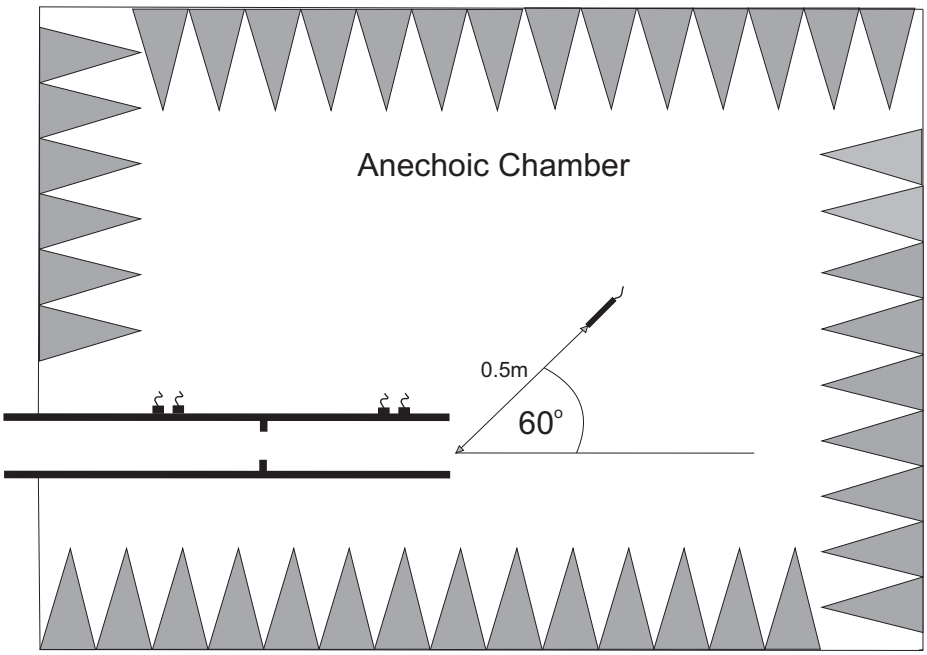

FIGURE 4.2: Schematic of orifice experiment configuration. Set-up consists of a simple cylindrical Perspex tube with an internal diameter of 40mm. An orifice plate is fitted with its upstream edge located 500mm upstream of the unflanged open duct termination. Microphone pairs are positioned both upstream and downstream of the orifice with an additional microphone position in the anechoic chamber 500mm from the duct termination at 60° to the duct center axis.

In order to assess the properties of an induct orifice an experimental rig as outlined in Figure 4.2 was developed. The experimental rig was located in the anechoic chamber of the ISVR Doak lab. Flush wall mounted microphones were position at 120mm, 195mm, 640mm & 715mm upstream from the duct termination corresponding to microphone positions 1 - 4 respectively. An additional microphone (# 5) was position in the farfield at 60^o to the duct center axis at a radius of 500mm from the duct termination. The flow temperature was measured using a thermocouple mount flush with 665mm upstream of the duct termination. The orifice plate fixed within the duct with the downstream facing edge located

at 497mm upstream of the duct termination. Simultaneous pressure time series were acquired using a National Instruments PXI-4472 8 Channel acquisition cards. Measurements were taken for a range of flow velocity with and with out acoustic excitation via a loud speaker coupled to the pipework upstream of the orifice.

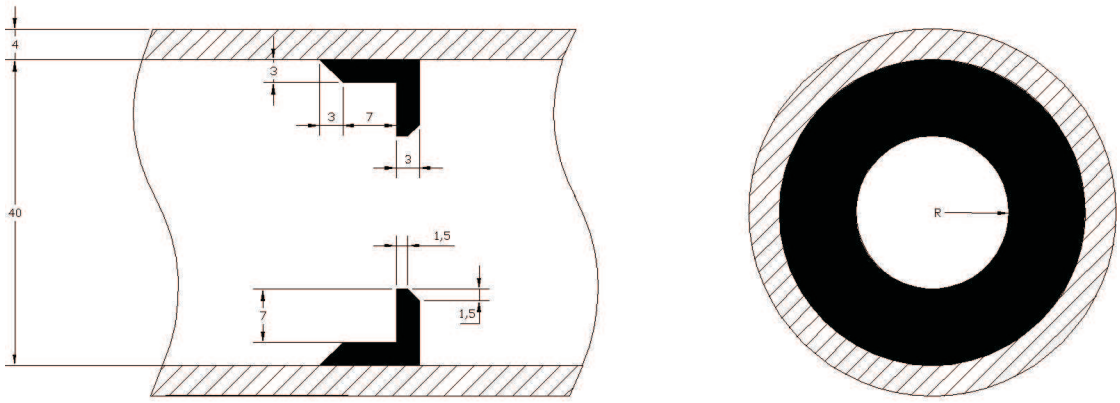

FIGURE 4.3: Geometric detail of orifice fitted within duct. All dimensions in millimeters. Measurements carried out for orifice radii, R, of 14.1mm, 11.5mm and 10mm. Flow travels from left to right.

Figure 4.3 is a schematic detailing the orifice plate geometry fitted inside a Perspex duct with 4mm wall thickness. The orifice plate was made out of aluminum and fixed in position via a screw in the Perspex wall. A total of 3 orifice geometries were employed for the tests with orifice radii, R, of 14.1mm, 11.5mm and 10mm corresponding to duct-to-orifice area ratios of 2, 3 & 4 respectively.

4.3.1 Rejection of flow noise using a coherence function method

Due to high levels of turbulent kinetic energy downstream of the the orifice plate a three microphone method for the rejection of flow noise was adopted. The method was first presented by Chung [44] and is based on the coherence functions between each of the microphone signals. The method works on the basis that the flow noise at the three transducer is mutually uncorrelated. For the orifice experiment described in figure 4.2 the coherence between the two induct microphones (#1 & #2) downstream of the orifice and the microphone position in the farfield(#5) were used to provide a coherent power flux spectrum. This is done by determining the coherent autospectrum which in turn is used to calculate the pressure wave components as outlined in section 2.2. The coherent autospectrum associated with each microphone is defined as

$$\begin{aligned} G_{1'1'} &= G_{11}\frac{\gamma_{12}^2\gamma_{51}^2}{\gamma_{25}^2}, \\ G_{2'2'} &= G_{22}\frac{\gamma_{25}^2\gamma_{12}^2}{\gamma_{51}^2}, \\ G_{5'5'} &= G_{55}\frac{\gamma_{51}^2\gamma_{25}^2}{\gamma_{12}^2}. \end{aligned} \tag{4.2}$$

The left-hand side of eqn 4.2 consists of the autospectra associated with the acoustic pressure signal at each location without extraneous noise. On the right hand side are the basic autospectra and the coherence function relations which form the basis of the noise rejection method [44].

Figure 4.4 is a comparison of the experimentally determined coherence function, γ_{12}^2, with that of the coherence function relation $\frac{\gamma_{12}^2\gamma_{51}^2}{\gamma_{25}^2}$. The results are for flow through an orifice with a duct to orifice area ratio of 2 and a mean Mach number of 0.15. It can be clearly seen from the plot that the magnitude of the coherence is typically higher than that of the coherence function relation. This difference is due to hydrodynamic pressure fluctuations correlated over the distance between microphone #1 & #2 contributing to the associated measured signals. However, microphone #5 is not in the flow but is assumed to be in the same sound field and so any correlation with signals #1 & #2 is due to the acoustic field alone.

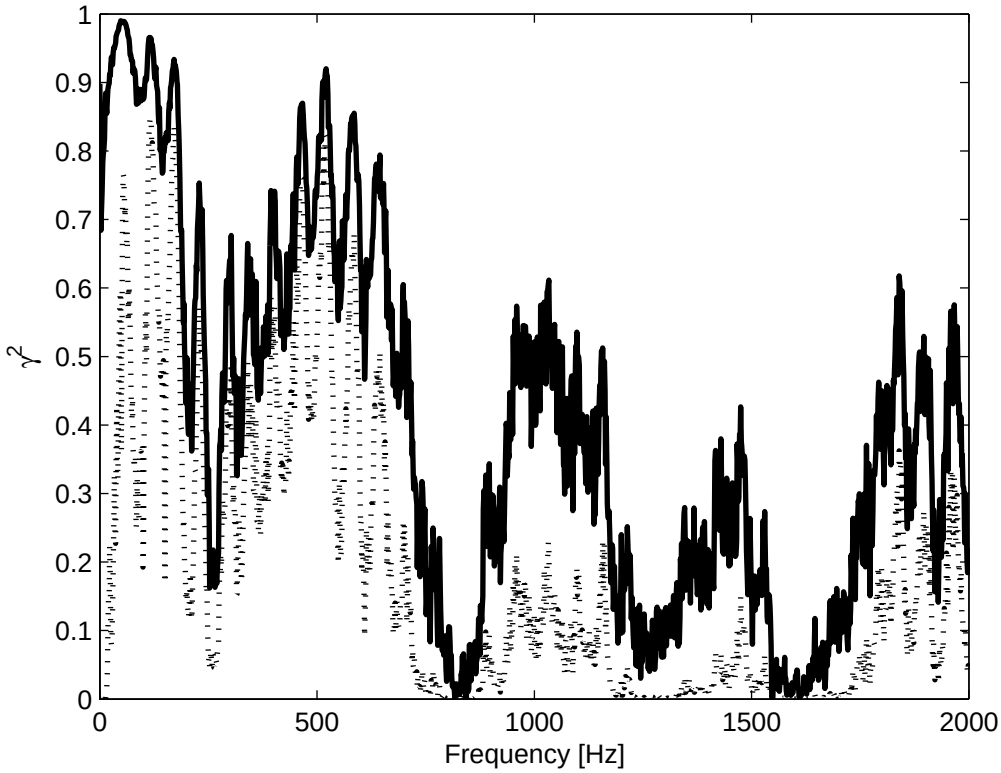

FIGURE 4.4: Comparison of experimentally determined γ_{12}^2 (-), with the coherence function relation $\frac{\gamma_{12}^2\gamma_{51}^2}{\gamma_{25}^2}$ (..). Results are for an orifice with a duct to orifice area ratio of 2 and a mean duct Mach number of 0.15.

Consequently the coherence function relation calculated is generally smaller in magnitude when flow is present. If there was no flow the coherence and the coherence function relation would become equivalent. It is also apparent from figure 4.4 that there is a low coherence at approximately 800Hz, 1250 and 1550Hz. This is a result of a low signal-to-noise ratio due to pressure nodes existing at these frequencies at certain microphone locations. It will be shown in the subsequent sections that this impairs the quality of the results at these frequencies.

4.4 Sound absorption through an induct orifice with flow

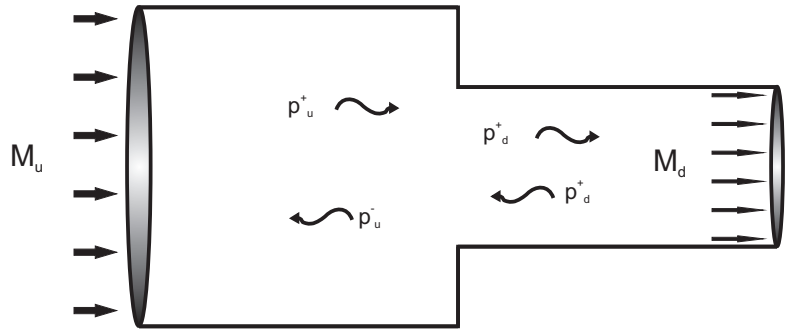

FIGURE 4.5: Abrupt area contraction in a cylindrical duct with flow.

So long as the acoustic wave propagation can be considered substantially planar the aeroacoustics of an orifice plate can be considered similar to that of a sudden area contraction followed by an equivalent sudden area expansion. The flow conditions at a contraction can normally be considered to be approximately isentropic on both sides of the discontinuity. Under such conditions the wave transfer across a contraction can be defined by the equations of conservation of energy and continuity of mass [23]. For the system described in figure 4.5 these can be expressed as

$$(1 + M_u)\,\hat{p}_u^+ + (1 - M_u)\,\hat{p}_u^- = (1 - M_d)\,\hat{p}_d^+ + (1 - M_d)\,\hat{p}_d^-, \tag{4.3}$$

and

$$S_u\left(\hat{p}_u^+\,(1 + M_u) - \hat{p}_u^-\,(1 - M_u)\right) = S_d\left(\hat{p}_d^+\,(1 + M_d) - \hat{p}_d^-\,(1 - M_d)\right). \tag{4.4}$$

Where subscript u denotes system parameters immediately upstream of the contraction and subscript d indicates parameters immediately downstream of the contraction. Using these equations it can be shown that

$$\hat{p}_u^+ = \Delta^+\hat{p}_d^+ + \Lambda^+\hat{p}_d^-, \tag{4.5}$$

and

$$\hat{p}_u^- = \Lambda^-\hat{p}_d^- + \Delta^-\hat{p}_d^-, \tag{4.6}$$

where the coefficients Δ^+, Δ^-, Λ^+, & Λ^- are defined as

$$\Delta^+ = \frac{1+M_d}{1+M_u}\frac{S_u+S_d}{2S_u} \tag{4.7}$$

$$\Delta^- = \frac{1-M_d}{1-M_u}\frac{S_u+S_d}{2S_u}, \tag{4.8}$$

$$\Lambda^+ = \frac{1-M_d}{1+M_u}\frac{S_u-S_d}{2S_u}, \tag{4.9}$$

and

$$\Lambda^- = \frac{1+M_d}{1-M_y}\frac{S_u-S_d}{2S_u}, \tag{4.10}$$

Eqns 4.5 & 4.6 allow the acoustic power flux to be determined immediately upstream and immediately downstream of the duct area contraction in terms of the same wave components i.e as $p_u^{\pm}$ or $p_d^{\pm}$ only. This allows an easy comparison and indicates that the power flux is expected to be maintained either side of the contraction with $W_u = W_d$. Thus, there is no loss in acoustic energy at a sudden area contraction within a flow duct. This is as expected since conservation of energy is imposed on the acoustic transfer at the discontinuity.

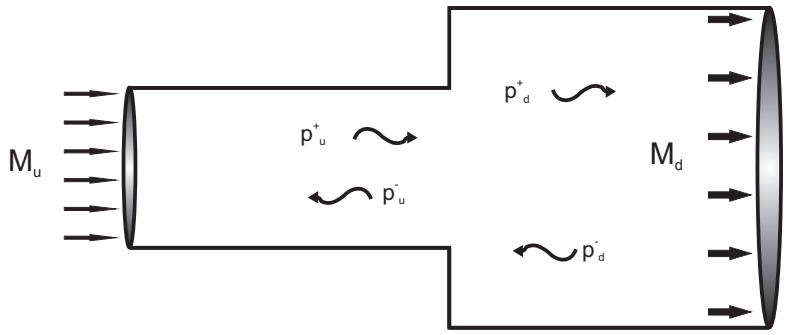

FIGURE 4.6: Abrupt area expansion in a cylindrical duct with flow.

The flow conditions at an area expansion in a duct are more complex than the conditions assumed for an area contraction. When flow reaches the expansion it separates and forms a jet. The shed vorticity associated with the shear layer provides a mechanism for the conversion of acoustical energy to vortical energy. Alfredson and Davies [23] modeled such a system can be modeled using conservation of mass, energy, and momentum flux as indicated by eqns 4.11, 4.12 & 4.13 respectively.

$$\left((1+M_u)\,\hat{p}_u^+ - (1-M_u)\,\hat{p}_u^-\right) S_u = \left((1+M_u)\,\hat{p}_d^+ - (1-M_u)\,\hat{p}_d^-\right) S_d + \psi S_u M_u, \tag{4.11}$$

$$\hat{p}_u^+ (1 + M_u) + \hat{p}_u^- (1 - M_u) = \hat{p}_d^+ (1 + M_u) - \hat{p}_d^- (1 - M_u) - \frac{\psi}{\gamma - 1}, \tag{4.12}$$

$$\begin{aligned} &\hat{p}_u^+ \left(S_d + S_u \left(2M_u + M_u^2\right)\right) + \hat{p}_u^+ \left(S_d + S_u \left(2M_u - M_u^2\right)\right) \\ &\quad = \hat{p}_d^+ \left(S_d \left(1 + M_u\right)^2\right) - \hat{p}_d^- \left(S_d \left(1 - M_u\right)^2\right) + \psi S_d M_u^2, \end{aligned} \tag{4.13}$$

where ψ is a fluctuation pressure arising from entropy fluctuations and is a function of viscosity and conductivity [81].

Using these expressions it was possible for the author to derive the acoustic power loss at an area expansion in a duct with flow. First equations 4.11, 4.12 & 4.13 are used simultaneously to eliminate ψ and define the pressure wave component transfer across the expansion as

$$\hat{p}_d^+ = \Phi_+ \hat{p}_u^+ + \Theta_+ \hat{p}_u^-, \tag{4.14}$$

$$\hat{p}_d^- = \Theta_- \hat{p}_u^- + \Phi_- \hat{p}_u^-, \tag{4.15}$$

where the coefficients Φ_+, Φ_-, Θ_+, & Θ^- are defined as

$$\Phi_+ = \frac{\left(1 + 2M_u - (\gamma - 1)M_u^2\right) S_u + \left(1 + (\gamma - 1)M_u^2\right) S_d}{2(1 + M_u) S_d}, \tag{4.16}$$

$$\Phi_- = \frac{\left(1 - 2M_u - (\gamma - 1)M_u^2\right) S_u + \left(1 - (\gamma - 1)M_u^2\right) S_d}{2(1 - M_u) S_d}, \tag{4.17}$$

$$\Theta_+ = \frac{\left((\gamma - 1)M_u^2 - 1\right) (S_u - S_d)}{2(1 + M_u) S_2}, \tag{4.18}$$

$$\Theta_- = \frac{\left((\gamma - 1)M_u^2 - 1\right) (S_u - S_d)}{2(1 - M_u) S_2}. \tag{4.19}$$

By using eqns 4.14 & 4.15 in conjunction with eqns 3.1 & 3.2 allows for the acoustic power loss at the expansion to be expressed as

$$\begin{aligned} \rho c W_u - \rho c W_d = \\ \left|\hat{p}_u^+\right|^2 \left(S_u(1 + M_u)^2 - S_d(1 + M_d)^2 \Phi_+^2 + S_d(1 - M_d)^2 \Theta_-^2\right) \\ + \left|\hat{p}_u^-\right|^2 \left(S_u(1 - M_u)^2 - S_d(1 - M_d)^2 \Phi_-^2 + S_d(1 + M_d)^2 \Theta_+^2\right) \\ -2Re\left(\hat{p}_u^+ (\hat{p}_u^-)^*\right) \left(S_d \left(\Phi_+ \Theta_+ (1 + M_d)^2 \Phi_- \Theta_- (1 - Md)^2\right)\right) \end{aligned} \tag{4.20}$$

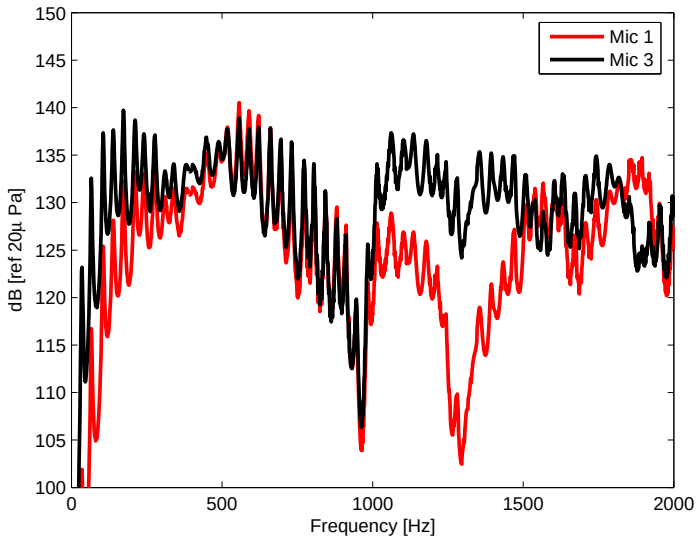

FIGURE 4.7: Sound pressure level measured within duct at microphone locations 1 & 3 for orifice absorption experiment with no flow.

Eqn 4.20 is a new prediction of the acoustic power loss at an orifice in a duct for frequency at which the wave motion is substantially planar. Examination of eqn 4.20 indicates that the extent of acoustic power loss through a shear layer within a duct is not only dependent on the fluid parameters such as the the density and ratio of specific heats, the relative fluid velocities and the local geometry, but also on the local acoustic field. This is highlighted by the presence of the term $-2Re\left(\hat{p}_u^+(\hat{p}_u^-)^*\right)$ in eqn 4.20 which is dependent on the phase relationship of the incident and reflected pressure wave components. Most importantly, the term $-2Re\left(\hat{p}_u^+(\hat{p}_u^-)^*\right)$ is lowest when $\hat{p}_u^+$ and $\hat{p}_u^-$ are in phase and highest when they are 180° out of phase. This indicates the sound absorption due to shear layers formed at sudden expansions in a duct (such as on orifice plate) will be highest at frequencies corresponding to pressure nodes immediately downstream of the expansion.

4.4.1 Comparison of theory with measurements

To assess the extent of absorption of sound due to flow through an in-duct orifice, measurements of the coherent sound power flux both upstream and downstream of the orifice were acquired with the duct system excited via a loudspeaker upstream of the orifice. The results are restricted to mean duct Mach numbers below M = 0.1 to ensure that any aeroacoustic source present at the orifice is dominated by the

acoustic field created by the loud speaker. This allowed the absorption associated with the orifice to be assessed rather than obscured by the orifice aeroacoustic source. Figure 4.7 is a plot of the sound pressure level (dB ref $20\mu Pa$) measured at microphone locations 1 and 3 as specified in section 4.3. The spectral shape of the excitation is dictated by the acoustic response of the pipe network used for the experiment. The distinct peaks in the spectra at approximately every 32 Hertz corresponds to a wavelength equivalent to twice the distance from the system loudspeaker and duct open end. The troughs which occur at approximately 960Hz and 1300Hz correspond to pressure nodes at the microphone measurement positions. It is apparent from the figure that the sound pressure level is typically in excess of 120dB and achieves up to 140dB at certain frequencies. Measurements of the aeroacoustic source strength for a flow through an orifice with such flow rates indicates the sound pressure level remains much lower than this. This data is presented in section 4.5.3.

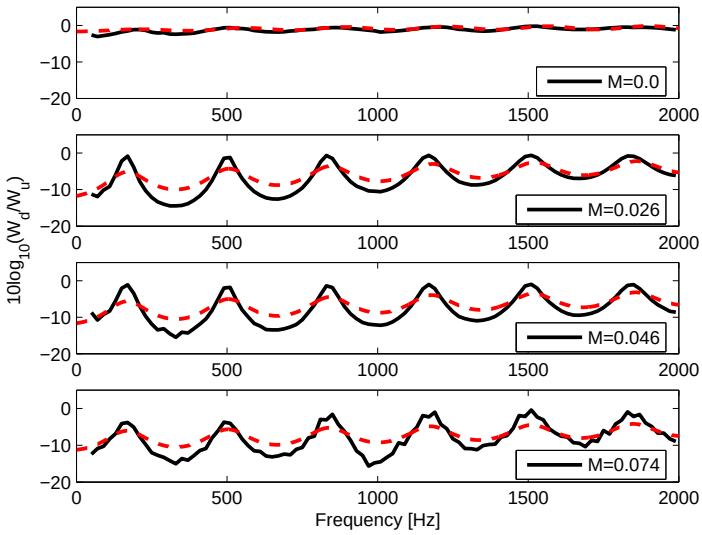

FIGURE 4.8: Ratio of net sound power flux upstream of orifice to that immediately downstream. (-) Experimental result. (- -) Predicted from eqn 4.20.

Figure 4.8 is a plot of the ratio of sound power flux downstream of the orifice to that upstream for a system excited upstream of the orifice via a loudspeaker. The results are for a orifice with an area ratio of 4 for mean duct Mach numbers of 0, 0.026, 0.046 & 0.074. The results are plotted in dB with the solid black line representing the measured value and the red dashed line representing that predicted value from eqn 4.20. It is apparent from the plot that the extent of sound absorption tends toward zero for no flow with a small amount of absorption

due to viscothermal losses. Both the predicted and measured absorption ratio are within 1dB of each other. When flow is present the extent of power loss is much more variable with frequency. Both the theoretical prediction and experimental results have the same spectral shape, however, the extent of the modulation in the predicted curves differs from that of the experimentally determined values by up to 4dB. In addition, both the measured and predicted levels of absorption increases with increasing flow velocity. Further examination indicates that the sound absorption is lowest i.e $10log_{10}W_d/W_u \Rightarrow 0$, at frequencies corresponding to pressure anti-nodes immediately downstream of the orifice and highest corresponding to pressure nodes immediately downstream as indicated by eqn 4.20. Though the prediction and measured results do differ in the extent of modulation with frequency, the dependence of the sound absorption on the local acoustic field is clear.

4.5 Sound generation from an in-duct orifice

The sound generated from flow through an in-duct orifice can be considered similar to that of a spoiler in a duct. Gordon [58, 59] modelled spoiler generated flow noise by relating the total power radiated, W, to the fluctuating drag force on the spoiler. The model assumes that the magnitude of the fluctuating drag forces is proportional to the steady state drag force. The validity of such an assumption was substantiated by good correlation between acoustic power and steady state drag in his results. It was further supported by measurements of Heller and Widnall [82] who found the ratio of the fluctuating overall and steady state drag force to be constant. Gordon's paper [59] provides a prediction for the total acoustic power for a wide variety of spoilers, including that of an orifice, as

$$W = \frac{\kappa(\Delta\bar{P})^3 D^2}{\rho^2 c^3} \tag{4.21}$$

where ΔP is the pressure pressure drop across the spoiler, D is the duct diameter and κ is a constant defined emperically as 2.5×10^{-4}. The geometry of the spoiler does not enter this equation but is implicit in the pressure drop across the flow spoiler.

In this chapter both the scaling laws of Gordon [59] will be compared to aeroacoustic sources measured using the source measurement techniques detailed in Chapter 3. The pressure drop $\Delta\bar{p}$ across the orifice, employed in Gordon's prediction, was determined using the method outlined in appendix A.4.

4.5.1 Measured orifice source power

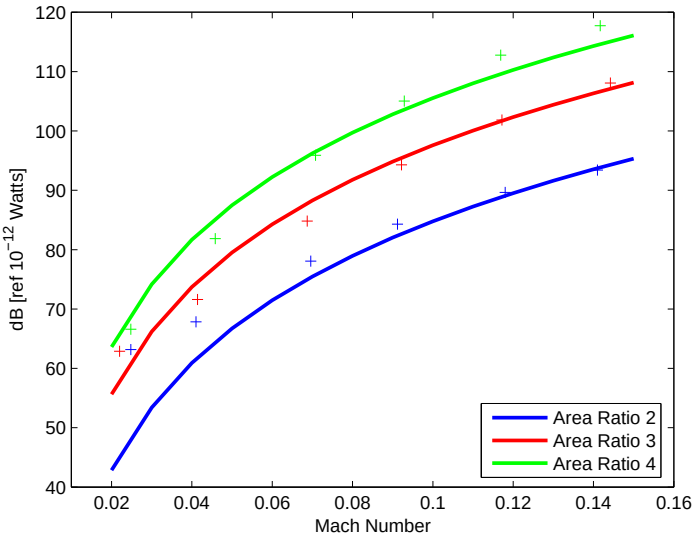

FIGURE 4.9: Total power radiated into farfield (+) from duct termination compared with that predicted (-) by Gordon's equation 4.21 as a function of mean duct Mach number.

Figure 4.9 is a plot of the total orifice source sound power predicted by eqn 4.21 compared with that radiated from the duct termination. The data is plotted for each orifice to duct area ratio. The radiated sound power was determined using a farfield microphone assuming monopole radiation using eqn 3.6. It is apparent from the plots that Gordon's semi-empirical model is valid with the prediction remaining with 3dB of the experimental results apart from a single measurement point for a duct-to-orifice area ratio of 2 with $M \approx 0.25$. This is attributed to the low level of sound generated at this flow velocity causing the signal-to-noise ratio to drop and the error to increase as a consequence.

Figures 4.10, 4.11 & 4.12 show the octave band sound power radiated from the duct termination for an orifice to duct area ratio of 2, 3, & 4 respectively. Examination of the results indicated that the source characteristics of an orifice with an area ratio of 2 have a Strouhal number dependency. Consequently figure 4.10

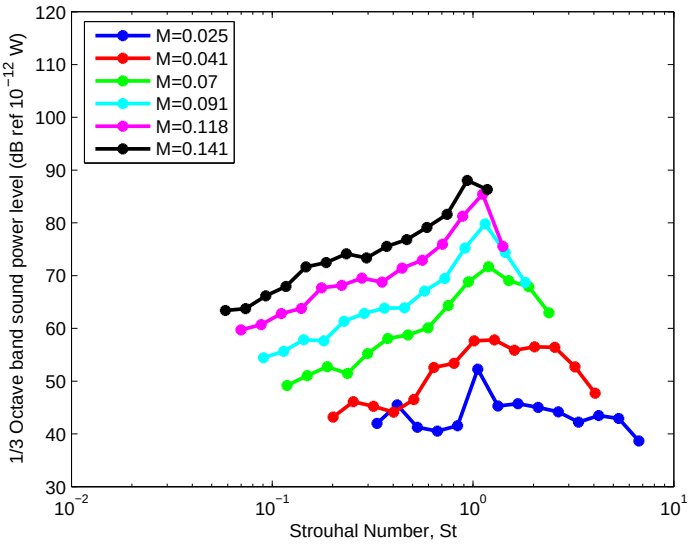

FIGURE 4.10: Octave band sound power radiated from the duct termination for flow through an orifice with an area ratio of 2. Results plotted as a function of Strouhal number.

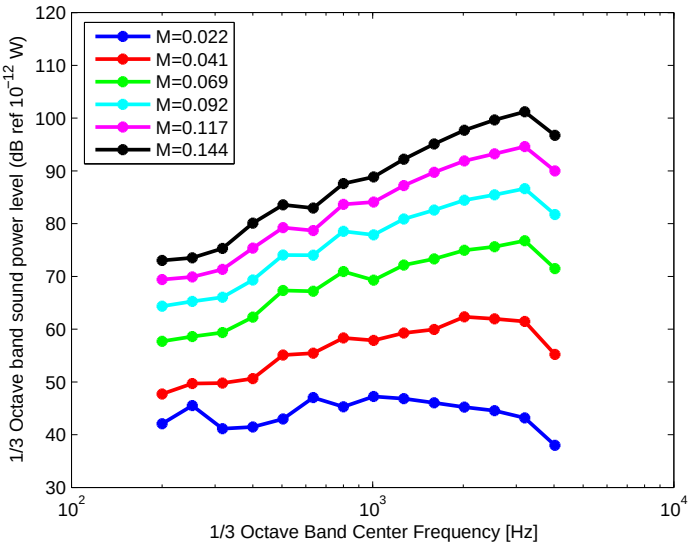

FIGURE 4.11: Octave band sound power radiated from the duct termination for flow through an orifice with an area ratio of 3. Results plotted as a function of 1/3 octave center band frequency.

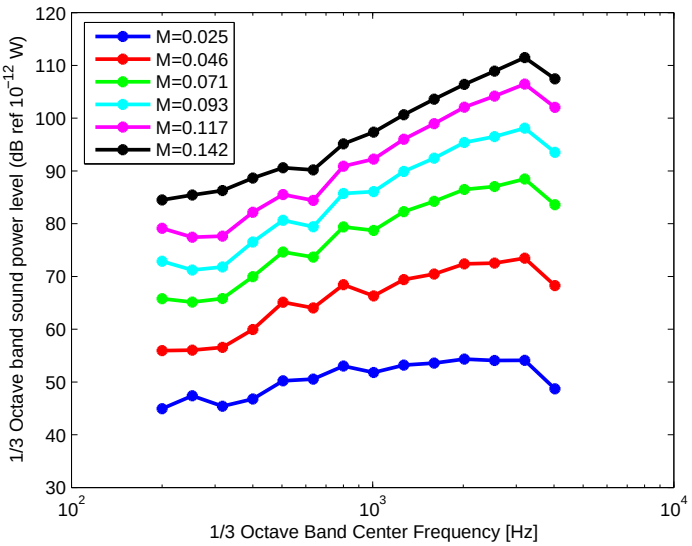

FIGURE 4.12: Octave band sound power radiated from the duct termination for flow through an orifice with an area ratio of 4. Results plotted as a function of 1/3 octave center band frequency.

is plotted as a function of Strouhal number. The plot indicates consistent peak in the spectrum at a Strouhal number of 1.12. This similar to that predicted by Hardin and Pope[55] who predict a peak in the the source spectrum at a Strouhal number of 0.9. In contrast to this, the source characteristics of orifices with an area ratio of 3 & 4 where found to have a Helmholtz number dependency. Consequently figures 4.11 & 4.12 are plotted as a function of 1/3 octave band sound power level. This suggest that the proximity of the duct walls to the developing orifice jet affects the spectral characteristics of the source.

4.5.2 Orifice source velocity dependence

As discussed in section 1.5, the acoustic power radiated by an aeroacoustic source scales as a function of the fluid velocity, U^n, with n expected to vary between 4 & 8. As highlighted by figure 4.10, for an orifice with an area ratio of 2, the source strength is a function of Strouhal number. Assuming that the aeroacoustic source power, W, at one particular flow velocity and Strouhal number can be represented as

$$W_1 = A\bar{U}_1^n, \tag{4.22}$$

and the aeroacoustic source power at another flow velocity can be defined as

$$W_2 = A\bar{U}_2^n, \tag{4.23}$$

where A is some unknown function which includes all other parameters. This implies that

$$A = \frac{W_1}{\bar{U}_1^n} = \frac{W_2}{\bar{U}_2^n}. \tag{4.24}$$

Taking the natural logarithm of both sides and rearranging provides

$$n = \frac{ln\frac{W_1}{W_2}}{ln\frac{\bar{U}_1}{\bar{U}_2}} \tag{4.25}$$

Therefore, with a knowledge of the acoustic power at two or more distinct flow velocities the velocity dependence, n, of the aeroacoustic source associated with flow through an orifice can be determined. The results of this analysis for an orifice with a duct to orifice area ratio of 2 are plotted in figure 4.13. The results where calculated from the 1/3 octave band sound power radiated from the duct termination as shown in figure 4.10. The data was linearly interpolated between data points to compare the sound power at equivalent Strouhal numbers. The average velocity dependence was determine from the five different flow velocity combinations at each Strouhal number apart from at a Strouhal number of 0.1 where three flow velocity combinations, and at a Strouhal number of 2 where two flow velocity combinations where used due to a shortage of data in these regions. The results indicate that the source power on average scales as $U^{5.75}$. The slight increase to $U^{6.2}$ at $Str = 0.1$ and decrease to $U^4.8$ at $Str = 2$ is attributed to an increase in error due to a decrease in data points employ in determining n at these Strouhal number values.

The same technique was performed on the data for sound power radiated from orifices with area ratios of 3 & 4. However, as demonstrated in figures 4.11 & 4.12 of section 4.5.1, the source power is a function of Helmholtz number, ka, rather than Strouhal number for these orifice geometries. Consequently, the velocity dependence of the aeroacoustic source associated with these orifice geometries was determined assuming the source to be a function of flow velocity and Helmholtz number. The results of the analysis is plotted in figure 4.14. The plot indicates that the velocity dependence of the orifice with an area ratio of 3 is approximately U^4 at very low Helmholtz number increasing to $U^{7.43}$ at a Helmholtz number

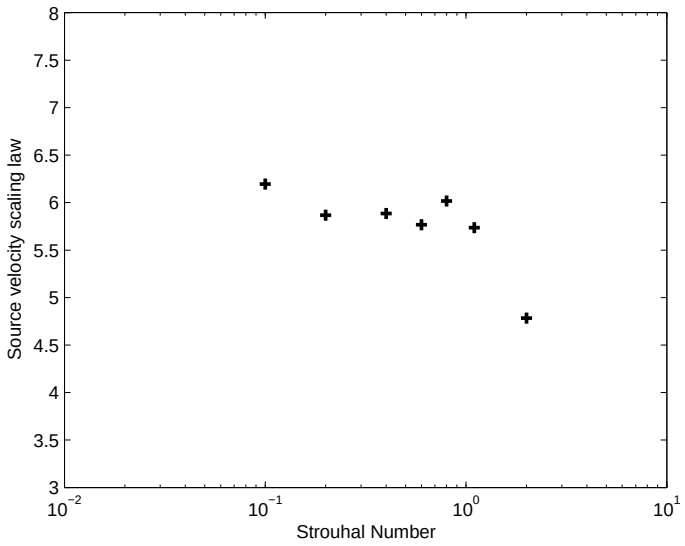

FIGURE 4.13: Velocity dependence, n, of aeroacoustic source power associated with flow through an orifice with an area ratio of 2. Velocity dependence plotted as a function of Strouhal number

of 1.48. Similarly, the velocity dependence of an orifice with an area ratio of 4 is approximately $U^{5.5}$ at very low Helmholtz numbers increasing to $U^{7.78}$ at a Helmholtz number of 1.48. This indicates that as the Helmholtz number increases toward the cut-on frequency of the first higher order mode the source becomes quadrapole (U^8) in nature, whereas at low frequencies it tends toward that of a monopole (U^4) for an orifice with an area ratio of 3, and toward that of a dipole (U^6) for an orifice with an area ratio of 4.

4.5.3 In-duct source measurements

Figures 4.15 - 4.20 are plots of the aeroacoustic source strength due to flow through an orifice in a duct with area ratios of 2, 3, & 4 measured using the technique presented in section 3.5. The source strengths are normalised and plotted in dB. The results are plotted as a function of frequency and mean duct Mach number in both an isometric view and plan view. The plots are created from 6 mean duct Mach numbers and the data interpolated between for visual improvement. Examination of the results highlights key features. Firstly, low source strength values (represented by blue/green) can be observed at approximately 800 Hz, 1250 Hz and 1550Hz on all plots. This is a results of a low signal to noise ratio at these frequencies due to a pressure node occurring at the measurement planes

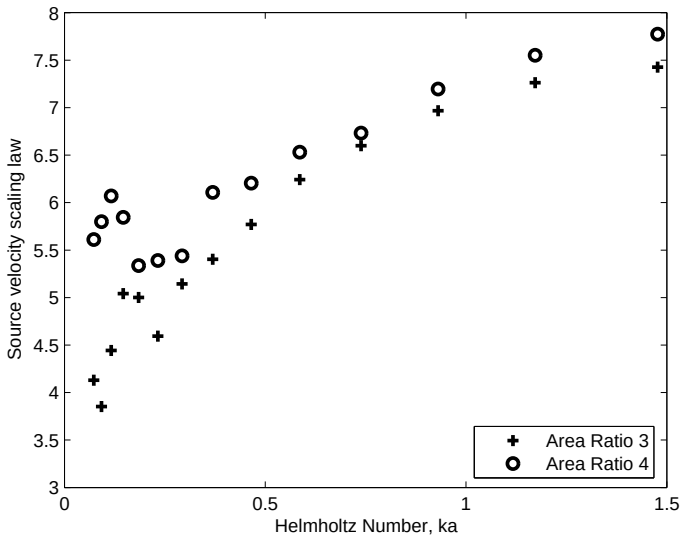

FIGURE 4.14: Velocity dependence, n, of aeroacoustic source power associated with flow through an orifice with an area ratio of 3 & 4. Velocity dependence plotted as a function of Helmholtz number.

of the microphone positions downstream of the orifice. Consequently the source strength presented at these frequencies should be ignored. Secondly, distinct high source strength levels (in red) can be observed at a number of frequencies for all Mach numbers. The frequency at which these high source strengths occur is approximately 496 Hz, 1140 Hz, and 1845 Hz for an orifice with an area ratio of 2, 495 Hz, 867Hz, 1140 Hz and 1462 Hz for area ratio of 3, and 174Hz, 455 Hz, 1156 Hz, 1472Hz and 1800 Hz for an orifice with an area ratio of 4. These frequencies are similar to those correspond to pressure anti-nodes immediately downstream of the orifice. However, these peaks are not apparent in acoustic power radiated from the duct termination. This indicates that these peaks are not associated with the source power radiated in the downstream direction but rather are associated with the acoustic power radiated in the upstream direction from the source. It is concluded from the measurements that acoustic power radiated in the upstream direction from the orifice region has frequencies equal to that of the tailpipe is acting at a quarter wave resonator whereas the spectral characteristics of the source in the downstream direction is more broadband.

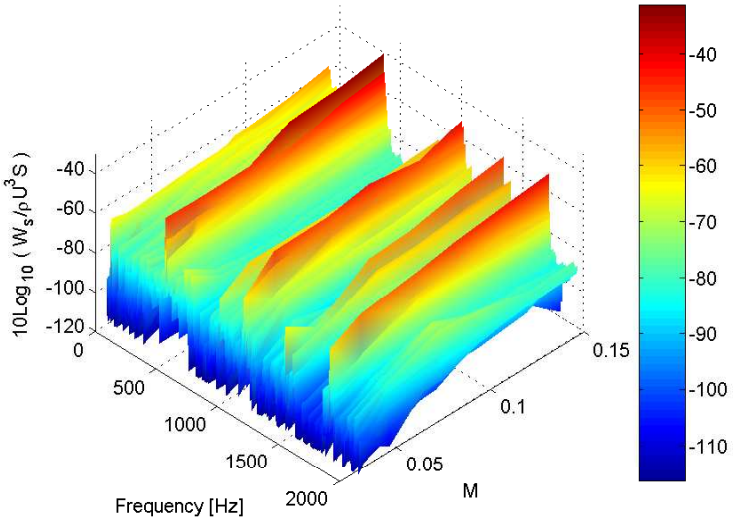

FIGURE 4.15: Isometric view of normalised source strength for flow through an orifice with an orifice to duct cross sectional area ratio of 2 as a function of frequency and mean duct Mach number. Colourbar in dB (ref $\rho U^3 S$).

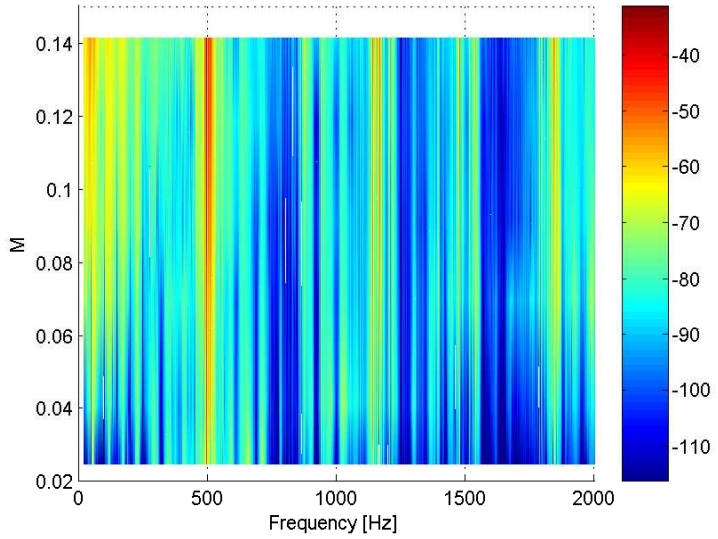

FIGURE 4.16: Plan view of normalised source strength for flow through an orifice with an orifice to duct cross sectional area ratio of 2 as a function of frequency and mean duct Mach number. Colourbar in dB (ref $\rho U^3 S$).

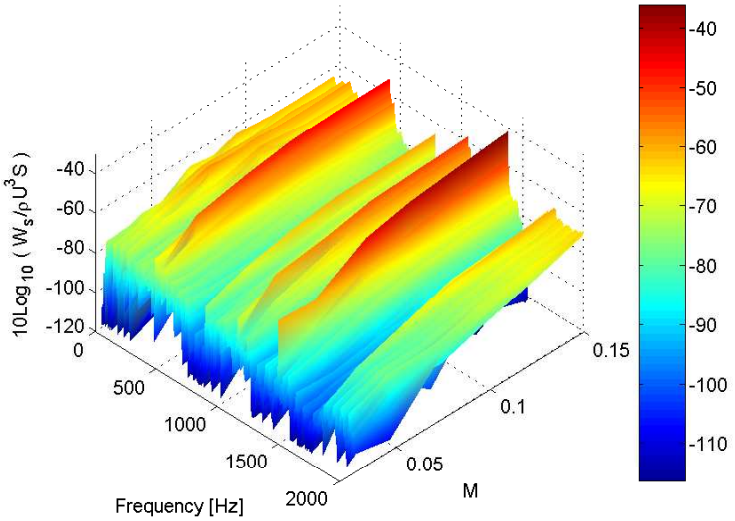

FIGURE 4.17: Isometric view of normalised source strength for flow through an orifice with an orifice to duct cross sectional area ratio of 3 as a function of frequency and mean duct Mach number. Colourbar in dB (ref $\rho U^3 S$).

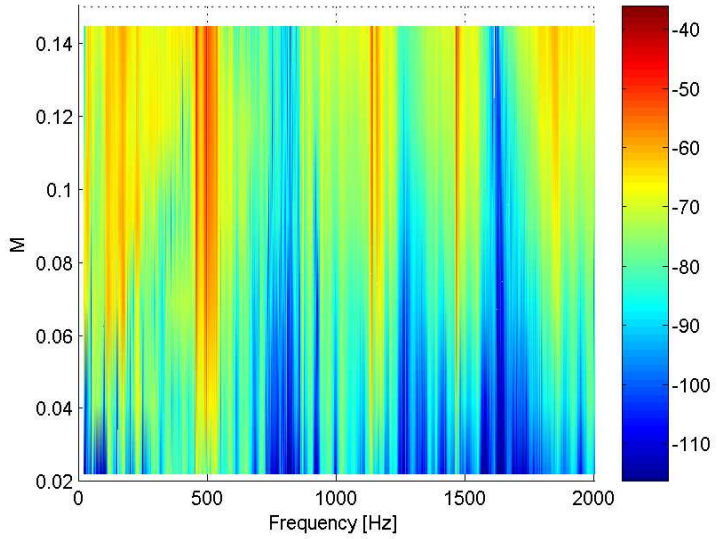

FIGURE 4.18: Plan view of normalised source strength for flow through an orifice with an orifice to duct cross sectional area ratio of 3 as a function of frequency and mean duct Mach number. Colourbar in dB (ref $\rho U^3 S$).

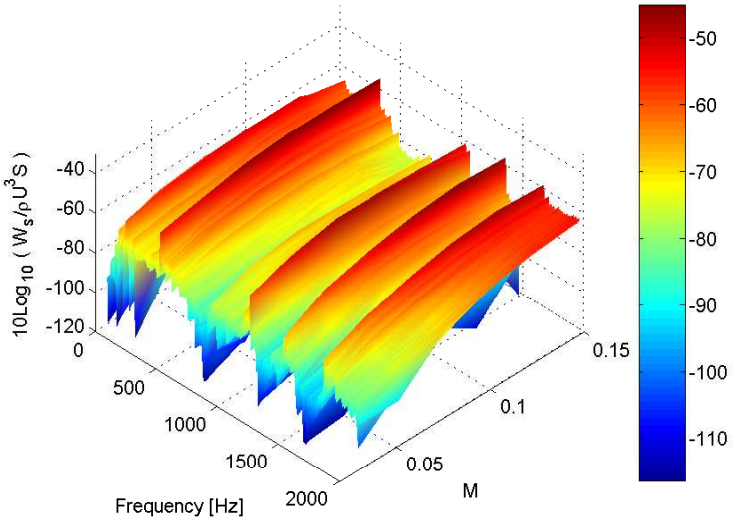

FIGURE 4.19: Isometric view of normalised source strength for flow through an orifice with an orifice to duct cross sectional area ratio of 4 as a function of frequency and mean duct Mach number. Colourbar in dB (ref $\rho U^3 S$).

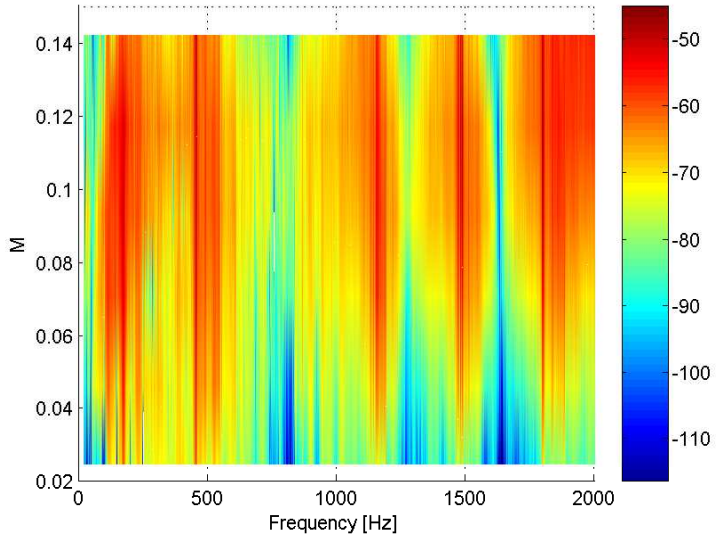

FIGURE 4.20: Plan view of normalised source strength for flow through an orifice with an orifice to duct cross sectional area ratio of 4 as a function of frequency and mean duct Mach number. Colourbar in dB (ref $\rho U^3 S$).

4.6 Conclusions

In this chapter the aeroacoustic of an orifice in a duct with flow have been assessed. An equation for the acoustic power loss at an area expansion in a duct at low with flow has been presented. The equation highlights the importance of the local acoustic field in the absorption of acoustic energy by the shear layer formed at such sudden expansions. The theory was applied to an in-duct orifice with a duct to orifice area ratio of 4 and the predicted absorption compared to that experimentally determined, as presented in section 4.4.1. The results of the comparison indicate that the sound absorption is lowest at frequencies corresponding to pressure anti-nodes immediately downstream of the orifice and highest corresponding to pressure nodes immediately downstream. This supports Howe's power integral [49](eqn 4.1).

Measurements of the acoustic power generated orifices in a duct with area ratios of 2, 3, 4 are presented in section 4.5. Comparison of Gordon's semi-empirical model for sound radiated from an orifice in a duct with measurements indicate the model is valid to within 3dB. In addition, it was discover that the source strength of an orifice with an area ratio of 2 is a function of Strouhal number with a peak in the spectra occurring at a Strouhal number of approximately 1.1, whereas the source strength of an orifice with an area ratio of 3 & 4 have a Helmholtz number dependent source strength. Determination of the velocity dependence indicate further differences in the character of the source strength associated with an orifice area ratio of 2 and that of orifices with an area ratio of 3 & 4. The velocity dependence of an orifice with an area ratio of 2 remains relatively unchanged with Strouhal number averaging at $U^{5.75}$. The velocity dependence of orifice with area ratios of 3 & 4 are Helmholtz number dependent tend toward that of a free field jet, U^8, at close to the cut-on of the first higher order mode. However, this decreases to close to that of a monopole source, U^4, for an area ratio of 3, and decreases to that of a dipole source, U^6, for an area ratio of 4 at low frequencies.

The source measurement technique presented in Chapter 3 has been applied to the three different orifice geometries. These aeroacoustic source strengths are plotted in section 4.5.3 as a function of mean duct Mach number and frequency. Examination of the results indicates that the source is coupling with the tailpipe in such a way as to act as a quarter wave resonator. Further examination of the measurement indicate that these peaks in the source spectra are radiated upstream

of the orifice only, whereas the source power radiated downstream of the orifice is more broadband in character.

Chapter 5

Aeroacoustic sound generation in simple expansion chambers

5.1 Introduction

In chapter 3 a method for the measurement of the strength of aeroacoustic sources in ducts with flow based on acoustic powerflux measurements was developed. This chapter applies the technique to measure the aeroacoustic source strength of a simple flow excited expansion chamber. The chamber source measurements are plotted as a function of chamber inlet mean Mach number and frequency and indicate that acoustic lock-on occurs when the vortex shedding frequency is similar to the tailpipe resonant frequency. A comparison of the lock-on frequencies measured with that predicted by theory is presented in section 5.4.1. The esperimental results support the theory.

5.2 Theory

Experimental results [8, 83] have indicated that flow excited expansion chambers have tonal characteristics with spectral peaks of the radiated acoustic field occuring at acoustic resonant frequencies of the tailpipe and the expansion chamber. Such resonantors can be considered half wave resonators with resonant frequencies, f_r, defined by [8, 84]

$$f_r = \frac{nc(1-M^2)}{2L_{eff}}, n = 1, 2... \tag{5.1}$$

where L_{eff} is the effective length of the resonator. For chamber resonances L_{eff} is equivalent to the chamber length, whereas for the tailpipe of length L_t, $L_{eff} \approx L_t + 0.525D$ where D is the tailpipe diameter [9]. In some cases [63, 64, 85] such sustained oscillations are apparently controlled by eddy shedding at frequencies corresponding acoustic resonances of the adjacent lengths of pipe. The Strouhal number, fL/U_∞, of these tones typically lie within well defined bands when plotted against mean flow Mach number, where U_∞ represent the free stream velocity. For flow in ducts this is the mean stream velocity at the duct centre. These bands can be understood in terms of the 'feedback' system proposed by Rossiter [86] for cavity tones in which the flow seperates at the upstream edge to form a shear layer which quickly rolls up to form a train vortices. These vortices are convected downstream towards the trailing edge of the cavity. As these vortices impinge on the trailing edge of the cavity a sound pulse is generated which propagates upstream and excites the shear layer at the upstream edge reinforcing the vortex shedding. A vortex travels across the cavity of length, L, in time L/U_c, where U_c is the convective velocity, whereas the sound radiates back to the leading edge in time, L/U_c. In the simplest approximation, the returning sound will reinforce the periodic shedding of vorticity provided the following equation is satisfied

$$\frac{L}{U_c} + \frac{L}{c} = \frac{n}{f}, n = 1, 2, 3.. \tag{5.2}$$

Comparison of equation 5.2 with experimental observation [63, 87] lead to n being replace with a constant $n - \beta$ where β which accounts for a 'phase lag' associated with the arrival of the vortex at the trailing edge and the emission of the acoustic pulse, and the arrival of sound at the leading edge and the the release of a new vortex. This leads to

$$\frac{fL}{U_\infty} = \frac{U_c}{U_\infty}(n - \beta) \tag{5.3}$$

with good agreement between prediction and measurement for $U_c/U_\infty \approx 0.6$ and $\beta \approx 0.25$. In a duct the free stream velocity doesn't exist and so U_∞ will be

replaced with the duct centre line velocity U_{peak}. Analysis of the flow profiles detailed in section 2.4.1 indicated $U_{peak} = 1.16\bar{U}$.

5.2.1 Lock-on flow tones

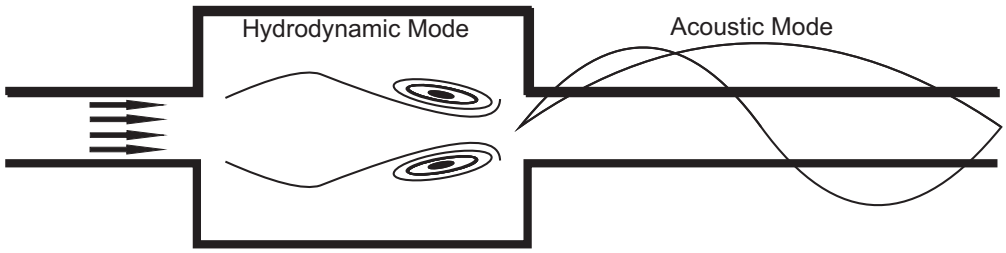

FIGURE 5.1: Schematic demonstrating hydrodynamic and acoustic modes associated with a simple expansion chamber and its associated tailpipe.

Aeroacoustic lock-on occurs when a hydrodymamic mode, such as that associated with vortices shed from the downstream facing egde of the inlet of an expansion chamber, couples with that of of a local acoustic resonances. The result of such aeroacoustic coupling is a highly amplified tone. Insight into lock-on flow tones is provided by Howe's acoustic power integral [49] as dicussed in section 4.2. Crucially, it indicates that energy transfer from the fluid dynamic to the acoustic field occurs when high levels of vorticity occur at a pressure node. With regard to an expansion chamber a pressure node can be expected at the inlet to the tailpipe at frequencies indicate by eqn 5.1 and it is at this point where the vortices interact with the downstream edge of the chamber [56, 84, 88]. Therefore, it is expected for acoustic lock-on to occur when the vortex shedding frequency predicted by eqn 5.3 matches closely the frequency predicted by eqn 5.1.

5.2.2 Describing function theory applied to flow excited resonators

Describing function analysis is a method commonly employed in control theory to calculate the limit cycle of a nonlinear system. Using the method the system of interest is modelled as a group of coupled elements, with each element represented by its associated frequency response functon or decribing function [89]. Typically the the linear part of the system is represented by one decribing function and

the non-linear part of the system represented by another decribing function. Self-excited flow oscillations are common examples of nonlinear systems which possess such limit cycles. Mast and Pierce [67] adopted decribing function theory as a means to model the self excited oscillation of resonators subjected to grazing boundary layer flow. They assume that the resonator can be described as a one-dimensional, lumped element oscillator with governing equation

$$m\ddot{x} + r\dot{x} + Kx = F(x,t). \tag{5.4}$$

Here x is the average displacement of the fluid, m is the relative mass of fluid excited in the resonator, r is the radiation resistance, K is the stiffness of the resonator and $F(x,t)$ is the force exerted on the fluid in the resonator opening.

In their analysis they consider describing functions in terms of the orifice volume velocity, q_o, and resonator volume velocity, q_r. The forward gain function decribes the the non-linear interaction between the oscillatory flow in the resonators neck and the unstable mean flow and is given by $q_o(q_r)/q_r$. The backward gain function is associated with the response of the resonator to a given flow disturbance and is given by $q_r(q_o)/q_o$. The criteria for a limit cycle of the system to exist is that both q_r and q_o must be finite and that

$$\frac{q_o(q_r)}{q_r}\frac{q_r(q_o)}{q_o} = 1 \tag{5.5}$$

Mast and Pierce [67] derive the forward gain function as

$$\left(\frac{q_o}{q_r}\right)_{forward} = \frac{0.5A^3\rho U^2}{\omega m\,|q_r|}e^{-j(3\pi/2-2\omega d/u)} \tag{5.6}$$

where A is the surface area over which the oscillatory flow acts, d is the length over which a hydrodynamic mode developes. The respective backward gain function is provided as

$$\left(\frac{q_r}{q_o}\right)_{backward} = \frac{1 - j\Omega/Q}{\Omega^2 - (1 - j * \Omega/Q)} \tag{5.7}$$

where Q is the quality factor of the resonator defined as $\sqrt{Km}/r$, $\Omega = \omega/\omega_o$, and $\omega_o = \sqrt{K/m}$ is the natural frequency of the resonator.

These two equations can be solved numerically to yield possible solutions for stable conditions. This criteria can be written as

$$\frac{0.5A^3\rho U^2}{\omega m\left|q_r\right|}e^{-j(3\pi/2-2S)}\frac{1-j\Omega/Q}{\Omega^2-(1-j*\Omega/Q)}=1 \tag{5.8}$$

where $S = \omega d/U$ is the Strouhal number. Eqn 5.8 can only be solved if the imaginary part of the loop gain is zero. From this assumption it can shown that the frequency of flow excited oscillations is defined as

$$\omega=\frac{U}{2d}tan^{-1}\left(\frac{Q^2-\Omega^2\left(Q^2-1\right)}{\Omega^3Q}\right)+n\pi. \tag{5.9}$$

To apply this theory to a flow excited expansion chamber the tailpipe is consider to be the resonator excited with an effective mass, m, of $\rho L_{eff}S_t$, where S_t is the cross-sectional area of the tailpipe. The natural frequency of the tailpipe is defined by eqn 5.1 which allows for the stiffness to be calculated from $K = m(2\pi f_r)^2$. The radiation resistance of associated with the source is defined by considering it analagous to oscillating piston in a cavity in a duct [90, 91]

$$r=\pi L^2\rho c\frac{sin^2\theta_o}{\theta_o}, \tag{5.10}$$

where $\theta_o = \omega L/2c$. With a knowledge of m, K, and r and by specifying a value of u and n, Eqn 5.9 can be solved numerically for ω. The predicted value of omega will be compared with experimental results in section 5.4.1.

5.3 Experimental method

Figure 5.2 is a schematic of the experimental set-up employed to measure the aeroacoustic source strength in a simple expansion chamber for a range of flow velocities. The expansion chamber was located in the anechoic chamber of the ISVR Doak Lab. The inlet duct was connected to the ISVR high pressure air supply detailed in Figure 2.5. Pairs of microphones were mounted flush with the inner wall of the duct both upstream and downstream of the expansion chamber. An additional microphone was position in the farfield at 60° to the duct center axis at a radius of 500mm from the duct termination.

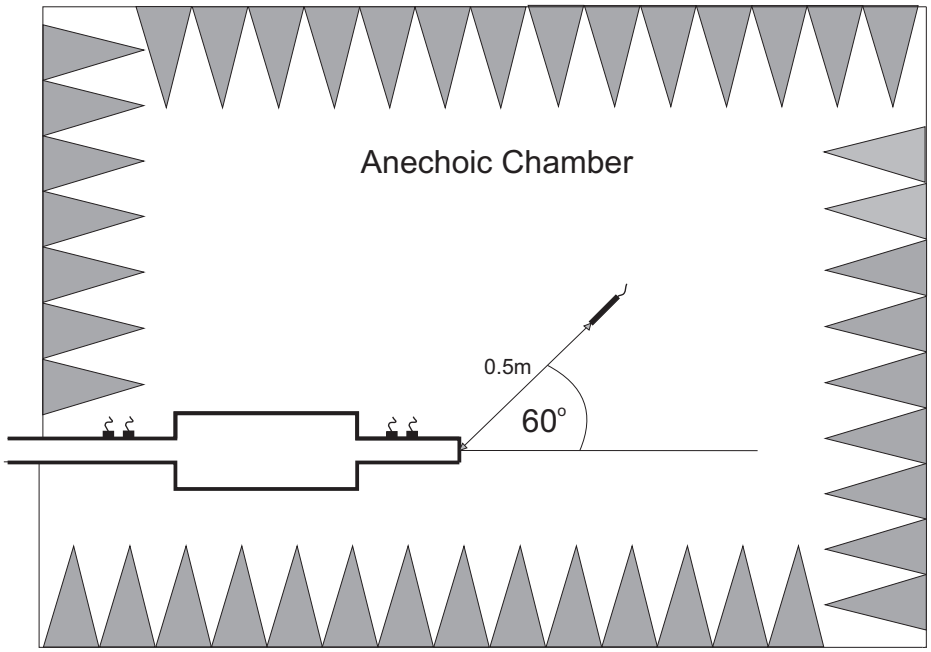

FIGURE 5.2: Overview of chamber geometry and experimental configuration.

5.3.1 Expansion chamber configuration

Figure 5.3 consists of a hard plastic inlet and outlet ducts with an internal diameter of 39mm and 2mm wall thickness. The chamber duct has an internal diameter of 107mm and a wall thickness of 4mm. The chamber ends consist of 24mm thick plywood. A sliding interface exist between the downstream plywood end and the chamber duct to allow for the chamber length to be modified. The temperature of the air was measured using a duct wall mounted thermocouple located 175mm upstream of the expansion chamber entrance.

5.3.2 Measurements

Simultaneous pressure time series were acquired using a National Instrument PXI-4472 8 Channel acquisition cards. Meausurements were taken when the system was excited acoustically via a loudspeaker connected upstream (see figure 2.5) to allow for relative phase and magnitude calibration of the microphones as detailed in section 2.3.3. Measurements were taken when the system was excited by just flow for chamber lengths from 2D to 10D with 1D increments, with 6 inlet duct Mach Numbers increasing in approximately equal increments from approximatelty 0.03 - 0.2. A sampling rate of 44.1 kHz and an acquisition time of 60 seconds

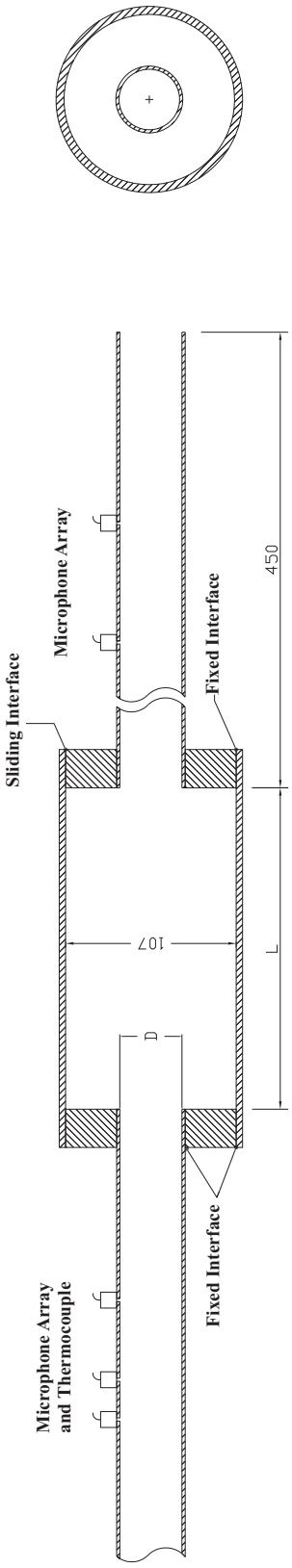

FIGURE 5.3: Schematic detailing geometry of expansion chamber used in experiments.

was used for each test. A 32768 FFT length with a 50% overlap and hanning window was employed to process the results using specifically written MATLAB code. This provided 80 spectral averages and a spectral binwidth of 1.346Hz. The acoustic source strength was calculated from measuring the acoustic power flux both upstream and downstream of the expansion chamber as detailed in chapter 3.

5.4 Results

Figures 5.4 - 5.11 plot the source strength due to flow through a simple expansion chamber of length 2D -5D. The results are presented as spectrograms of acoustic power normalised with $\rho U^3 S$ [80]. A linear interpolation between measured values has been employed to refine the plots. The source strength of each chamber configuration is displayed in isometric and plan views with the plan views containing dotted lines to indicate the tailpipe resonant frequencies predicted by eqn 5.1. The magnitude of the normalised source strengths is defined by a colourbar with dark red indicated the highest magnitude and dark blue indicating the lowest values.

A number of key features can be observed from the plots. Distinctive bands of higher source strength occur a multiples of approximately 360Hz. Analysis of figure 5.5 suggest that these bands correspond to the tailpipe resonant frequencies indicated by the dotted lines on the plot. In addition to this, a number of distinct peaks in the source magnitude can be observed on each of the spectrograms. For an expansion chamber of length 2D the most dominant of these can be observed in figure 5.4 at frequency of 379Hz, 748Hz & 1075 Hz for respective mean flow Mach numbers of 0.063, 0.1332 & 0.1991. Similar peaks can be observed in figures 5.6-5.11 for different frequency and Mach number combinations for other chamber. These distinct peaks do not necessarily increase with increasing flow velocity but rather appear then disappear as the flow velocity is increase. This suggest that this tones are associated with aeroacoustic lock-on of hydrodynamic modes in the chamber with the acoustic resonances of the tailpipe.

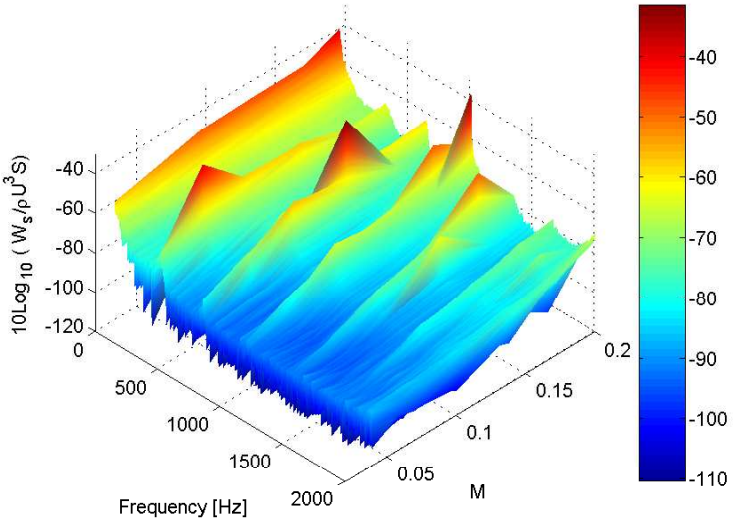

FIGURE 5.4: Isometric view of normalised source strength for a chamber of length 2D as a function of frequency and mean tailpipe Mach number.

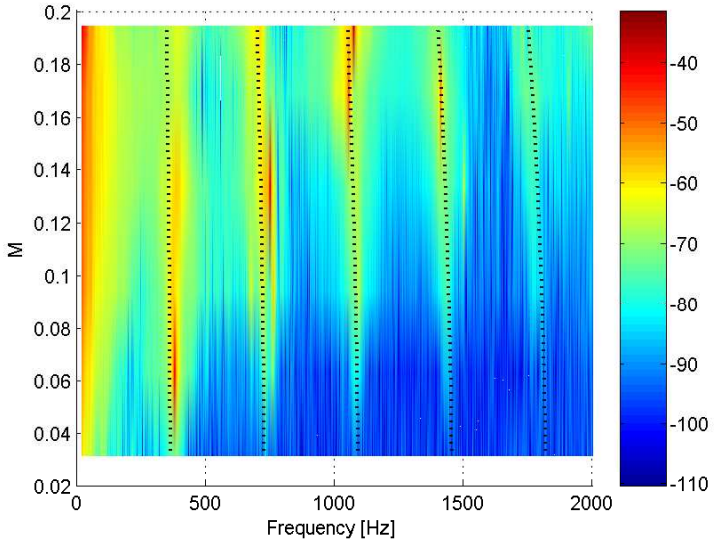

FIGURE 5.5: Plan view of normalised source strength for a chamber of length 2D as a function of frequency and mean tailpipe Mach number. (..) Predicted tailpipe resonant frequency 5.1.

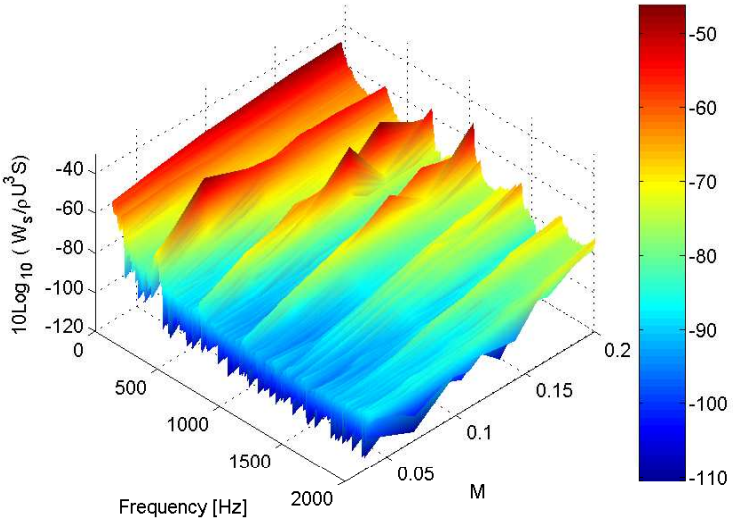

FIGURE 5.6: Isometric view of normalised source strength for a chamber of length 3D as a function of frequency and mean tailpipe Mach number.

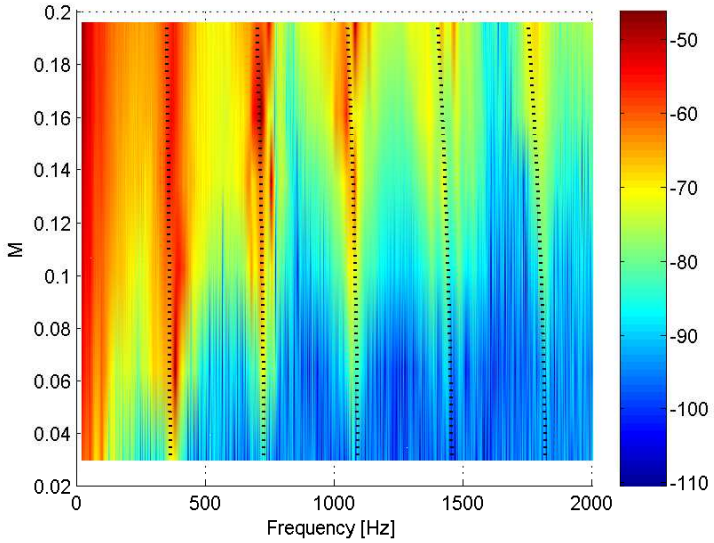

FIGURE 5.7: Plan view of normalised source strength for a chamber of length 3D as a function of frequency and mean tailpipe Mach number. (..) Predicted tailpipe resonant frequency 5.1.

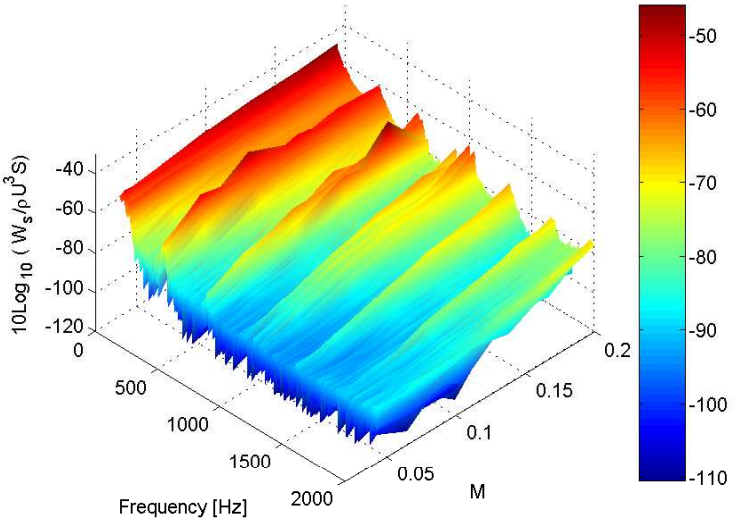

FIGURE 5.8: Isometric view of normalised source strength for a chamber of length 4D as a function of frequency and mean tailpipe Mach number.

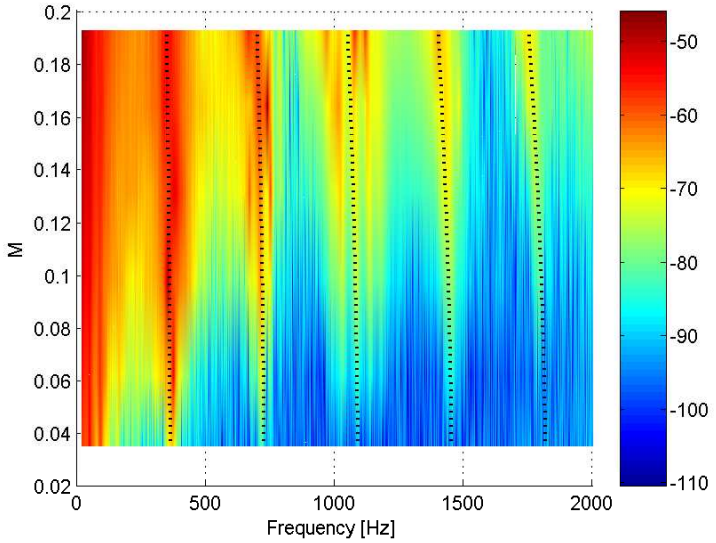

FIGURE 5.9: Plan view of normalised source strength for a chamber of length 4D as a function of frequency and mean tailpipe Mach number. (..) Predicted tailpipe resonant frequency 5.1.

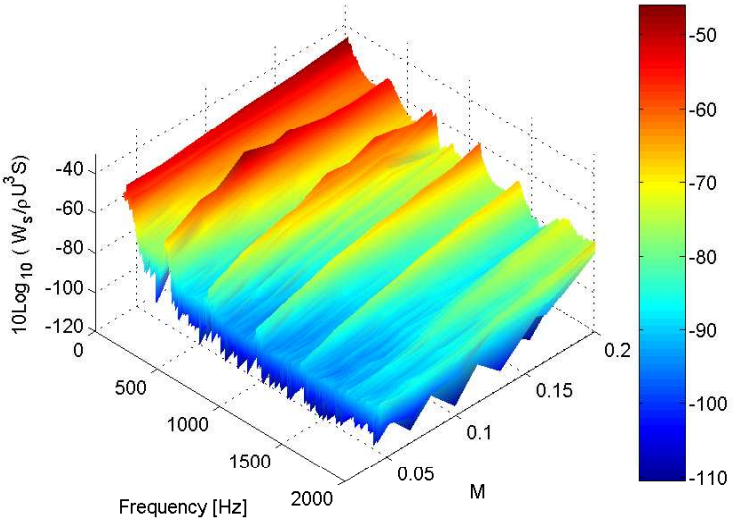

FIGURE 5.10: Isometric view of normalised source strength for a chamber of length 5D as a function of frequency and mean tailpipe Mach number.

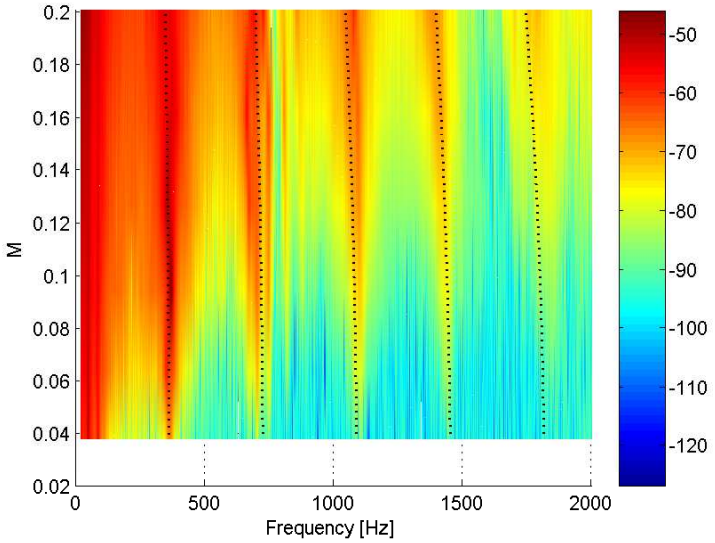

FIGURE 5.11: Plan view of normalised source strength for a chamber of length 5D as a function of frequency and mean tailpipe Mach number. (..) Predicted tailpipe resonant frequency 5.1.

5.4.1 Comparison of flow tones with describing function theory prediction

This section compares the frequency of the lock-on flow tones apparent in the experimental results shown in section 5.4 with that predicted using describing function theory discussed section 5.2.2. Figure 5.12 is a comparison of the frequency of oscillation of the chamber-tailpipe resonator predicted using describing function analysis with that identified from the experimental results for a chamber of length 2D. The freqeuncies are identfied from the experimental results by their distinct peaks in the spectrum which may decrease in magnitude with increasing flow velocity. Each solid line is the frequency of the oscillation predicted by describing function analysis as a function of mean chamber inlet velocity compared and the individual points are the lock-on frequencies identified from results in section 5.4. The frequency of oscillation for each hydrodynamic mode number, n, is plotted. It is apparent from the plots that the predicted frequency follows a similar trend to that of the experimental data with further analysis indicating that predicted frequency is on average 1.4% higher than that measured varying from -7.95% to 7.79%. Figures 5.13 - 5.15 show similar comparisons for expansion chmabers of length 3D, 4D & 5D with the predicted frequency on average 2.07% & 2.45% higher and 0.7% lower than that of that measured respectively. The predicted frequency for each of this chamber lengths varies between -1.93% & 8.38%, -9.26% & 21.74% and -9.7% & 9.34% from that measured for chamber lengths 3D, 4D & 5D respectively. The close match of the theory with experimental results supports describing function theory as a method of modelling the aeroacoustics of flow excited expansion chambers.

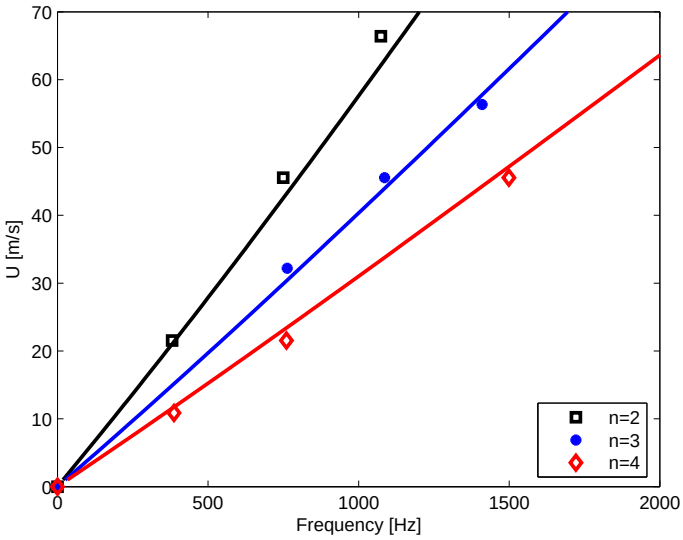

FIGURE 5.12: Comparison of frequency of oscillation of resonator predicted using describing function analysis (-) with that identified from results for a chamber of length 2D. n = hydrodynamic mode number.

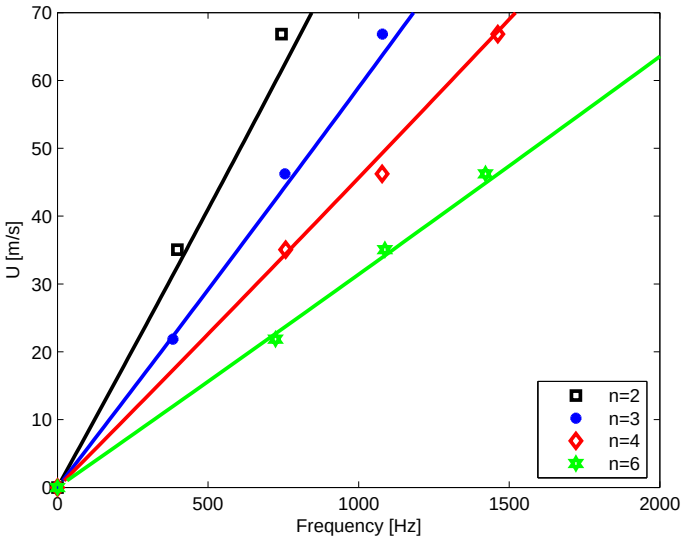

FIGURE 5.13: Comparison of frequency of oscillation of resonator predicted using describing function analysis (-) with that identified from results for a chamber of length 3D. n = hydrodynamic mode number.

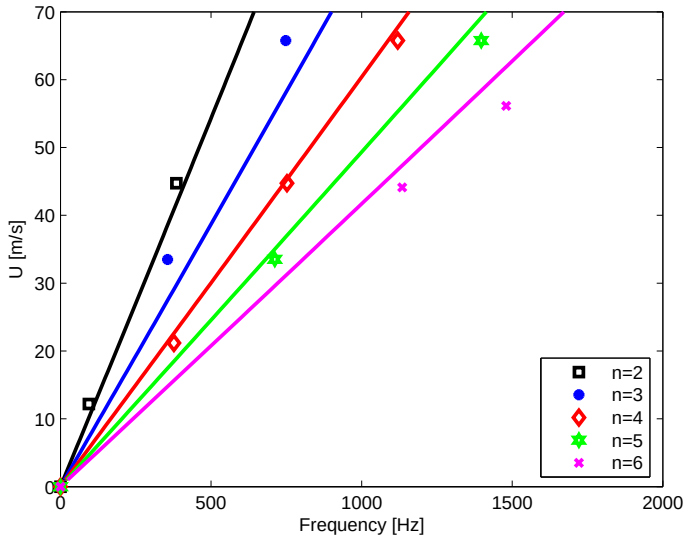

FIGURE 5.14: Comparison of frequency of oscillation of resonator predicted using describing function analysis (-) with that identified from results for a chamber of length 4D. n = hydrodynamic mode number.

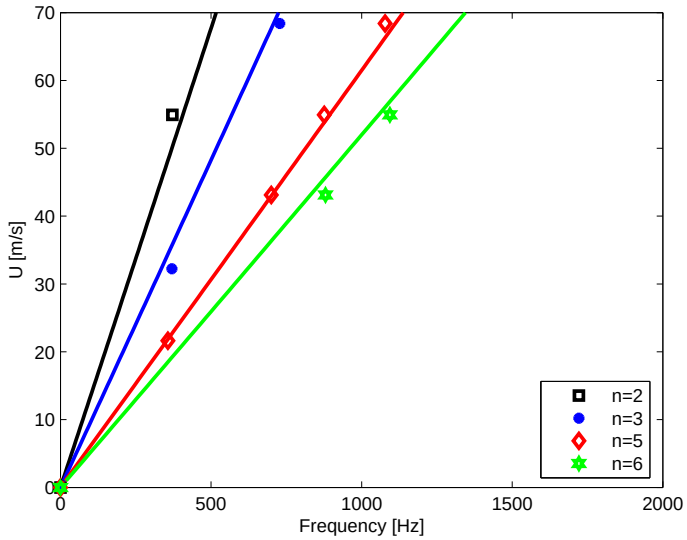

FIGURE 5.15: Comparison of frequency of oscillation of resonator predicted using describing function analysis (-) with that identified from results for a chamber of length 5D. n = hydrodynamic mode number.

5.4.2 Comparison of lock-on flow tones using a simple predictive method

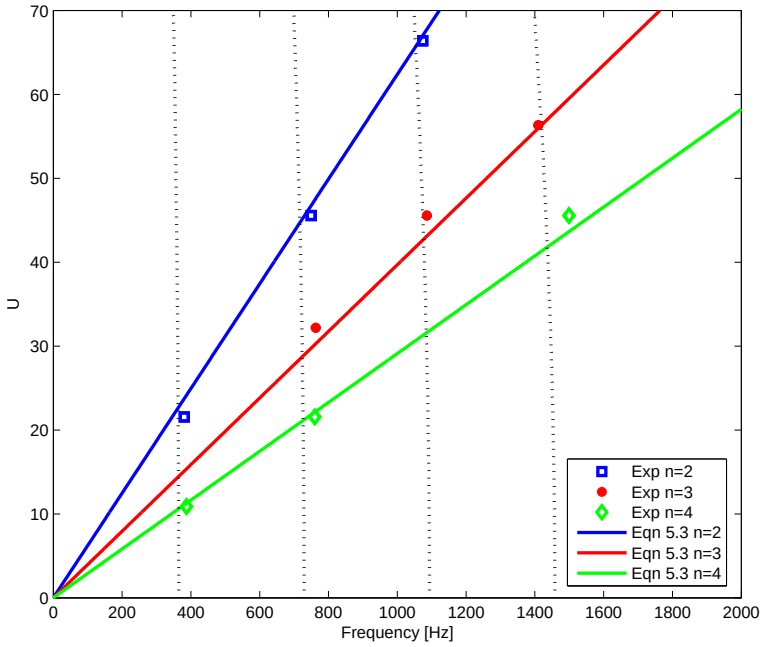

FIGURE 5.16: Comparison of predicted chamber hydrodynamic mode frequencies, predicted tailpipe resonant frequencies (..), and measured lock-on flow tones as a function of mean chamber inlet flow velocity.

Good agreement can be found with the measured locked-on flow tones when the tailpipe resonant frequency predicted by eqn 5.1 satisfies eqn 5.3. Figure 5.16 is a comparison of the chamber hydrodynamic mode frequencies predicted using eqn 5.3 and the tailpipe resonant frequencies predicted using eqn 5.1 with the measured lock-on flow tones as a function of mean chamber inlet flow velocity for a chamber of length 2D. Using the results an improved fit was found if $U_c = 0.616U_{peak}$ was employed in eqn 5.3. Further analysis of the results indicates that the acoustic natural frequencies of the tailpipe predicted by eqn 5.1 are on within -4.9% and +1.2%, and on average 4% below those measured for lock on. Similarly, comparison of the frequencies predicted by eqn 5.3 with those measured indicate the prediction is on average within 1% of those measured with a variance between -23.1% & +11%. The close match of the predictions with the measured results suggests that using eqn 5.3 in conjunction with 5.3 can provide a simple method of assessing whether flow-acoustic lock-on may occur. This method holds an advantage over desribing function theory in the simplicity of the mathematics

involved. In addition, should the geometry of the system be more complex than a simple expansion chamber eqn 5.1 can be replaced with frequencies predicted by acoustic modelling software, such as APEX, already employed in industry.

5.5 Conclusions

In this chapter describing function theory has been used to model the self-excited flow oscillations which occur in simple expansion chambers. The theory was used to predict the frequency of oscillation associated with the tailpipe resonance coupling with the vortices shed in the chamber. In addition, the source strength measurement technique developed in Chapter 3 has been applied to a simple flow excited expansion chamber of different chamber lengths. The results highlight that the frequency of the source tends to be associated with the tailpipe resonant frequency. In addition, distinct peaks in the source strength are apparent when the vortex shedding frequency is similar with that of the tailpipe resonant frequency. This is indicative of acoustic lock-on. Comparison of the frequency of oscillation predicted by the describing function analysis with that measured show the theory match the results within a range of -9.7% and 21.74%. This supports the theory as a method capable of modelling such flow excited resonators. Significantly, comparison of the frequencies at which the tailpipe resonant frequency predicted by eqn 5.1 satisfies eqn 5.3 are on average within 1% of the measured lock-on flow tones within a range of -23.1% & +11%. This suggests that using eqn 5.3 in conjunction with 5.3 can provide a simple method of assessing whether flow-acoustic lock-on may occur. This method holds an advantage over desribing function theory in the simplicity of the mathematics involved.

Chapter 6

Conclusions and Further Work

6.1 Conclusions

This research thesis primarily involved the measurement of certain aeroacoustic characteristics in ducts at low frequencies with steady flow as well as the measurement of the aeroacoustic source strength associated with flow through some common duct geometries. The objective was to use such measurement results to acquire further insight into the effect of flow on such characteristics and establish detail descriptions of the aeroacoustic sources determined.

Novel experimental techniques developed during the course of research include:

- A method for determining the viscothermal attenuation coefficient with flow. The technique is based on simultaneous measurements of pressure times series using two pairs of wall mounted microphones and incorporates Dokumaci's [13] formulation for the flow modified propagation constants. Comparison of the results with Howe's [19] prediction confirm the validity of the technique.

- A method for measurement of the aeroacoustic source strength in ducts with flow. The method is based on coherent powerflux measurements either side of the source region and is restricted to Helmholtz numbers $ka \leq 1.84(1 - M^2)$ where the wave motion can be consider substantially one dimensional. The method is experimentally verified by creating a known source in a duct at a range of frequencies and magnitudes.

An extensive amount of experimental data was acquired as a result of the research period. Significant measurements determined include:

- Measurements of the pressure reflection coefficient for an unflanged duct with outflow for two different edge conditions are presented in chapter 2. The results indicate that the edge thickness of the duct has an effect on the magnitude of the reflection coefficient. Further analysis and comparison with theory suggest that this is related to the extent of vorticity shed from the duct termination, and that the extent of the vorticity shed is affected by the edge condition. The results are used in conjunction with a numerical model developed by Gabard [1] to estimate the extent of vorticity shed from each of the edge conditions.

- The acoustic end correction of an unflanged are presented for two different edge conditions in section 2.8. The results indicate that the end correction tends toward a low frequency of $0.65a$ rather than the $0.6133a$ predicted by Levine and Schwinger [2]. As a consequence Dalmonts expression for the end correction of a circular duct with finite wall thickness is approximately 6% to low. When mean outflow is present the measured end correction tends toward a low frequency limit of $0.19a$ rather than $0.2554a$ as predicted by Rienstra [5].

- Aeroacoustic source measurements from flow through an in-duct orifice with duct-to-orifice area ratios 2, 3 & 4 are presented in chapter 4. The results highlight the importance of the duct-to-orifice area ratio in both the spectral character and velocity dependence of the source. For a orifice with an area ratio of 2 the source appears to have a Strouhal number dependence with a peak magnitude occurring at $Str \approx 1.1$. The magnitude of this Strouhal number dependent source was found to scale with a velocity dependence $U^{5.75}$. The aeroacoustic source strength associated associated with flow through orifices with area ratios 3 & 4 exhibit Helmholtz number dependence. The velocity dependence of the source associated with an orifice of area ratio 3 increases from U^4 at low Helmholtz numbers to $U^{7.43}$ at the cut-on frequency of the first higher order mode. Similarly, the velocity dependence of the source associated with an orifice of area ratio 3 increases from $U^{5.5}$ at low Helmholtz numbers to $U^{7.78}$ at the cut-on frequency of the

first higher order mode. Narrow band source measurements determined using the coherent power flux source measurement method indicate that the the total orifice source power is at a maximum at frequencies corresponding to pressure anti-nodes at immediately downstream of the orifice.

- Aeroacoustic source strength associated with a flow excited expansion chamber are presented in chapter 5. The source strengths are determined for a range of chamber lengths and indicate that the tailpipe acts as the primary resonator of the system. In additions, the results exhibit distinct peaks associated with lock-on flow tones at frequencies when the vortex shedding frequency in the chamber match the acoustic resonant frequency of the tailpipe. Such results support Howe's acoustic power integral.

From the body of work it can be concluded that the source measurement technique based on coherent acoustic power flux measurements either side of a source region is a valid and applicable to aeroacoustic source measurements in ducts with flow at low frequencies. From the body of analysed data the role of vorticity and its interaction with the local acoustic field has been repeatedly highlighted. It is vorticity which seems to be the primary factor which modifies the spectral shape of the pressure reflection coefficient of an unflanged duct with flow. It is vorticity which is apparently responsible for the extensive absorption of the acoustic power radiated from an unflanged duct with flow at low frequencies. With regard aeroacoustic sources, Howe's acoustic power integral indicates that the sound generation is highest when high levels of vorticity couples with the kinetic part of the local acoustic field. Measurements of the aeroacoustic source in a simple expansion chamber support Howe's theory. Therefore, though it may be possible to predict the total acoustic source power with relatively simple models such as that of Gordons for flow through an orifice in a duct, narrow band source prediction requires for detail of the local acoustic field to be included. An example of such a source prediction method is that of describing function theory described in section 5.2.2 which was used to successfully model the frequency of acoustic lock-on of a flow excited expansion chamber. However, a more simple approach of assessing whether flow-acoustic lock-on may occur is possible if eqn 5.3 is used in conjunction with eqn 5.1. In addition should the geometry of the system be more complex than a simple expansion chamber eqn 5.1 can be replaced with frequencies predicted by acoustic modeling software, such as APEX, already employed in industry.

6.1.1 Recommendation of future work

As part of the research presented in this thesis a source measurement technique based on acoustic power flux measurements in ducts with flow has been successfully applied to two generic duct geometries (i) the in-duct orifice (ii) the simple expansion chamber. Future work could include the application of the technique to other common duct geometries such as valves and perforated plates to provide detail of their aeroacoustic sources. Additionally,the aeroacoustic sound generation of more complex expansion chambers, such as that with extended inlet and outlet ducts, could be assess.

In this thesis describing function analysis was used to model the frequency of self-sustained oscillations of a simple expansion chamber. There is potential for this method to model the magnitude of the aeroacoustic source generated in the flow excited expansion chamber in addition to the frequencies predicted in chapter 5. Such predictions could then be refined using the aeroacoustic source measurement results provided in chapter 5.

Appendix A

A.1 Microphone Relative Calibration Functions

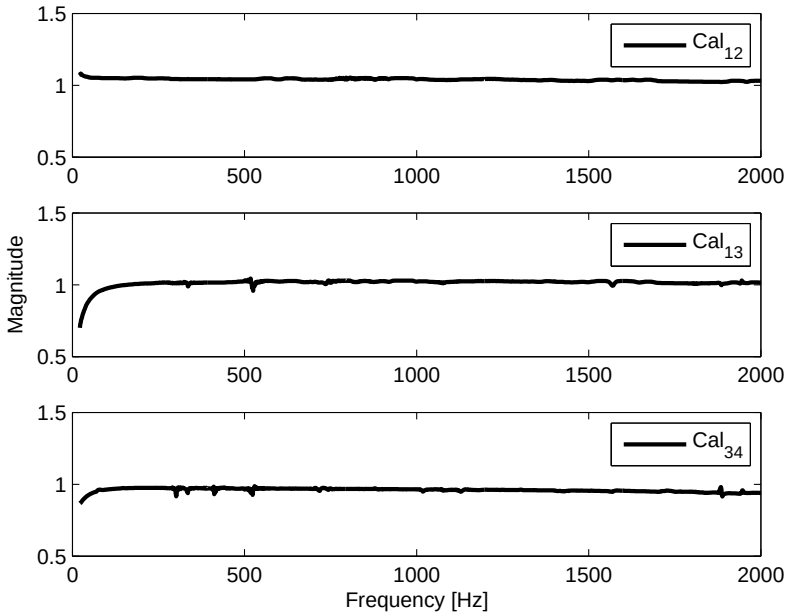

FIGURE A.1: Calibration function magnitude of microphone pairs determined using in-situ sensor switching technique.

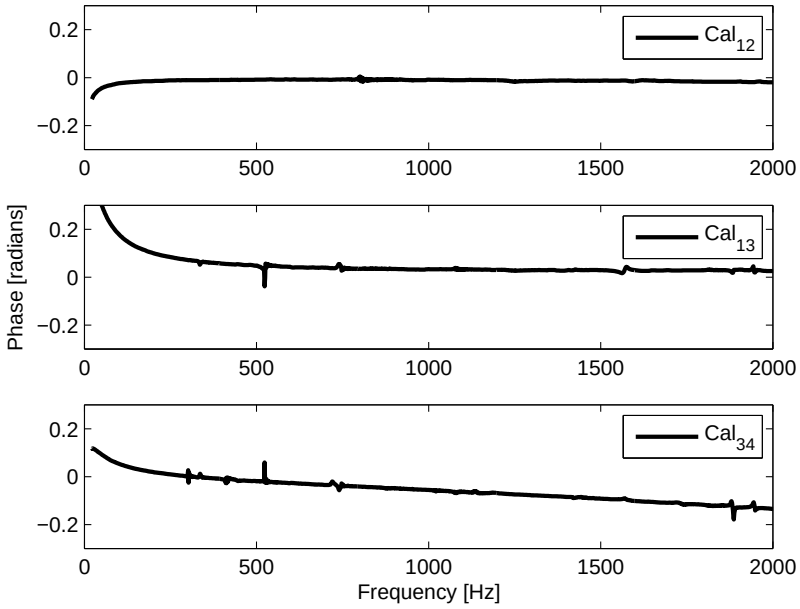

FIGURE A.2: Calibration function phase of microphone pairs determined using in-situ sensor switching technique.

A.2 Estimated Error

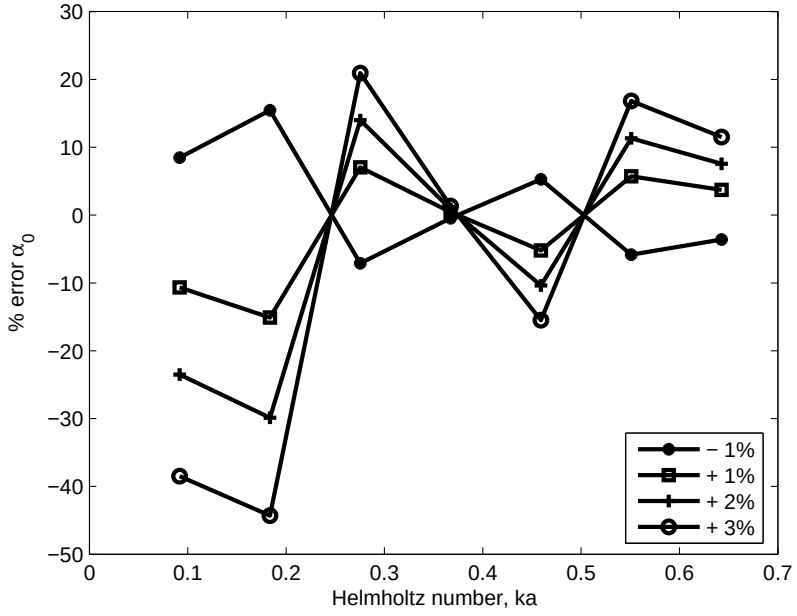

FIGURE A.3: Estimated error in measurement of α_0 for a given percentage error in transfer functions.

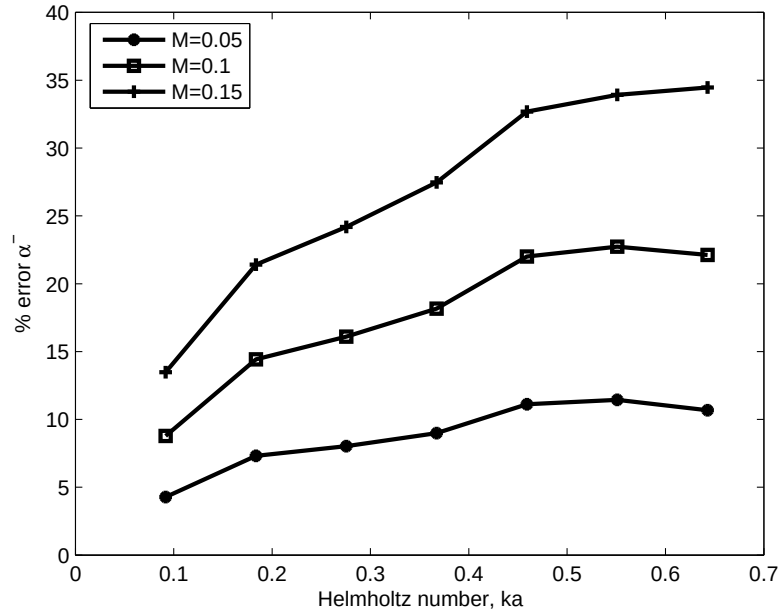

FIGURE A.4: Estimated error in measurement of α^- for a given percentage error in Mach number

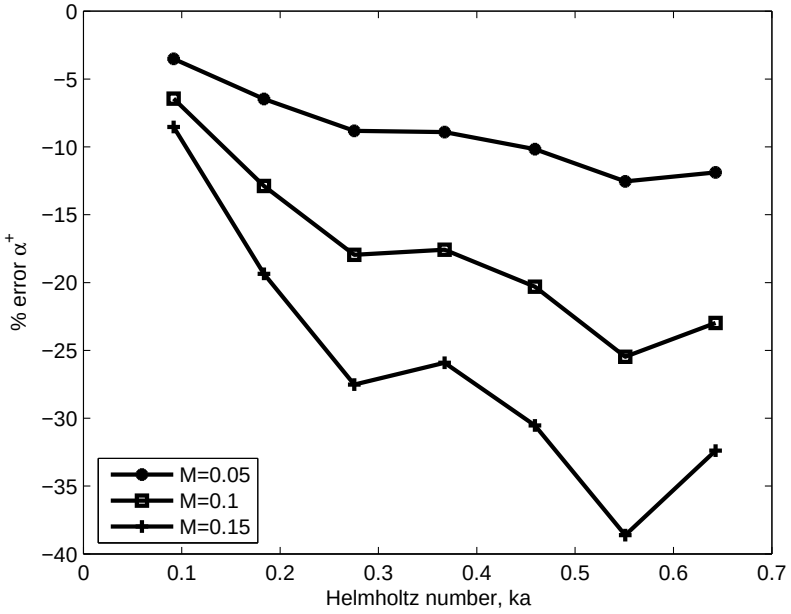

FIGURE A.5: Estimated error in measurement of α^+ for a given percentage error in Mach number.

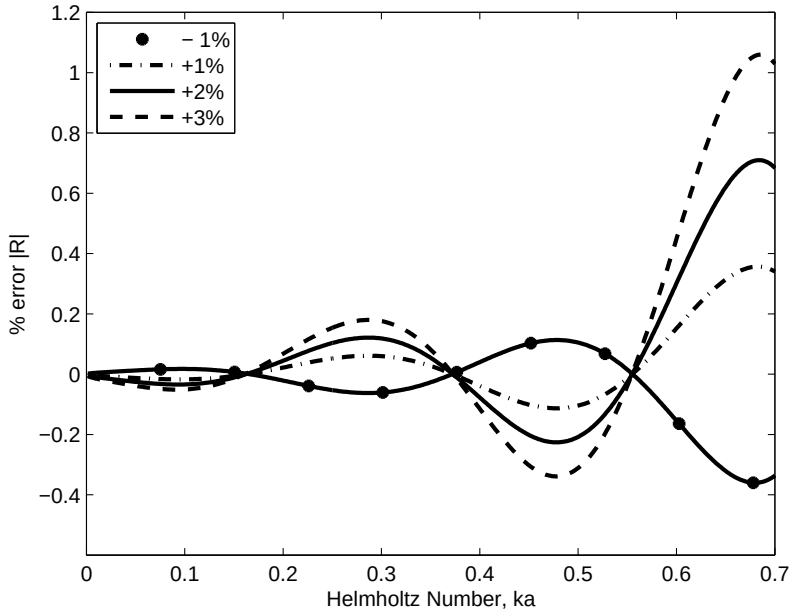

FIGURE A.6: Estimated error in measurement of $|R|$ for a given percentage error in transfer function.

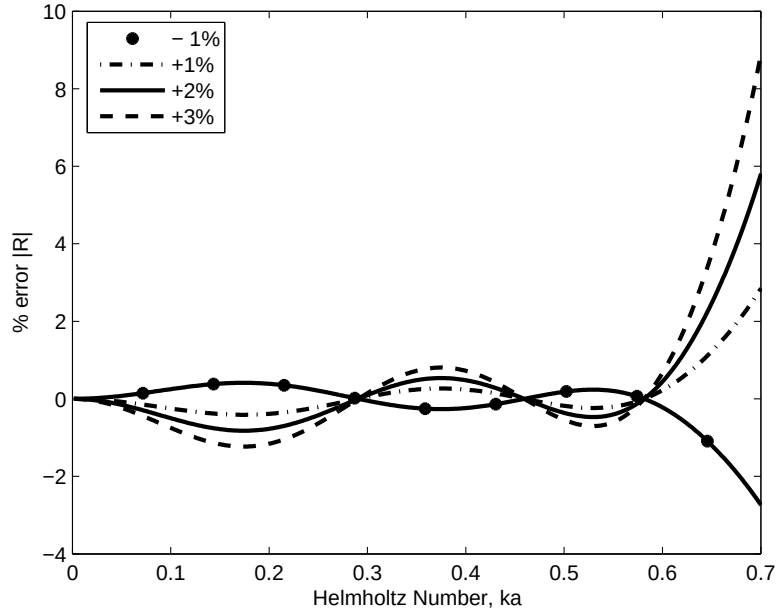

FIGURE A.7: Estimated error in measurement of $|R|$ for a given percentage error in Mach number.

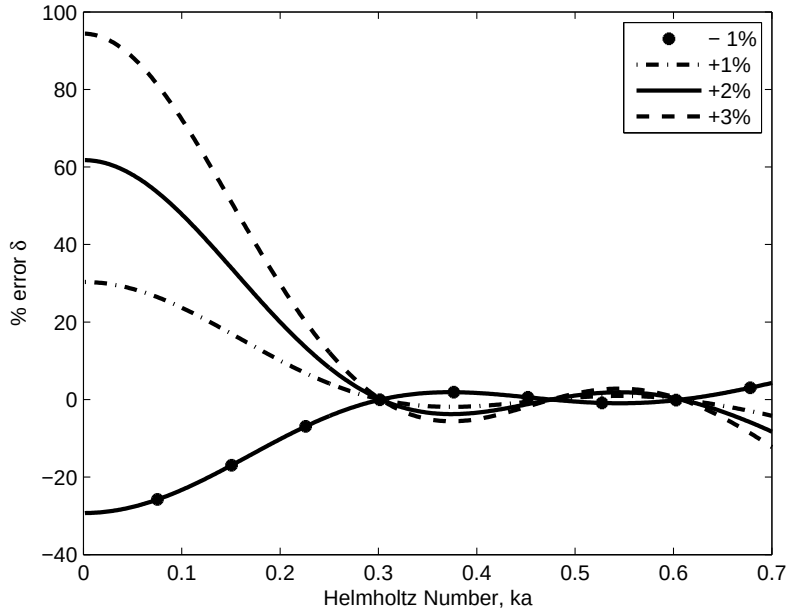

FIGURE A.8: Estimated error in measurement of $\frac{\delta}{a}$ for a given percentage error in transfer function.

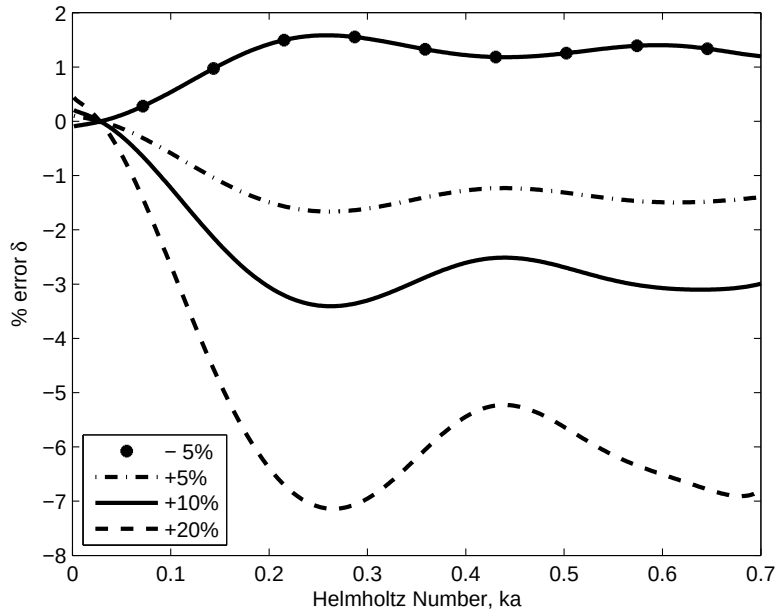

FIGURE A.9: Estimated error in measurement of $\frac{\delta}{a}$ for a given percentage error in Mach number.

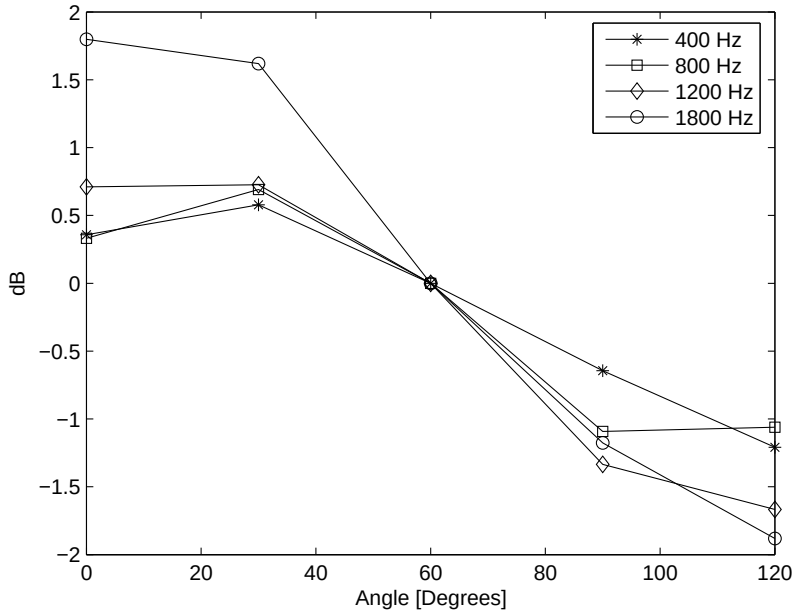

FIGURE A.10: Directivity of sound radiated from duct termination with an internal radius of 20mm. The results are normalised with the acoustic pressure at microphone at 60^o to the duct central axis.

A.3 Directivity of radiated field from duct termination

Figure A.10 is a plot of the directivity of the sound field radiated from a simple unflanged duct with an internal diameter of 40mm. The results are normalised with the measured acoustic pressure at 60^o to the pipe central axis. The measurements where taken in the anechoic chamber of the Doak lab with the duct termination positioned 2m from the nearest wedged surface. The farfield microphones were positioned 750mm from the central axis of the duct termination. It is apparent from the plot that the radiated field is not strictly monopole. However, further analysis of the results indicated that the measured acoustic pressure at 60^o to the duct centre line axis remains within 10% of the mean acoustic pressure of the radiated field over the frequency range. Consequently, in this thesis when monopole radiation is assumed to determine the radiated sound power the farfield microphone is position at 60^o to the duct central line axis.

A.4 Determination of pressure drop across orifice

Consider the flow through an orifice in a duct as described by figure 4.1. The pressure drop, $\Delta\bar{P}$, across the orifice can be determined by applying the continuity and Bernoulli equations for incompressible steady frictionless flow respectively:

$$Q = S_1 U_1 = S_2 U_2, \tag{A.1}$$

$$p = p_1 + \frac{1}{2}\rho U_1^2 = p_2 + \frac{1}{2}\rho U_2^2. \tag{A.2}$$

Using eqnsA.1 & A.2 to eliminate U_2, provides

$$\frac{Q}{S_1} = U_1 \approx \left[\frac{2(p_2 - p_1)}{\rho(1 - (S_1/S_2)^2)}\right]^{\frac{1}{2}}. \tag{A.3}$$

However, this expression ignores the effect of viscosity as well as the vena contracta effect downstream of the contraction. To account for this a dimensionless discharge coefficient, C_d, is adopted providing

$$Q = S_o U_o = C_d So = \left[\frac{2\Delta\bar{P}}{\rho(1 - (S_1/S_2)^2)}\right]^{\frac{1}{2}}, \tag{A.4}$$

where $\Delta\bar{P}$ is the pressure drop across the orifice. Rearranging this provides an expression for the pressure drop as

$$\Delta\bar{P} = \frac{\rho Q^2(1 - (S_1/S_2)^2)}{2C_d^2 S_o^2}. \tag{A.5}$$

The discharged coefficient is a function of Reynolds number, Re, with the ASME recommending the curve fit formulas developed by the ISO [92]. The basic form of the curve fit is

$$C_d = f(\beta) + 91.71\beta^{2.5}Re^{-0.75} + \frac{0.09\beta^4}{1 - \beta^4}F_1 - 0.00337\beta^3 F_2, \tag{A.6}$$

where $\beta = \sqrt{\frac{S_1}{S_o}}$ and $f(\beta) = 0.5959 + 0.0312\beta^{2.1} - 0.184\beta^8$. The correlation factors F_1 and F_2 vary with the position of the pressure tappings. For the configuration used in the experiment type 2 pressure tapings were employed with $F_1 = 0.433$ and $F_2 = 0.47$. For the orifice geometries and Reynolds number range of the

experiments an average discharge coefficient of approximately $C_d = 0.62$ was determined.

A.5 Determination the friction velocity

The friction velocity, u_* can be defined as [71]

$$u_* = \sqrt{\frac{\tau_w}{\rho}} \tag{A.7}$$

where τ_w is the wall shear which can be defined as

$$\tau_w = \frac{F_d \rho \bar{U}^2}{8}. \tag{A.8}$$

F_d is the Darcy friction factor, a dimensionless number used in internal flow calculations. It expresses the linear relationship between flow velocity and pressure gradient and is defined as

$$F_d = \frac{\frac{dp}{dx} D}{1/2 \rho \bar{U}}, \tag{A.9}$$

where dp/dx is the pressure gradient in the pipe and D is the pipe hydraulic diameter. If the pressure gradient is not known the friction factor can be estimated via Haaland's [93] expression

$$F_d \approx \frac{1}{-1.8 log_10 \left[\frac{6.9}{Re} + \left(\frac{\epsilon/D}{3.7} \right)^{1.11} \right]}. \tag{A.10}$$

The parameter ϵ is the pipe surface roughness. The pipe roughness depends on pipe material and manufacturing process. For the smooth extruded plastic pipe used in experiments for this thesis a surface roughness of 0.0015mm [71] was adopted. The friction velocity can then be determined using eqns A.7, A.8 & A.10.

A.6 Expansion chamber farfield microphone measurements

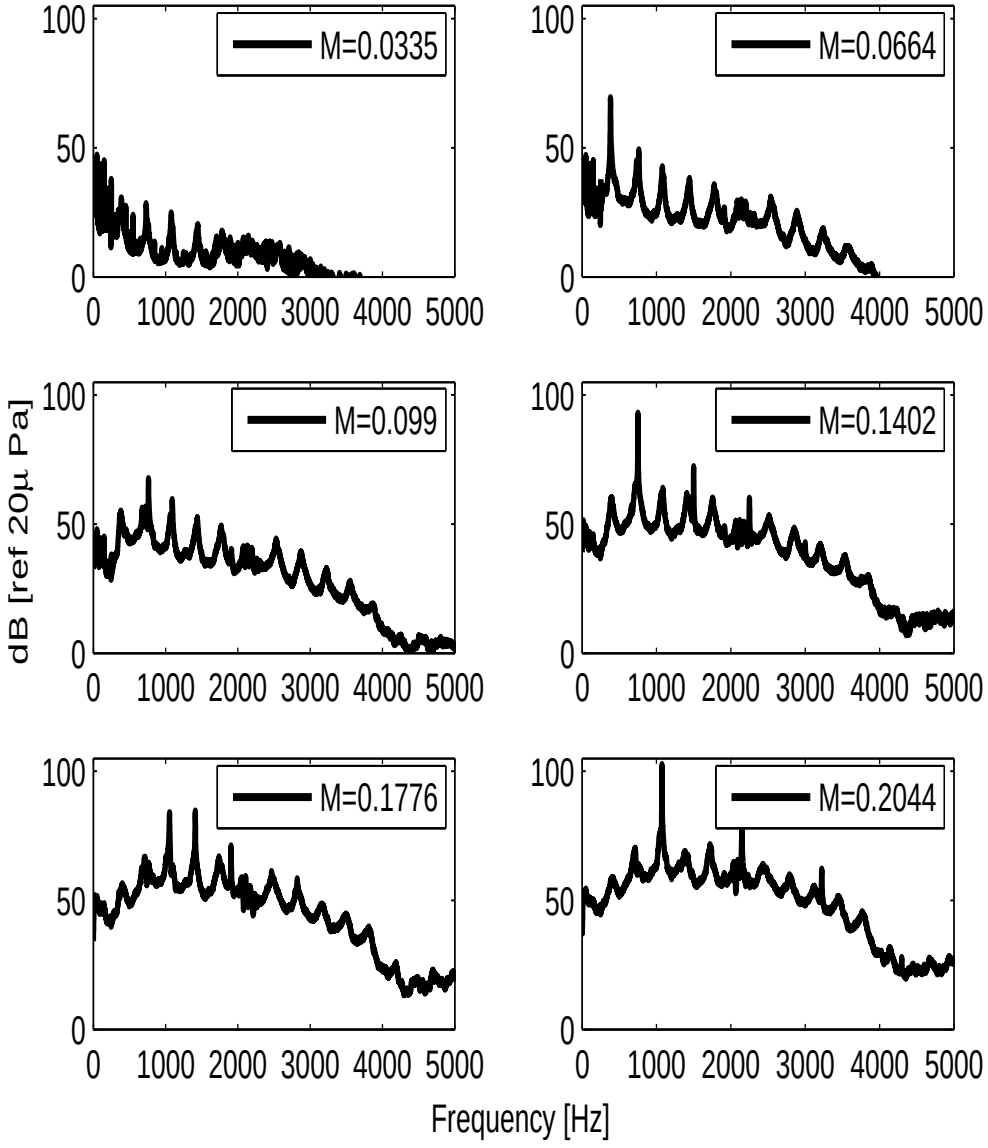

FIGURE A.11: Sound pressure level (dB ref 20μPa) measured at microphone #5 in farfield 500mm from flow excited expansion chamber tailpipe termination. Expansion chamber length 2D.

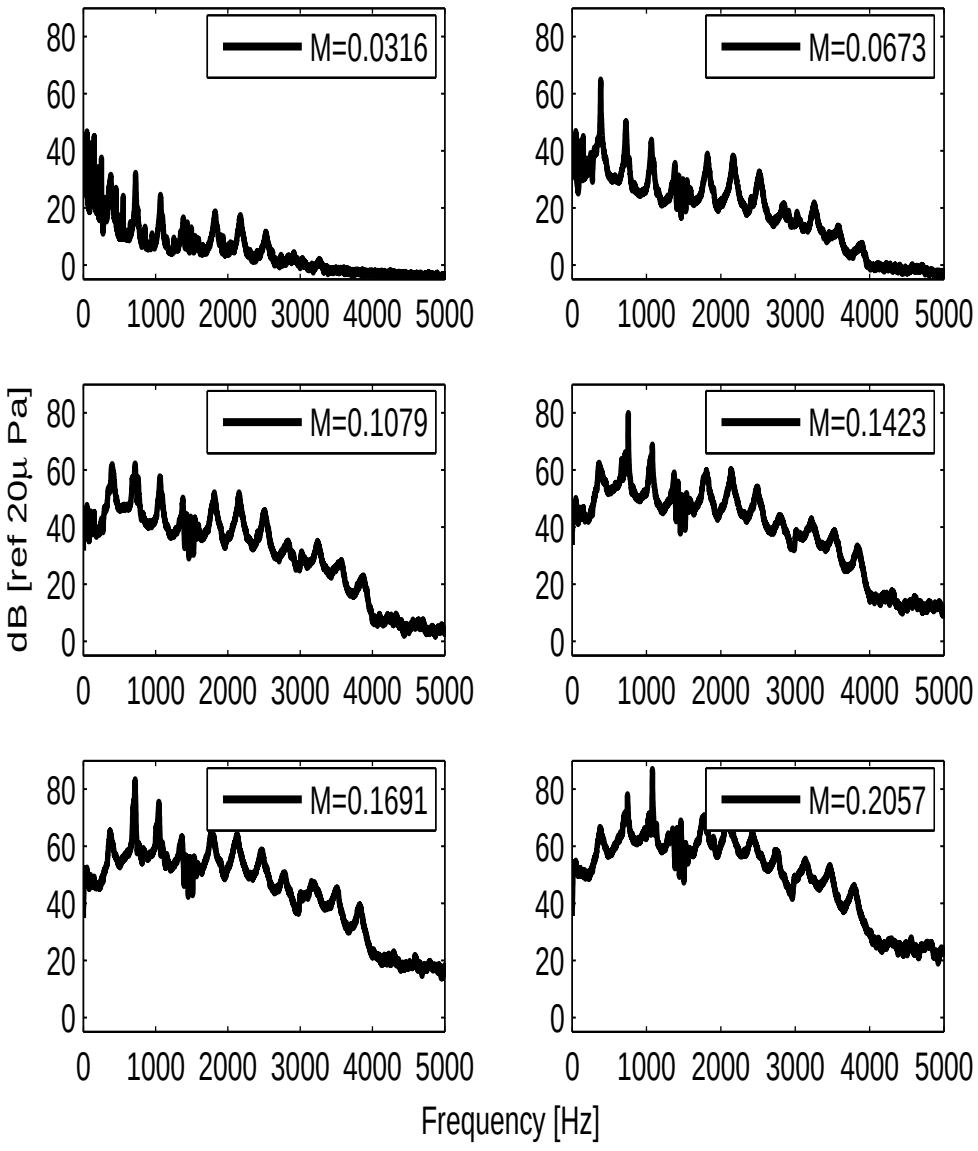

FIGURE A.12: Sound pressure level (dB ref 20μPa) measured at microphone #5 in farfield 500mm from flow excited expansion chamber tailpipe termination. Expansion chamber length 3D.

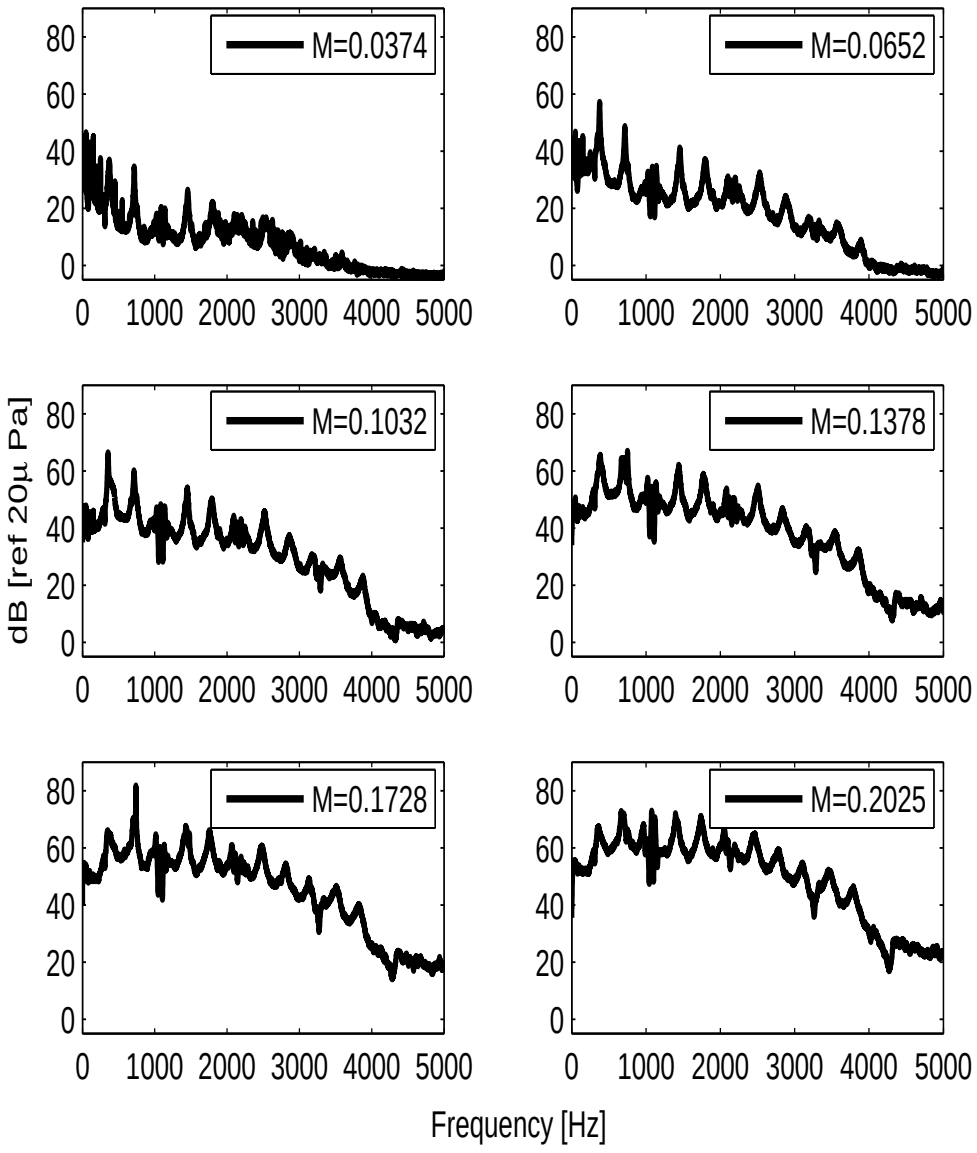

FIGURE A.13: Sound pressure level (dB ref 20μPa) measured at microphone #5 in farfield 500mm from flow excited expansion chamber tailpipe termination. Expansion chamber length 4D.

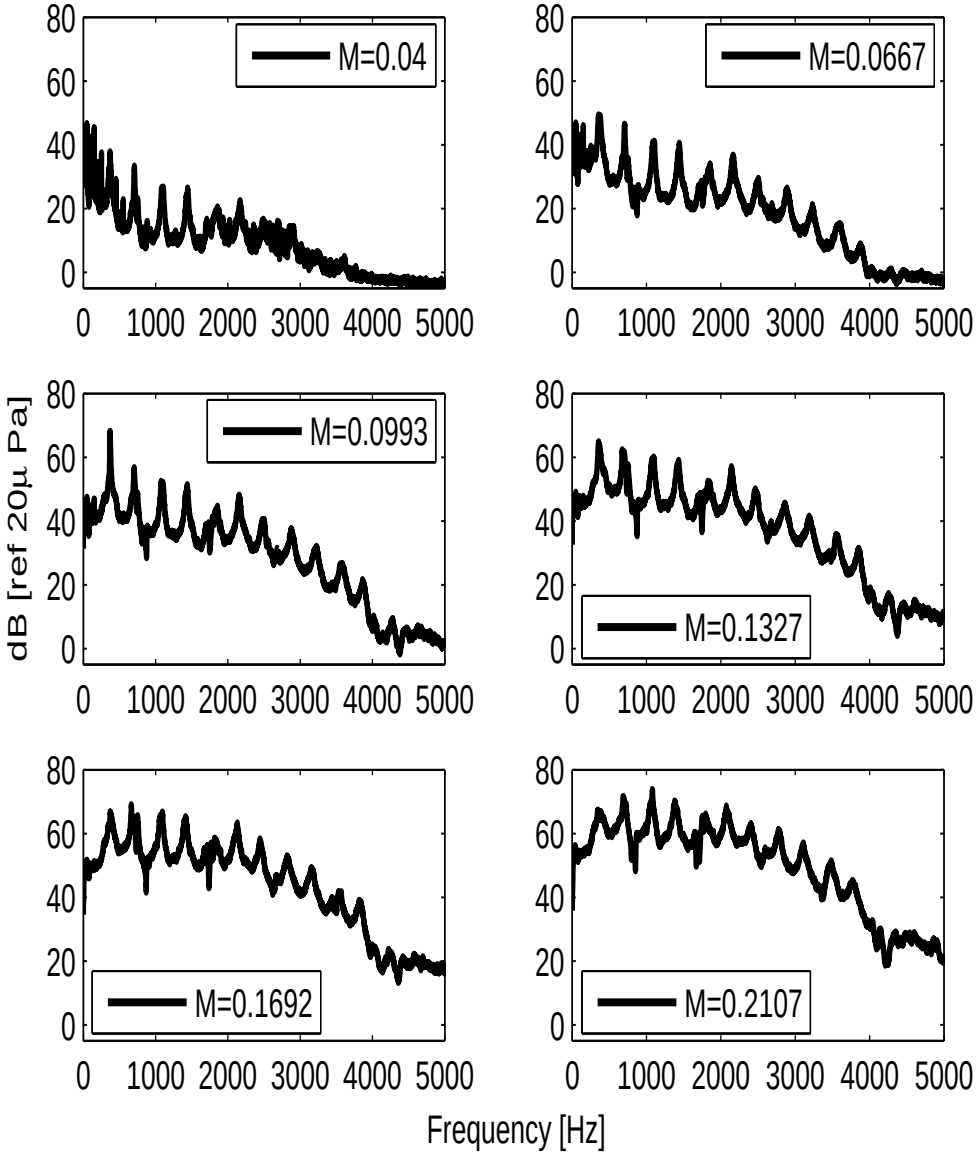

FIGURE A.14: Sound pressure level (dB ref 20μPa) measured at microphone #5 in farfield 500mm from flow excited expansion chamber tailpipe termination. Expansion chamber length 5D.

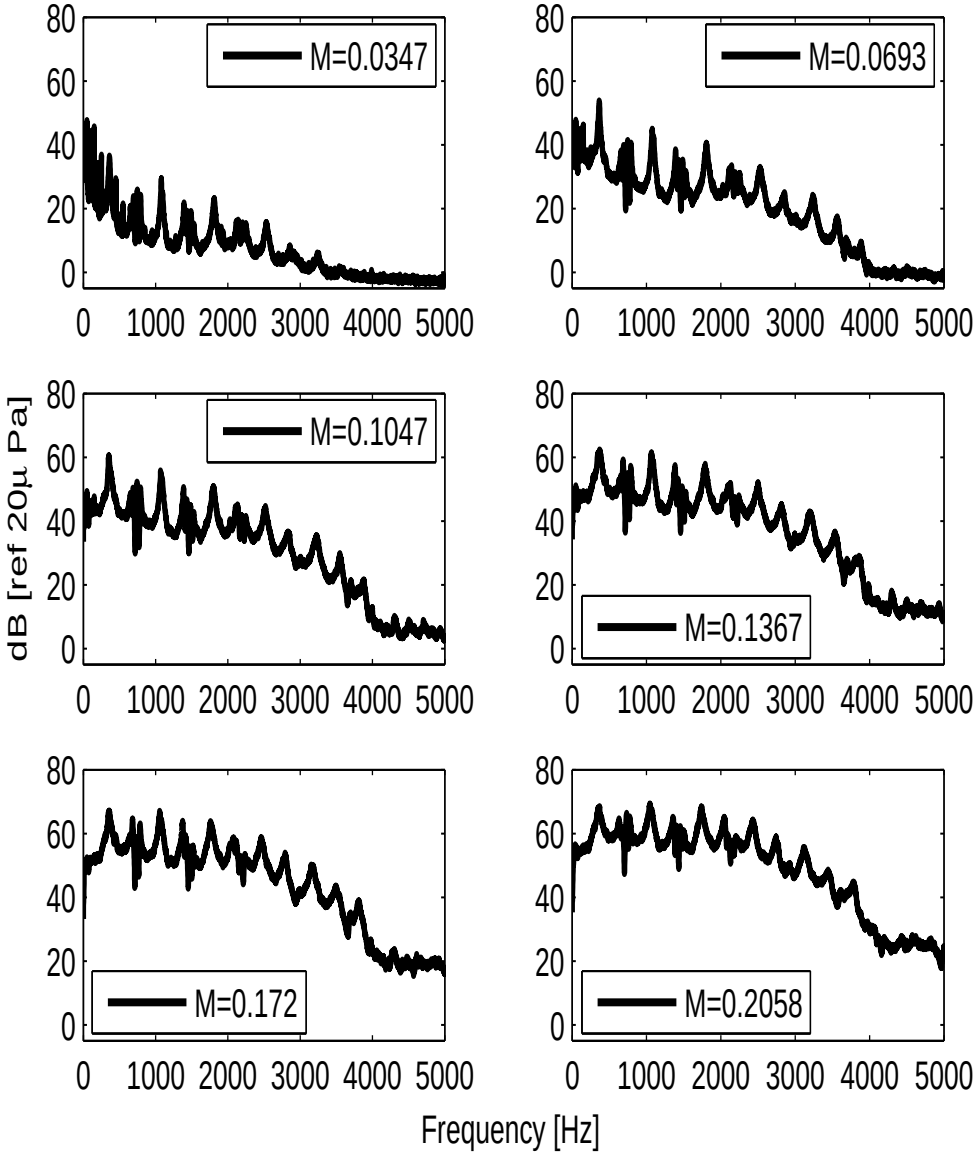

FIGURE A.15: Sound pressure level (dB ref 20μPa) measured at microphone #5 in farfield 500mm from flow excited expansion chamber tailpipe termination. Expansion chamber length 6D.

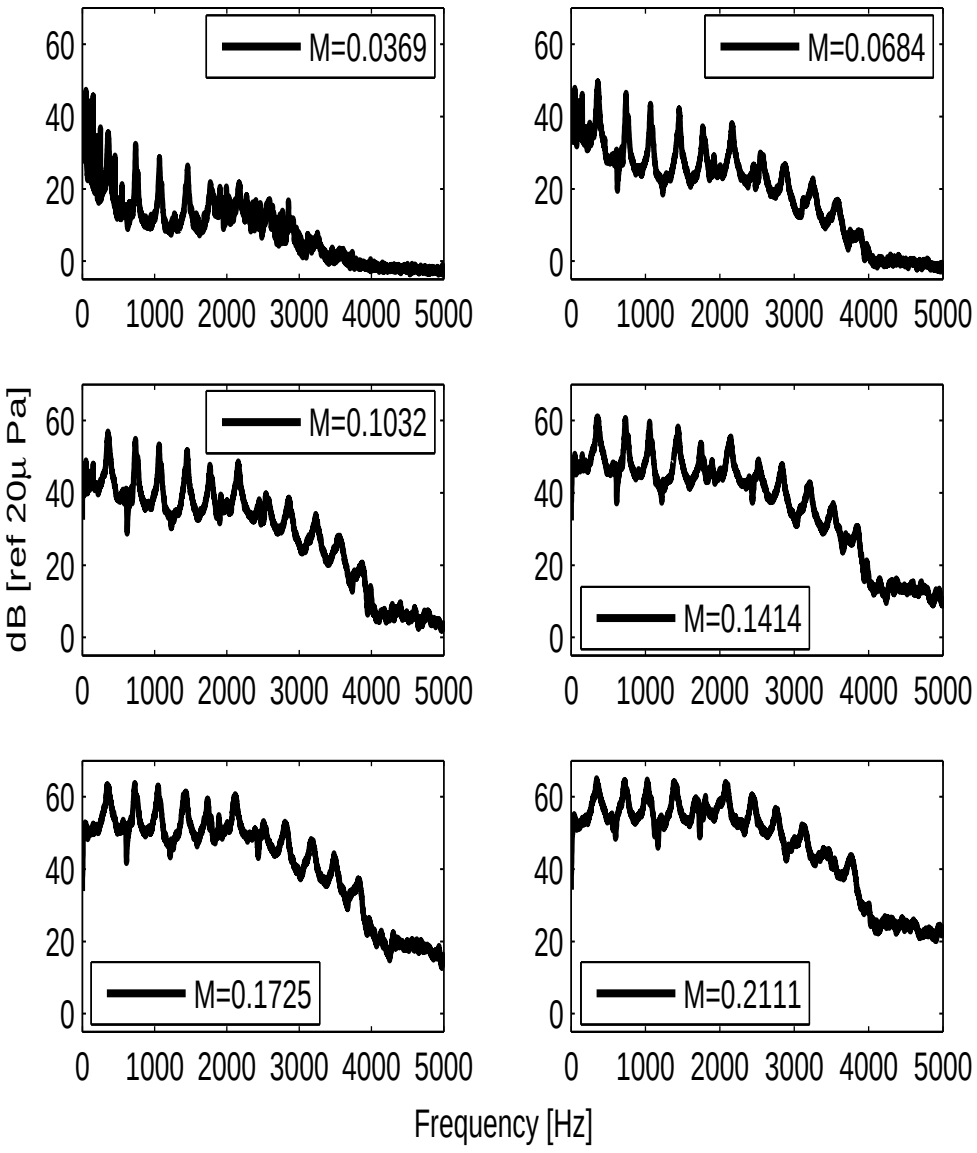

FIGURE A.16: Sound pressure level (dB ref 20μPa) measured at microphone #5 in farfield 500mm from flow excited expansion chamber tailpipe termination. Expansion chamber length 7D.

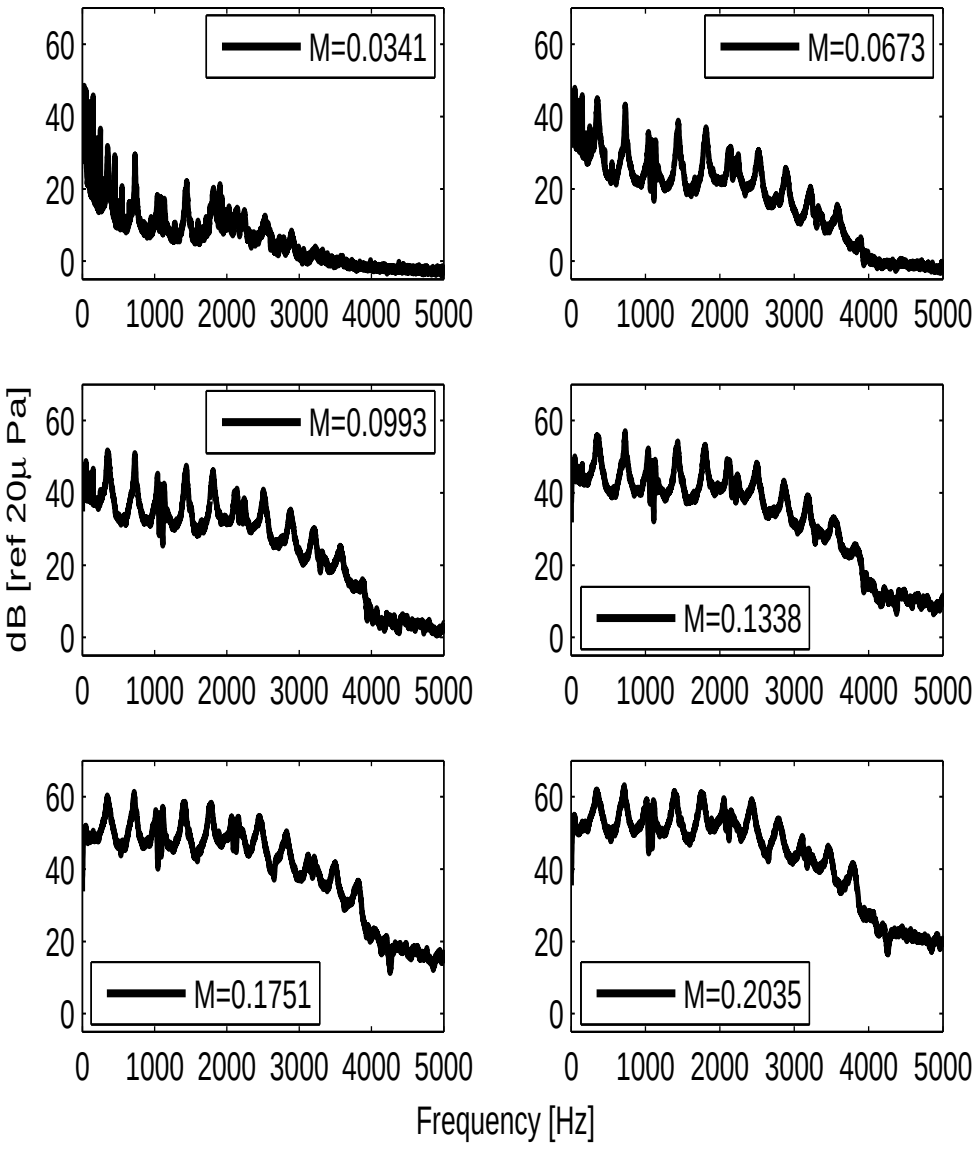

FIGURE A.17: Sound pressure level (dB ref 20μPa) measured at microphone #5 in farfield 500mm from flow excited expansion chamber tailpipe termination. Expansion chamber length 8D.

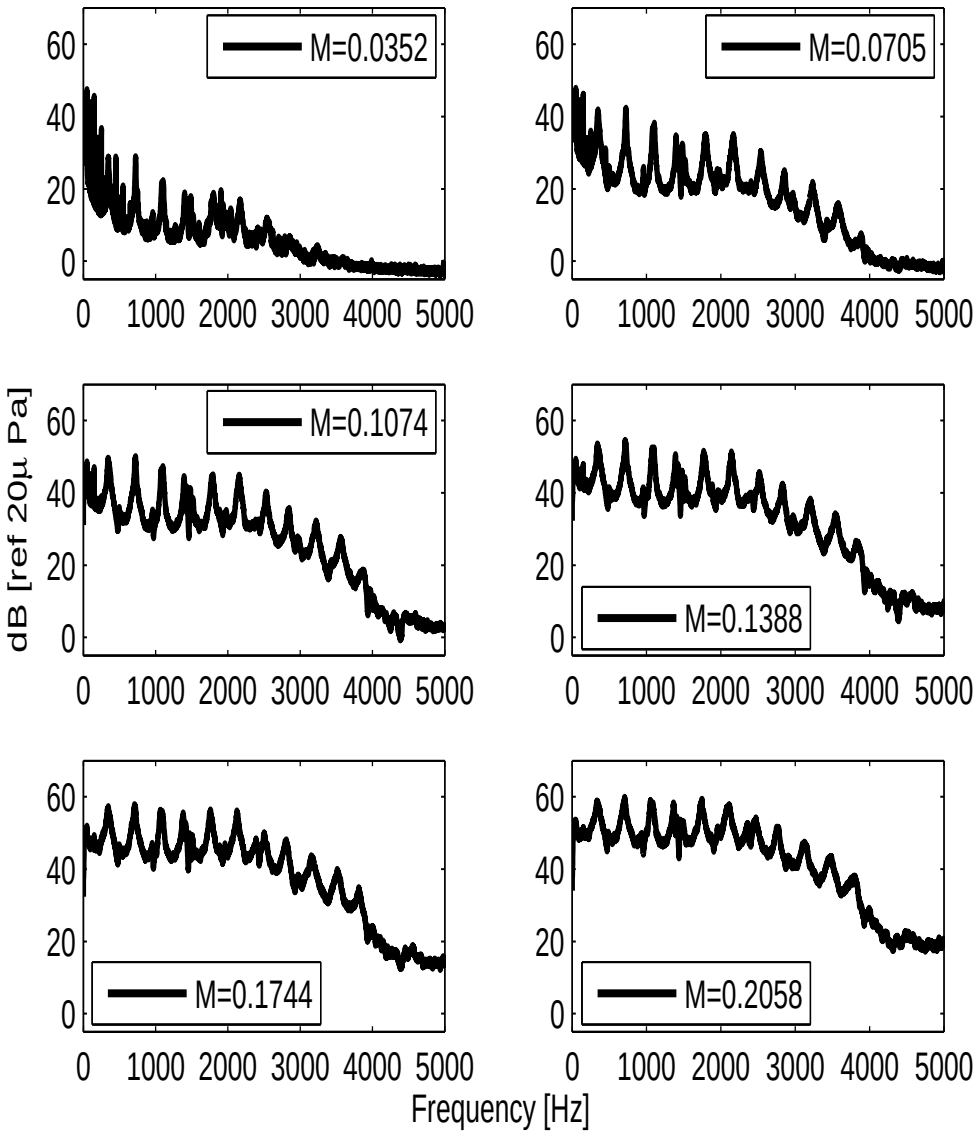

FIGURE A.18: Sound pressure level (dB ref 20μPa) measured at microphone #5 in farfield 500mm from flow excited expansion chamber tailpipe termination. Expansion chamber length 9D.

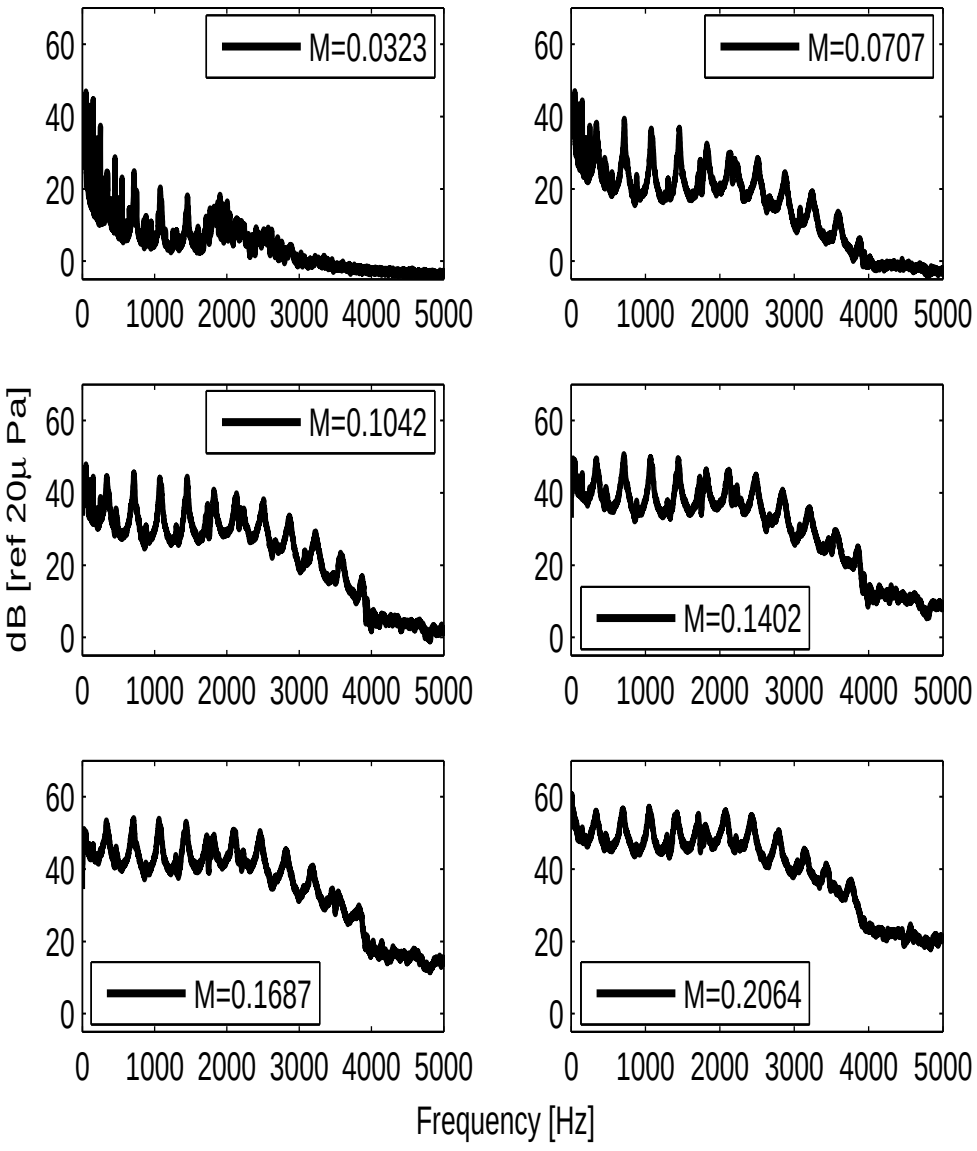

FIGURE A.19: Sound pressure level (dB ref 20μPa) measured at microphone #5 in farfield 500mm from flow excited expansion chamber tailpipe termination. Expansion chamber length 10D.

A.7 Chamber source velocity dependence

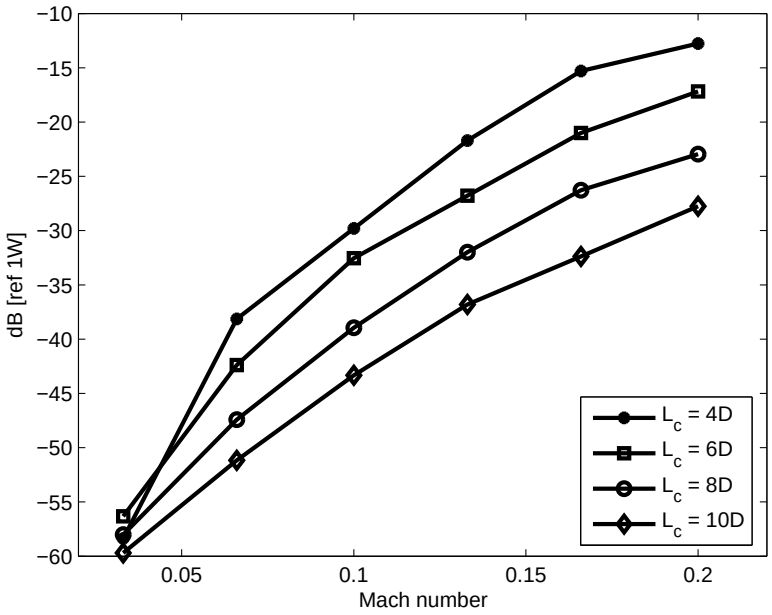

FIGURE A.20: Plot of total sound power radiated into the farfield from the tailpipe termination of a simple flow excited expansion chamber. Sound power plotted in dB [ref 1W] as a function of Mach number

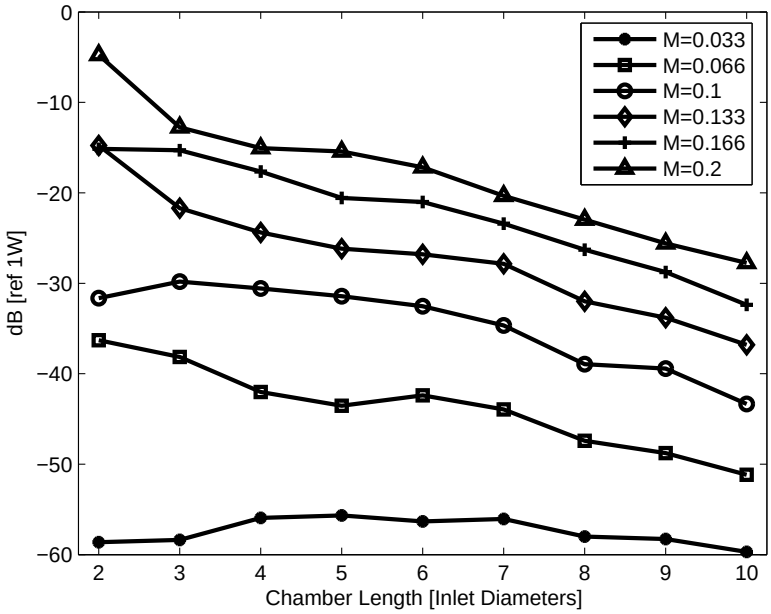

FIGURE A.21: Plot of total sound power radiated into the farfield from the tailpipe termination of a simple flow excited expansion chamber. Sound power plotted in dB [ref 1W] as a function of expansion chamber length in inlet diameters.

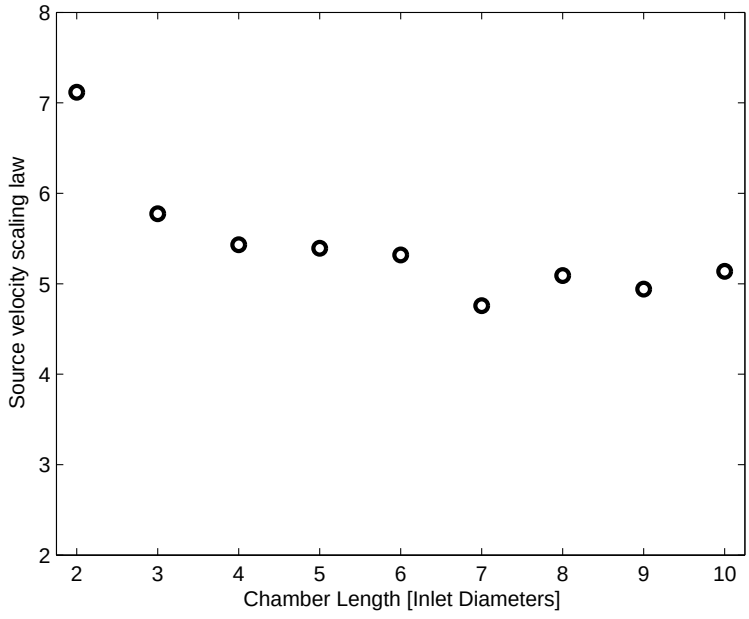

FIGURE A.22: Velocity dependence of aeroacoustic source associated with a simple flow excited expansion chamber. Velocity dependence plotted as a function of chamber length.

Bibliography

[1] Gwnal Gabard and Jeremy Astley. Theoretical model for sound radiation from annular jet pipes: Far- and near-field solutions. *Journal of Fluid Mechanics*, 549(315-41):1103–1124, 2006.

[2] Harold Levine and Julian Schwinger. On the radiation of sound from an unflanged circular. *Physical Review*, 73(4):383–406, 1948.

[3] R. M. Munt. The interaction of sound with a subsonic jet issuing from a semi-infinite cylindrical pipe. *Journal of Fluid Mechanics*, 83(4):609–640, 1977.

[4] R. M. Munt. Acoustic transmission properties of a jet pipe with subsonic jet flow: I. the cold jet reflection coefficient. *Journal of Sound and Vibration*, 142(3):413–436, 1990.

[5] S. W. Rienstra. On the acoustic implications of vortex shedding from an exhaust pipe. *Journal of Engineering for Industry*, 103:378–384, 1981.

[6] S. W. Rienstra. A small strouhal number analysis for acoustic wave-jet flow-pipe interaction. *Journal of Sound and Vibration*, 86(4):539–556, 1983.

[7] G. C. J. HOFMANS, R. J. J. BOOT, P. P. J. M. DURRIEU, Y. AUREGAN, and A. HIRSCHBERG. Aeroacoustic response of a slit-shaped diaphragm in a pipe at low helmholtz number, 1: Quasi-steady results. *Journal of Sound and Vibration*, 244(1):35–56, 2001.

[8] J.M. Desantes, A.J. Torregrosa, and A. Broatch. Experiments on flow noise generation in simple exhaust geometries. *Acta Acustica united with Acustica*, 87:46–55, 2001.

[9] P. O. A. L Davies. Practical flow duct acoustics. *Journal of Sound and Vibration*, 124(1):91–115, 1987.

[10] G Kirchhoff. Ueber den einfluss der warmeleleitung in eimen gase auf die schallbewegung. *Poggendorfer annalen*, 134:177–193, 1868.

[11] H. Tijdeman. On the propagation of sound waves in cylindrical tubes. *Journal of Sound and Vibration*, 39(1):1–33, 1975.

[12] P.O.A.L Davies. Plane acoustic wave propagation in hot gas flow. *Journal of Sound and Vibration*, 122(2):389–392, 1988.

[13] E. Dokumaci. Sound transmission in narrow pipes with superimposed uniform mean flow and acoustic modelling of automobile catalytic converters. *Journal of Sound and Vibration*, 182(5):799–808, 1995.

[14] E. Dokumaci. A note on transmission of sound in a wide pipe with mean flow and viscothermal attenuation. *Journal of Sound and Vibration*, 208(4): 653–655, 1997.

[15] H. V. Helmholtz. Verhandlungen der naturhistorisch - medizinischen vereins zu heidelberg, bd iii, 16. 1863.

[16] G. Kirchhoff. Ueber den einfluss der wrmeleitung in einem gase auf die schallbewegung. *Annalen der Physik und Chemie*, 210(6):177–193, 1868.

[17] Rayleigh. *Theory of Sound*, volume 2. 1896.

[18] Uno Ingard and Vijay K Singhal. Sound attenuation in turbulent pipe flow. *The Journal of the Acoustical Society of America*, 55(3):535–538, 1974.

[19] M. S. Howe. The damping of sound by wall turbulent shear layers. *The Journal of the Acoustical Society of America*, 98(3):1723–1730, 1995.

[20] M. C. A. M. Peters, Hirschberg A., and A.J. Wijnands A.P.J. Reihnen. Damping and reflection coefficient measurements for an open pipe at low mach and low helmholtx numbers. *Journal of Fluid Mechanics*, 256:499–534, 1993.

[21] Sabry Allam and Mats Abom. Investigation of damping and radiation using full plane wave decomposition in ducts. *Journal of Sound and Vibration*, 292 (3-5):519–534, 2006.

[22] P. O. A. L. Davies, J. L. Bento Coelho, and M. Bhattacharya. Reflection coefficients for an unflanged pipe with flow. *Journal of Sound and Vibration*, 72(4):543–546, 1980.

[23] R. J. Alfredson and P. O. A. L. Davies. Performance of exhaust silencer components. *Journal of Sound and Vibration*, 15(2):175–196, 1971.

[24] T.H. Schlinker. Transmission of acoustic-plane waves at a jet exhaust. *AIAA Journal*, 77(22), 1977.

[25] C. L. Morfey. *Dictionary of Acoustics*. Academic Press, 2001.

[26] J. P. DALMONT, C. J. NEDERVEEN, and N. JOLY. Radiation impedance of tubes with different flanges: Numerical and experimental investigations. *Journal of Sound and Vibration*, 244(3):505–534, 2001.

[27] A. N. Norris and I. C. Sheng. Acoustic radiation from a circular pipe with an infinite flange. *Journal of Sound and Vibration*, 135(1):85–93, 1989.

[28] R.J. Alfredson and P.O.A.L. Davies. The radiation of sound from an engine exhaust. *Journal of Sound and Vibration*, 13(4):389–408, 1970.

[29] L.L. Beraneck. *Acoustic Measurements*. J. Wiley & Sons, 1949.

[30] William S. Gatley and Raymond Cohen. Methods for evaluating the performance of small acoustic filters. *The Journal of the Acoustical Society of America*, 46(1A):6–16, 1969.

[31] D. C. VAN DER WALT. *Rapid Acoustic Assessment of Exhaust Systems During Engine Accelleration*. PhD thesis, University of Southampton, 2002.

[32] T.H. Melling. An impedance tube for precision measurement of acoustic impedance and insertion loss at high sound pressure levels. *Journal of Sound and Vibration*, 28(1):23–54, IN1, 1973.

[33] M. L. Kathuriya and M. L. Munjal. An accurate method for the experimental evaluation of the acoustical impedance of a black box. *The Journal of the Acoustical Society of America*, 58(2):451–454, 1975.

[34] M. L. Kathuriya and M. L. Munjal. A method for the experimental evaluation of the acoustic characteristics of an engine exhaust system in the presence of mean flow. *The Journal of the Acoustical Society of America*, 60(3):745–751, 1976.

[35] A. F. Seybert and D. F. Ross. Experimental determination of acoustic properties using a two-microphone random-excitation technique. *The Journal of the Acoustical Society of America*, 61(5):1362–1370, 1977.

[36] A. F. Seybert and Benjamin Soenarko. Error analysis of spectral estimates with application to the measurement of acoustic parameters using random sound fields in ducts. *The Journal of the Acoustical Society of America*, 69 (4):1190–1199, 1981.

[37] J. Y. Chung and D. A. Blaser. Transfer function method of measuring in-duct acoustic properties. ii. experiment. *The Journal of the Acoustical Society of America*, 68(3):914–921, 1980.

[38] J. Y. Chung and D. A. Blaser. Transfer function method of measuring in-duct acoustic properties. i. theory. *The Journal of the Acoustical Society of America*, 68(3):907–913, 1980.

[39] M. Bhattacharya. *Engine Noise Source Characterisation - an analysis and evaluation of experimental techniques.* PhD thesis, University of Southampton, 1980.

[40] J. L. Bento Coelho. *Aeroacoustic characteristics of perforate liners in expansion chambers.* PhD thesis, University of Southampton, 1983.

[41] K. R. Holland and P. O. A. L. Davies. The measurement of sound power flux in flow ducts. *Journal of Sound and Vibration*, 230(4):915–932, 2000.

[42] Keith R. Holland, Peter O. A. L. Davies, and Danie C. van der Walt. Sound power flux measurements in strongly exited ducts with flow. *The Journal of the Acoustical Society of America*, 112(6):2863–2871, 2002.

[43] J. S. Bendat and A.G. Piersol. *Random Data: Analysis and Measurement Procedures.* Wiley & Sons Inc, 605 Third Avenue, New York, 3rd edition edition, 2000.

[44] J. Y. Chung. Rejection of flow noise using a coherence function method. *The Journal of the Acoustical Society of America*, 62(2):388–395, 1977.

[45] D. Ronneberger and C. D. Ahrens. Wall shear stress caused by small amplitude perturbations of turbulent boundary-layer flow: an experimental investigation. *J. Fluid Mech*, 83(3):433–464, 1977.

[46] M.J. Lighthill. On sound generated aerodynamically i. *Proceedings of the Royal Society*, 211:564–587, 1952.

[47] M.J. Lighthill. On sound generated aerodynamically ii, 1954.

[48] N Curle. The influence of solid boundaries upon aerodynamic sound. *Proceedings of the Royal Society*, 231:505–575, 1955.

[49] M. S. Howe. On the absorption of sound by turbulence and other hydrodynamic flows. *IMA J Appl Math*, 32(1-3):187–209, 1984.

[50] N. H. Fletcher. Nonlinear interactions in organ flue pipes. *The Journal of the Acoustical Society of America*, 56(2):645–652, 1974.

[51] N. H. Fletcher. Airflow and sound generation in musical wind instruments. *Annual Review of Fluid Dynamics*, 11, 1979.

[52] S. Ziada, H. Ng, and C. E. Blake. Flow excited resonance of a confined shallow cavity in low mach number flow and its control. *Journal of Fluids and Structures*, 18(1):79–92, 2003.

[53] J. C. Bruggeman, A. Hirschberg, M. E. H. van Dongen, A. P. J. Wijnands, and J. Gorter. Self-sustained aero-acoustic pulsations in gas transport systems: Experimental study of the influence of closed side branches. *Journal of Sound and Vibration*, 150(3):371–393, 1991.

[54] P. O. A. L Davies and K. R. Holland. The observed aeroacoustic behaviour of some flow excited expansion chambers. *Journal of Sound and Vibration*, 239(4):695–708, 2001.

[55] J.C. Hardin and Pope D.S. Sound generation by a stenosis in a pipe. *AIAA Journal*, 30(2):312–317, 1992.

[56] P. A. Nelson, N. A. Halliwell, and P. E. Doak. Fluid dynamics of a flow excited resonance, part i: Experiment. *Journal of Sound and Vibration*, 78 (1):15–38, 1983.

[57] P. A. Nelson and C. L. Morfey. Aerodynamic sound production in low speed flow ducts. *Journal of Sound and Vibration*, 79(2):263–289, 1981.

[58] Colin G. Gordon. Spoiler-generated flow noise. i. the experiment. *The Journal of the Acoustical Society of America*, 43(5):1041–1048, 1968.

[59] Colin G. Gordon. Spoiler-generated flow noise. ii. results. *The Journal of the Acoustical Society of America*, 45(1):214–223, 1969.

[60] P. O. A. L Davies and K. R. Holland. Flow noise generation in expansion chambers. In *Institute of Acoustics Spring Conference*, volume 26, University of Southampton., 2004.

[61] A.J. Torregrosa, A. Broatch, V. Bermudez, and I. Andres. Experimental assessment of emission models used for ic engine exhaust noise prediction. *Experimental Thermal and Fluid Science*, 30(2):97–107, 2005.

[62] S. Ziada and S. Shine. Strouhal numbers of flow-excited acoustic resonance of closed side branches. *Journal of Fluids and Structures*, 13:127–142, 1999.

[63] D. Rockwell, J. C. Lin, P. Oshkai, M. Reiss, and M. Pollack. Shallow cavity flow tone experiments: onset of locked-on states. *Journal of Fluids and Structures*, 17(3):381–414, 2003.

[64] Y. Yang, D. Rockwell, K. Lai-Fook Cody, and M. Pollack. Generation of tones due to flow past a deep cavity: Effect of streamwise length. *Journal of Fluids and Structures*, 25(2):364–388, 2009.

[65] SAMIR ZIADA. Interaction of a jet-slot oscillator with a deep cavity resonator and its control. *Journal of Fluids and Structures*, 15(6):831–843, 2001.

[66] B. Karthik, S. R. Chakravarthy, and R. I. Sujith. The effect of orifice thickness on the vortex-acoustic interaction in a duct, 2001.

[67] T. Douglas Mast and Allan D. Pierce. Describing-function theory for flow excitation of resonators. *The Journal of the Acoustical Society of America*, 97(1):163–172, 1995.

[68] G. Heinzel, A. Rudiger, and R. Schilling. *Spectrum and spectral density estimation by the Discrete Fourier transform (DFT), including a comprehensive list of window functions and some new at-top windows.* ESA, 2002.

[69] J. Y. Chung and D. A. Blaser. Transfer function method of measuring acoustic intensity in a duct system with flow. *The Journal of the Acoustical Society of America*, 68(6):1570–1577, 1980.

[70] M. F. Harrison. *Time and frequency domain modelling of vehicle intake and exhaust systems.* PhD thesis, University of Southampton, 1994.

[71] F White. *Fluid Mechanics*. McGraw-Hill, 4th edition edition, 1999.

[72] J. P. DALMONT. Acoustic impedance measurement, part ii: A new calibration method. *Journal of Sound and Vibration*, 243(3):441–459, 2001.

[73] E. Dokumaci. On calculation of acoustic power. *Journal of Sound and Vibration*, 238(5):869–876, 2000.

[74] David H. Munro and K. Uno Ingard. On acoustic intensity measurements in the presence of mean flow. *The Journal of the Acoustical Society of America*, 65(6):1402–1406, 1979.

[75] J. K. Thompson and D. R. Tree. Finite difference approximation errors in acoustic intensity measurements. *Journal of Sound and Vibration*, 75(2):229–238, 1981.

[76] A. M. Cargill. Low-frequency sound radiation and generation due to the interaction of unsteady flow with a jet pipe. *J. Fluid Mech(1982)*, 121:59–105, 1982.

[77] D. W. Bechert. Sound absorption caused by vorticity shedding, demonstrated with a jet flow. *Journal of Sound and Vibration*, 70(3):389–405, 1980.

[78] P. O. A. L. Davies and K. R. Holland. I.c. engine intake and exhaust noise assessment. *Journal of Sound and Vibration*, 223(3):425–444, 1999.

[79] N. K. Agarwal. The sound field in fully developed turbulent pipe flow due to internal flow separation, part i: Wall-pressure fluctuations. *Journal of Sound and Vibration*, 169(1):89–109, 1994.

[80] G.C.J. Hofmans. *Vortex sound in confined flows*. PhD thesis, Technische Universiteit Eindhoven, 1998.

[81] P. Mungur and G. M. L. Gladwell. Acoustic wave propagation in a sheared fluid contained in a duct. *Journal of Sound and Vibration*, 9(1):28–48, 1969.

[82] Hanno H. Heller and Sheila E. Widnall. Sound radiation from rigid flow spoilers correlated with fluctuating forces. *The Journal of the Acoustical Society of America*, 47(3B):924–936, 1970.

[83] P. O. A. L. Davies. Flow-acoustic coupling in ducts. *Journal of Sound and Vibration*, 77(2), 1981.

[84] G. Rubio, W. De Roaeck, J. Meyers, M. Baelmans, , and W. Desmet. Aeroacoustic noise source mechanisms in simple expansion chambers. In *27th AIAA Aeroacoustic Conference*, Cambridge, Massachusetts, 2006.

[85] P. Oshkai, D. Rockwell, and M. Pollack. Shallow cavity flow tones: transformation from large- to small-scale modes. *Journal of Sound and Vibration*, 280(3-5):777–813, 2005.

[86] J. E. Rossiter. The effectof cavities on the buffeting of aircraft. Technical report, Royal Aircraft Establishment (UK), 1962.

[87] M. L. Pollack. Flow-induced tones in side-branch pipe resonators. *The Journal of the Acoustical Society of America*, 67(4):1153–1156, 1980.

[88] P. A. Nelson, N. A. Halliwell, and P. E. Doak. Fluid dynamics of a flow excited resonance, part ii: Flow acoustic interaction. *Journal of Sound and Vibration*, 91(3):375–402, 1983.

[89] Slotine J. E and Li Weiping. Applied nonlinear control. Prentice-Hall, 1991.

[90] L. Huang. A theory of reactive control of low-frequency duct noise. *Journal of Sound and Vibration*, 238(4):575–594, 2000.

[91] K. Renji, P. S. Nair, and S. Narayanan. On acoustic radiation resistance of plates. *Journal of Sound and Vibration*, 212(4):583–598, 1998.

[92] ASME Fluid Meters Research Committee. The iso-asme orifice coefficient equation, 1981.

[93] S. E. Haaland. Simple and explicit formula for the friction factor in trubulent pipe flow. *J. Fluids Eng*, pages 89–90, 1983.